MS53035 GRADUATION PROJECT MSE

Effect of Copper on the Corrosion of High-Carbon Bearing Steels

Haowei Jiang (5718554)

Maria Santofimia Navarro; Yaiza Gonzalez Garcia; Hanzheng Huang

Abstract

Roller bearings are one of the most important industrial components with a large variety of challenging environmental applications. Under water-contaminated lubricant conditions, a protective layer of oxide forms on the surface of the most used 100Cr6 bearing steel, which helps suppress the corrosion rate, while adding corrosion-resistant alloying elements can improve this corrosion resistance further. Recent research suggests that the Cu alloying element in high-carbon steels contains numerous carbide precipitates, which can help to form a stronger passive layer and, thus, more effective in protecting the steel against corrosion. Meanwhile, the accumulation of Cu as a tramp element can degrade the quality and performance of scrap-based steel. This limits the proportion of scrap that can be used in new products and may require adding ore-based steel to dilute the copper content and maintain the required properties. This study investigates the effect of incorporating copper in high-carbon bearing steel manufactured from scrap on enhancing long-term atmospheric corrosion resistance. The effective usage of this tramp element will contribute to boosting the circular economy of steel.

In this project, high-carbon bearing steel containing a high amount of Cu (0.5 wt %) was hardened using martensitic or bainitic hardening and compared with the baseline hardened steel with no excessive Cu. The microstructures of the steel were characterized by LOM, SEM (EDS), XRD and XPS to study the retention/segregation of Cu. Electrochemical corrosion tests were used to validate the prediction. Finally, LOM, SEM (EDS), XRD and XPS were utilised to characterise the corroded surfaces.

Contents

List of Figures

List of Tables

1 Introduction

It is a global consensus that recycling materials to the maximum extent is vital in today's world, considering the climate change due to greenhouse gases and the rapid depletion of natural resources. This rule also applies to the steel industry. The Dutch government has set a target to achieve a complete circular economy by 2050 (Government of Netherlands, n.d.). A circular economy is a production and consumption model involving sharing, leasing, reusing, repairing, refurbishing and recycling existing materials and products for as long as possible. In this way, the life cycle of products is extended, waste is minimised, and minimum new raw materials are added (European Parliament, 2023). The emphasis on the circular economy model has reshaped the production of steel from using raw materials to using steel scraps and waste (Eurofer, 2015).

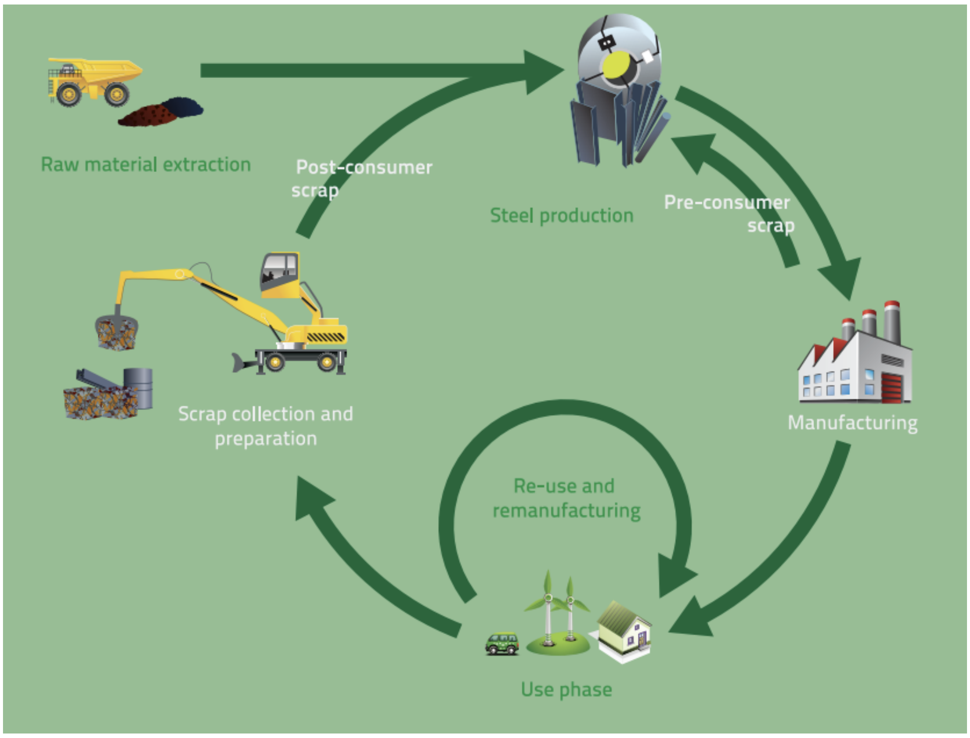

Figure 1: The steel cycle for reusing and recycling steel (Eurofer, 2015).

As shown in the steel cycle in Figure 1, steel is kept in a constant loop under the new production model by continuously reusing, remanufacturing and recycling. As of now, steel production accounts for approximately 6 % of all global CO_2 emissions, about 30 % of worldwide industrial carbon footprints, and around 73 % of global steel production comes from the primary steelmaking route using iron ores (Columbia Business School, 2024). Making future steel products from scrap would significantly contribute to environmental sustainability and circular economy.

1.1 Scrap Elements

Steel, with about 60% of all scrapped steel reused in new products and approximately 33% recycled scrap content in new products, is by far the world's most recycled material (The World Counts, 2018). However, using steel scrap is generally regarded as a downcycling process, in which steels are converted into long-term products of lower quality and value relative to their original features (Nidheesh & Kumar, 2019). The main reasons for that are the impurities introduced through mixed scrap and the gradual accumulation of certain hard-to-remove contaminant elements. This is detrimental in manufacturing high-performance steel, which has a low tolerance for chemical contamination and charge-to-charge chemical variation (Raabe et al., 2024). Using steel scrap for high-performance steel requires well-sorted scrap to control impurity elements, which affect undesirably in steel melting, casting, and downstream production processes, as well as the microstructure and properties of the final products.

Bearing steel, widely used in making rolling bearings for critical applications such as aerospace, has stringent requirements for strength, hardness, toughness, fatigue, and corrosion, low-tolerance specifications for alloying elements, namely Cr, Mn, Mo, and Ni, as well as low acceptance level for critical impurities, such as Cu and Sn (Bhadeshia, 2012). There are two distinct categories of such steel: case-hardened (CH) bearing steel with a carbon content of about 0.10–0.30 % and through-hardening (TH) bearing steel (also known as high-carbon bearing steel) with a carbon content of around 0.9–1.1 %, such as the 100Cr6 bearing steel (Cao et al., 2020). The focus will be on the latter, martensitic or bainitic through-hardened bearing steels, which accounts for a market size of around 45 % of the total global market size of 130.22 billion USD for bearing steel in 2022 (*Global High Carbon Bearing Steel Market Research Report 2022-2032*, 2024).

The main problem in high-carbon bearing steel is the accumulation of copper from steel scrap (Daehn, Serrenho, & Allwood, 2019). Copper, a tramp element from steel scrap, can be used in weathering steels as an alloying element, but in bearing steel, it is regarded as a non-removable impurity. This is because copper, unlike other scrap elements, is more noble than iron, so it cannot be oxidized into slag. It also does not form sulfides or phosphides stable enough to form a slag. Hence, no method for Cu removal is currently industrially viable, resulting in the copper remaining in the steel. The presence of the residual element is detrimental to the mechanical properties of the high-carbon bearing steel, with studies showing that impact toughness, hardness and ultimate tensile strength all decrease with increasing copper content (Cavaliere, 2023; Sekunowo et al., 2014).

Hence, when producing new high-quality steel from recycled material, the current practice is to use well-sorted scrap with low copper contamination or to dilute the charge with virgin material based on iron ore that is very low in Cu. However, this dilution method failed to reduce the reliance on the virgin steel produced from iron ore and is also not in line with the Dutch Government's goal of a completely circular economy by 2050 (Government of Netherlands, n.d.). Therefore, this study aims to increase copper tolerance in bearing steel by exploring the possibility of using copper as an alloying element.

1.2 Copper as an Alloying Element

Studies have shown that the addition of a small amount of copper is beneficial for the corrosion resistance of the steel. This has been proven extensively using low-carbon steel or low-alloy steel since very early times (Hao et al., 2017; J. Hong, Lee, Kim, & Yoon, 2012; Samusawa & Nakayama, 2019; Williams & Komp, 1965). Nevertheless, the effectiveness of copper in improving the corrosion resistance of high-carbon bearing steel has yet to be discovered. If proven effective, this could provide an alternative solution to deal with the accumulated residual elements in bearing steels. Instead of diluting and tolerating, one can make effective use of the scrap elements by enhancing their positive effects on specific properties while mitigating the negative impacts on other properties. In this manner, residual elements are turned into alloying elements without additional raw material or cost.

However, some scholars have pointed out the fact that copper increases the pitting corrosion of steel, no matter the weight percentage of carbon (I. Hong & Koo, 2005; Jang et al., 2009; Ujiro et al., 2001). The outcome is that copper produces two opposite effects on corrosion, enhancing pitting corrosion while suppressing uniform corrosion. The overall effectiveness will, therefore, be volatile due to changes in setup and working conditions. In addition, Díaz et al. (2018) states that incorporating more copper into steels with existing copper content does not create an additional effect on corrosion resistance. Therefore, a comprehensive understanding of copper's corrosion mechanism is exceptionally vital.

1.3 Research Methodology

Thus far, there is no concrete proof of the effectiveness of copper against corrosion in high-carbon bearing steel. Hence, the project's core goal is to find evidence of copper increasing corrosion resistance in bearing steel and, therefore, secure a more advanced material with better corrosion properties against challenging circumstances by turning copper from a tramp element into an alloying element in high-carbon bearing steel. In addition, the project must be aligned with the circular economy goal of the Dutch government (Government of Netherlands, n.d.) and the green development ideology adopted by the majority of the society.

The research will begin with a literature review to investigate the current state of development of copper addition in steels to gain knowledge on the working mechanism of copper, factors that alter corrosion resistance, and possible research gaps. From there, the experimental set-up and research questions were formulated for the study. Then, a corrosion test using the electrochemical polarisation method was done to analyse the effect of copper on different phases of the bearing steel. Its surface before and after corrosion was characterised by Light Optical Microscopy (LOM), Scanning Electron Microscopy (SEM), Energy Dispersive X-ray Spectroscopy (EDS), X-ray Diffraction (XRD) and X-ray Photoelectron Spectroscopy (XPS). From the results of the experiments, the effect of copper on the corrosion of high-carbon bearing steel was determined.

2 Literature Review

One central aspect of this literature review is to understand how copper affects steel's corrosion mechanism. Therefore, this section presents the main findings about the effectiveness and consequences of copper against corrosion in all kinds of steel. Additional information on the impact of copper on other properties, experimental conditions for a suitable corrosion test, and possible heat treatment for hardening the steel are also provided.

2.1 Advantages of Copper on Corrosion of Steel

It is almost certain that a mild amount of copper is beneficial against corrosion in steel (Hao et al., 2017; J. Hong et al., 2012; Samusawa & Nakayama, 2019; Williams & Komp, 1965). However, depending on the type of steel, the heat treatment, the working environment, etc., the effectiveness of copper addition and the corrosion mechanism may vary. The following will be an in-depth discussion of the advantages of copper on steel.

2.1.1 Copper vs Iron

The discussion on the effectiveness of copper begins with the most fundamental element in steel, iron. By comparing the corrosion density of pure iron, pure copper and 20 wt% Cu iron, which is given in Table 1, it is clear that copper is less corrosive than iron, and by adding copper to pure iron, a significant improvement can be seen in the corrosion resistance of iron (El-Egamy, 2008).

Table 1: Corrosion potential and corrosion density of different elements in 1.0 M NaCl solution of pH 2 after 60 min immersion (El-Egamy, 2008).

Sample	-Ecorr (V)	icorr (µA/cm2)
Pure Iron	0.578	120.2
Pure Copper	0.247	43.6
20wt% Cu Iron	0.572	71.5

However, steel's microstructural complexity is far above that of pure iron. Depending on the type of steel, its phases, etc., copper's efficiency against corrosion may vary.

2.1.2 Mechanism 1: Formation of Cu-riched Passive Layer

Experiments on copper addition in steels can be dated back to as early as 1965 when then material scientists proved that the corrosion of steel with 0.02 % Cu is 16 times faster than steel with 0.1 % Cu (Williams & Komp, 1965). This result remains valid over the years, with researchers drilling deeper into the hidden mechanism for the observation. More recent experiments have uncovered that the elemental Cu-enriched layer that was formed on the corroded surface of the steel is key to restricting further corrosion. This is proven by Figure 2, the results from Auger electron spectroscopy (AES) depth profiling of Cu and Fe atomic concentration for 0.2 wt% Cu steel after immersion in pH 1 NaCl solution for 1, 24 and 144 hours (Samusawa & Nakayama, 2019), with the increase in ratio of copper at depth = 0 nm over time. This inert layer will cut off all redox reactions happening on the surface, hence improving the corrosion resistance of the steel.

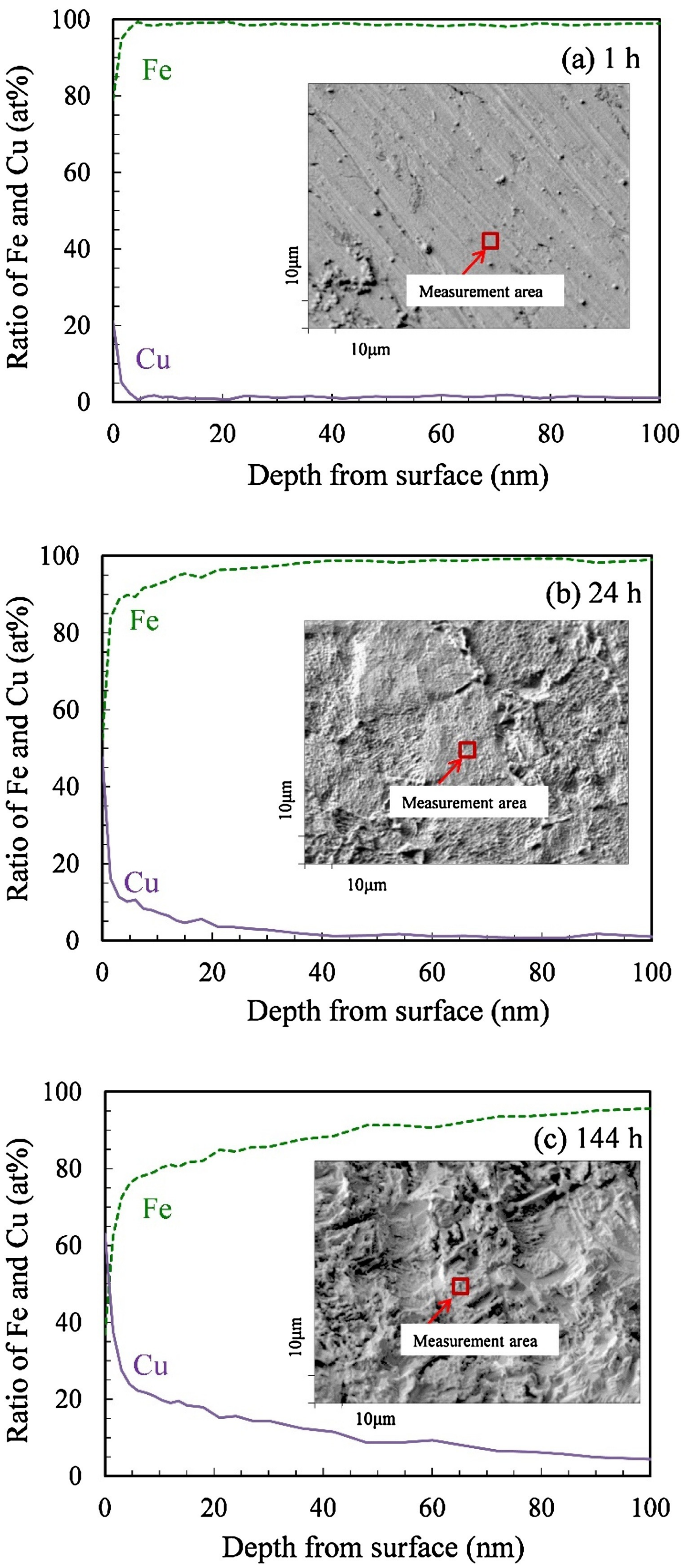

Figure 2: AES depth profiling of Cu and Fe atomic concentration for 0.2 wt% Cu low-carbon steel after immersion in pH 1 NaCl solution for 1, 24 and 144 hours (Samusawa & Nakayama, 2019).

The results from the polarisation curves given in Figure 3 also show that the anodic and cathodic reactions of the 0.2 wt% Cu low-carbon steel are being suppressed (Samusawa & Nakayama, 2019). This is because the Cu-enriched layer formed on the surface of the steel is a less corrosive layer that obstructs the steel's chemical structure from interacting with environmental compounds such as oxygen, bacteria or water, which can result in corrosion. Hence, adding a mild amount of copper is effective against the oxidation of steel.

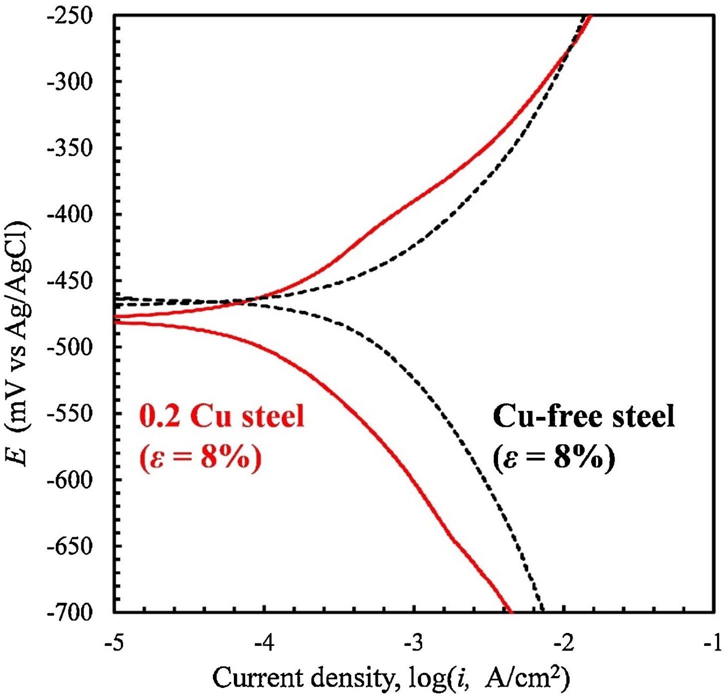

Figure 3: Polarisation curves for 0.2 wt% Cu steel and Cu-free steel in pH 1 NaCl solution (Samusawa & Nakayama, 2019).

By taking a closer look into the corrosion mechanism of steels, it is noted that when a steel specimen with Cu is exposed to a corrosive environment, the more active metals (Fe) are preferentially dissolved prior to Cu, resulting in copper particles accumulating on the surface. The result will be a surface layer rich in Cu. These copper particles accumulated on the surface will corrode and form either Cu_2O or $Cu(OH)_2$ as shown in Figure 4 (Jang et al., 2009), with Cu_2O and $Cu(OH)_2$ only observed in steels with 0.2 wt% and 0.35 wt% Cu and not in steels without copper content. This copper oxide layer is an inert layer that will shield the steel's surface from uniform corrosion as it suppresses the active dissolution of the ferrite phase. However, the problem is that this protective layer cannot cover the entire steel surface. The result of it is the encouragement of localised corrosion, which will be covered in more detail in Chapter 2.3.1.

The above is the first and primary mechanism for copper against corrosion in steel and is valid for all kinds of steel. In summary, the formation of a Cu-enriched layer that protects its underlying structure from reacting with the environment limits uniform corrosion. However, the non-uniform characteristic of the layer can be detrimental in terms of promoting localised corrosion (I. Hong & Koo, 2005; Jang et al., 2009; Ujiro et al., 2001). Hence, the overall effectiveness of this mechanism is the combined effect of both restricting uniform corrosion and encouraging pitting corrosion.

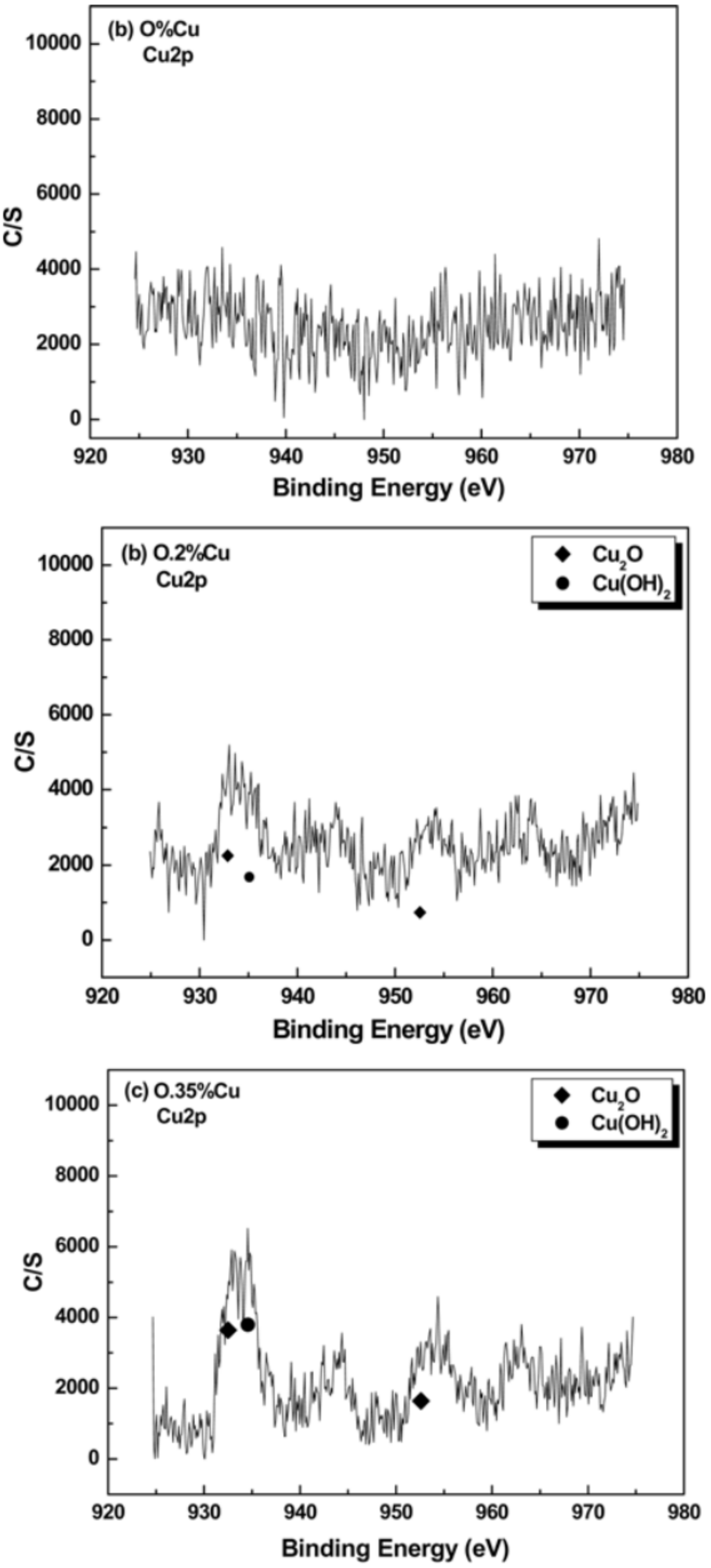

Figure 4: XPS spectra of 0 wt%, 0.2 wt% and 0.35 wt% Cu-containing steels (Jang et al., 2009).

2.1.3 Mechanism 2: Suppression of Galvanic Effect between Different Phases

The second mechanism relates to the nano-sized copper particles deposited on the surface of the steel (Hao et al., 2017). These nano-sized particles can be seen when comparing the SEM images, EDS analysis results and XRD patterns of Cu-free and 0.27 wt% Cu steels immersed in pH 0.85 NaCl solution at 30 ± 2 °C for 288 h, as shown in Figure 5. Its ability to weaken the galvanic effect between different phases leads to the higher corrosion resistivity of steel.

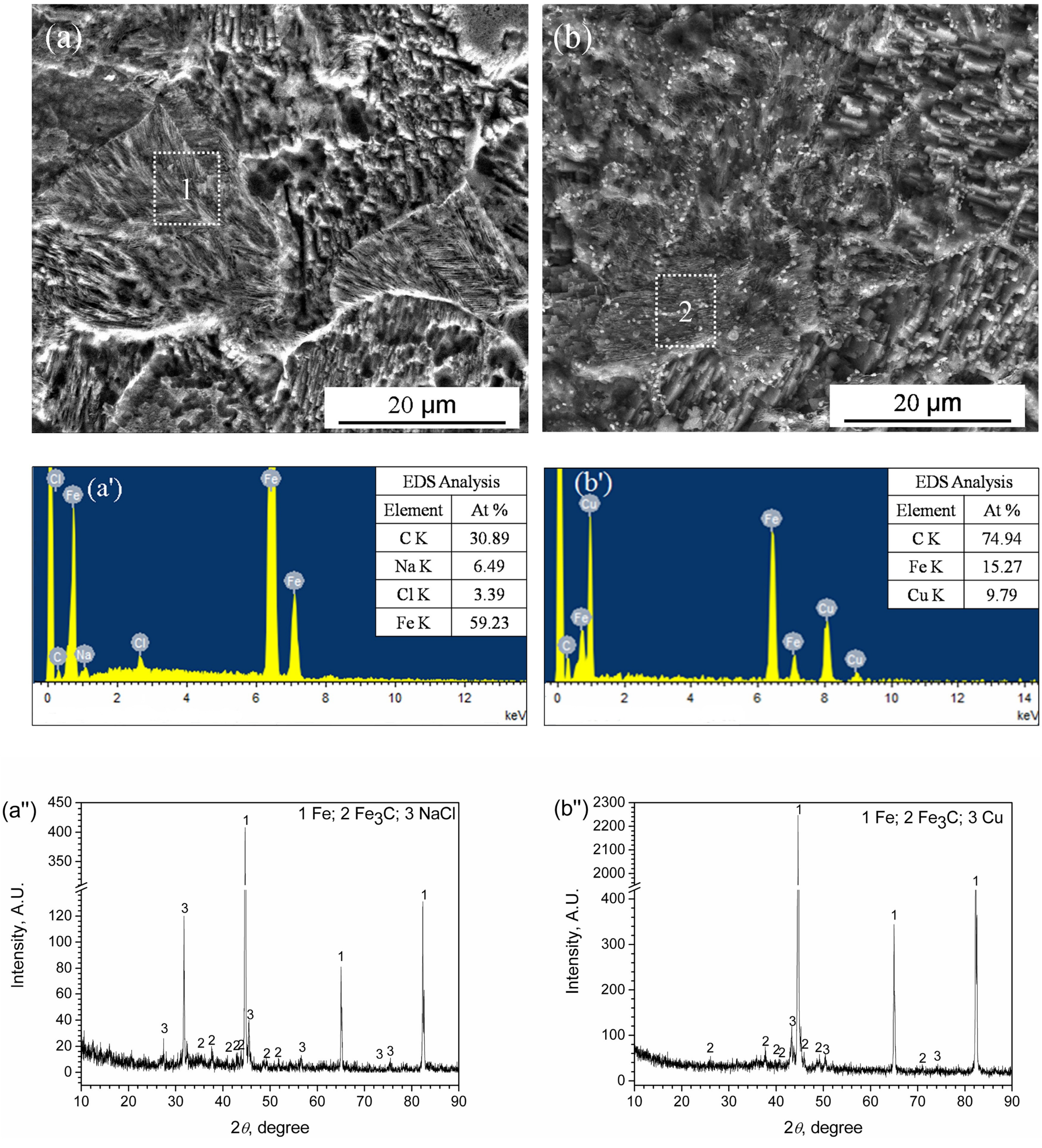

EDS Analysis

Element	At %
C K	30.89
Na K	6.49
Cl K	3.39
Fe K	59.23

EDS Analysis

Element	At %
C K	74.94
Fe K	15.27
Cu K	9.79

Figure 5: SEM images, EDS analysis results and XRD patterns of Cu-free and 0.27 wt% Cu steels immersed in pH 0.85 NaCl solution at 30 ± 2 °C for 288 h (Hao et al., 2017).

For example, most carbon steel contains at least two phases: ferrite and cementite. The presence of the cementite phase will accelerate the corrosion of the adjacent ferrite phase, boosting the galvanic effect. However, the nano-sized copper particles deposited on the surface of the steel can hinder and thus weaken the continuously enhanced galvanic effect between the ferrite and the cementite phases, improving the steel's corrosion resistance (Hao et al., 2017). In addition, micro-galvanic cells are formed between the Cu enrichment layer and the substrate during corrosion. With longer immersion time, more nano-sized Cu particles are accumulated at the surface, resulting in higher hydrogen over-potential suppressing the cathodic hydrogen evolution reaction. Therefore, the corrosion rate decreases with increasing immersion time (J. Hong et al., 2012).

Table 2 gives copper's working mechanism in different steel types. It can be seen that both mechanisms will be available in all different kinds of steel.

Table 2: Mechanisms working in different steel types

Steel type	Mechanism 1	Mechanism 2
Low-carbon steel	Yes	Yes
Low-alloy steel	Yes	Yes
High-alloy steel	Yes	Yes
Medium-carbon steel	Yes	Yes
High-carbon steel	Yes	Yes

In conclusion, during the corrosion of the copper-containing steels, the preferential dissolution of the ferrite phase, the accumulation of the cementite phase, the deposition of nano-sized Cu particles and the formation of a Cu-enriched layer on the steel surface will all occur. However, Cu segregation is undesirable in steel as it compromises the mechanical properties. The details are discussed in Chapter 2.5.1. Hence, a balance needs to be established between enhancing the corrosion resistance and preserving the mechanical strength of the steel.

2.2 Factors Affecting Effectiveness of Copper in Steel

The mechanism for copper against corrosion in steel is highly subjective to the heat treatment, the phases present in the steel, the working temperature and environment, the alloying element, etc. Therefore, in order to gain a brighter picture of the story, a detailed analysis is done of the factors that could affect the effectiveness of copper in steel.

2.2.1 Heat Treatment

Material scientists have proven that the heat treatment process is crucial to the effectiveness of copper. Any change in the parameters will greatly impact the corrosion resistance of steel with copper content. Hence, it is vital to fully understand how each step of the heat treatment can alter the final outcome of the corrosion test.

Using the temperature before quenching as an example, keeping other heat treatment steps unchanged, the selection of this temperature can directly impact the efficiency of copper (Yamanaka et al., 2021). As seen from the SEM, electron probe micro-analyzer (EPMA) elemental map and XPS profiles of steel quenched from 800 and 1100 °C shown in Figure 6 and Figure 7d and j, there is a much higher percentage of copper accumulation at the surface when the temperature before quenched is increased from 800 to 1100 °C. At 800 °C, Cu particles exist only on the matrix, while at 1100 °C, Cu atoms exist on both the martensitic matrix and the carbide phase. As a result, the local electrochemical potential difference between the carbide phase and the martensitic matrix dropped due to enhanced Cu accumulation at the surface, therefore decreasing the corrosion rate by suppressing micro-galvanic corrosion between the constituent phases (Yamanaka et al., 2021). The reduction of the amount of carbide at the surface at 1100 °C also contributes to the drop in local electrochemical potential.

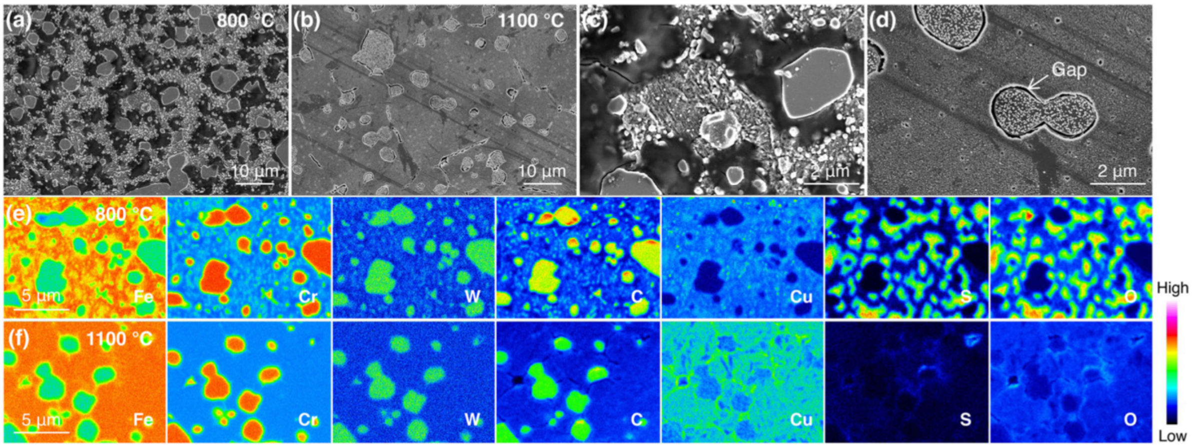

Figure 6: SEM images and EPMA elemental map of high-carbon steel quenched from 800 °C (a, c, e) and 1100 °C (b, d, f) after 1-hour immersion in 0.5 M H2SO4 (Yamanaka et al., 2021).

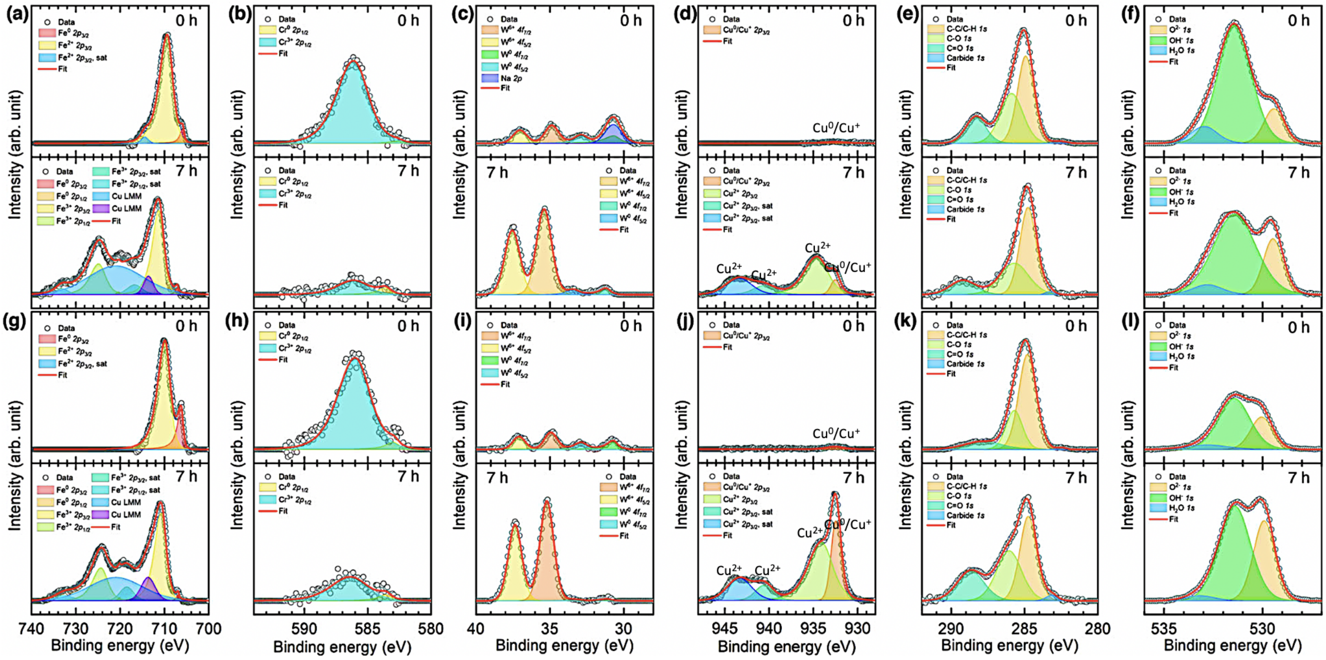

Figure 7: High-resolution XPS profiles of different elements, Fe 2p (a, g), Cr 2p (b, h), W 4f (c, i), Cu 2p (d, j), C 1s (e, k), O 1s (f, l) obtained from the steel quenched at 800 °C (a f) and 1100 °C (g l) before and after 7-hour immersion in the 0.5 M H_2SO_4 solution.(Yamanaka et al., 2021).

In addition to that, the austempering duration and temperature during the formation of the bainite phase/pearlite phase are also critical (Gupta et al., 2023). Austempering is the process of heat treatment where the steel is quenched to a specific temperature and held there for a sufficient period to transform austenite into a bainitic microstructure (Banerjee, 2017). The time taken for the process will have a significant influence on the effectiveness of copper against corrosion. Using 3 types of high-carbon steel with different carbon compositions, B12VA, B14VA and B15VA for 1.18 wt%, 1.02 wt% and 0.97 wt% carbon respectively (Gupta et al., 2023), the effect of austempering time and temperature is explained in detail.

1. Austempering time

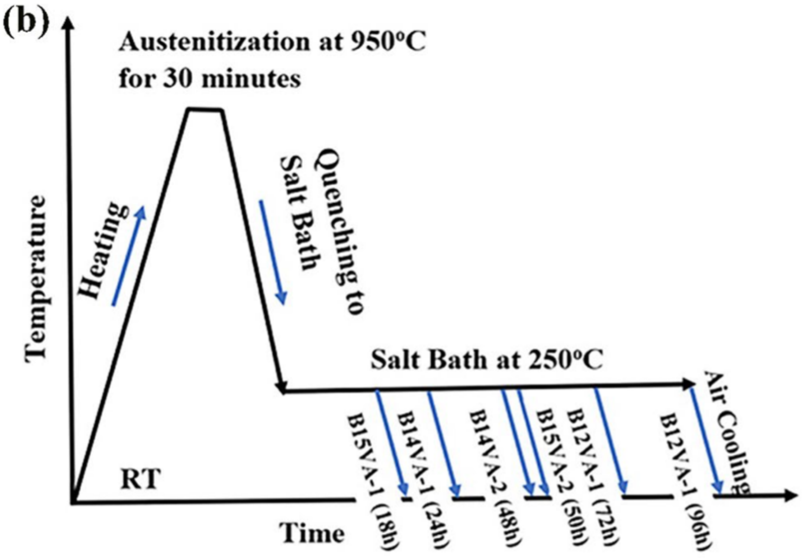

Figure 8: Heat treatment process of B12VA, B14VA and B15VA with different austempering time (Gupta et al., 2023).

- The selection of the austempering time for the steel with an austempering temperature of 250 °C, B12VA, B14VA B15VA, is given in Figure 8. As seen in Figure 9 and Figure 10, retained austenite content reduces with increasing austempering time, thus decreasing the number of galvanic cells created (Gupta et al., 2023) and improving the capability of the steel to resist corrosion. With the accumulation of Cu at the surface, the corrosion resistance of the steel is further enhanced, but to a smaller extent, due to the formation of uniform, compact and non-porous passive layers. Hence, longer austempering time equips the steel with a stronger corrosion resistance ability and limits copper's effectiveness against corrosion when introduced to the steel.

2. Austempering temperature

- P12VA, P14VA and P15VA are the same type of high-carbon steel as B12VA, B14VA and B15VA; the main difference is that the final phase is pearlite instead of bainite. As shown in Figure 9 and Figure 10, austempering at 250 °C results in the formation of bainite phase and retained austenite, while preserving at 550 °C leads to pearlite phase being present (Gupta et al., 2023). Pearlite is a mixture of 2 phases, ferrite and cementite, arranged lamellarly with the two phases alternating (Hillert, 1962). As explained in chapter 2.1.3, the presence of the cementite phase in the steel will accelerate the corrosion of the adjacent ferrite phase, boosting the galvanic effect (Hao et al., 2017). Thus, at the interface between the phases, the initiation of corroded pores begins. As corrosion continues, more pearlite at or adjacent to the grain boundary are etched off, and multiple corroded pores are combined into one pore, enlarging the dimension of the corroded pore (Fu, 2016). With copper added to the steel, the accumulation of Cu at the surface will barricade the pores, thus weakening the continuously enhanced galvanic effect between the ferrite and cementite phases. Hence, at a high enough temperature reheating temperature where pearlite formation begins, copper is more efficient in restricting the corrosion of the steel.

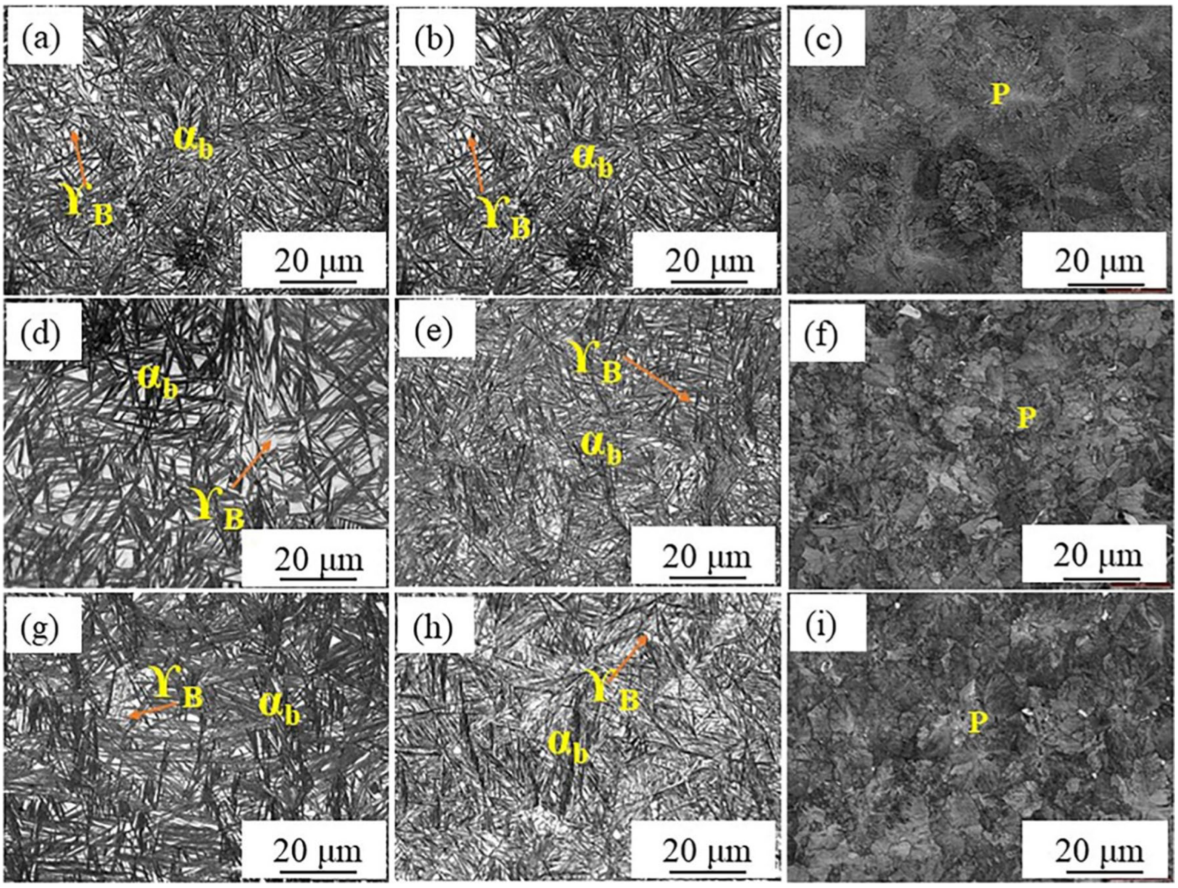

Figure 9: SEM image of the steel austempered at 250 °C with shorter austempering time (a, d, g), 250 °C with longer austempering time (b, e, h) and undergone pearlite transformation at 550 °C (c, f, i) (Gupta et al., 2023).

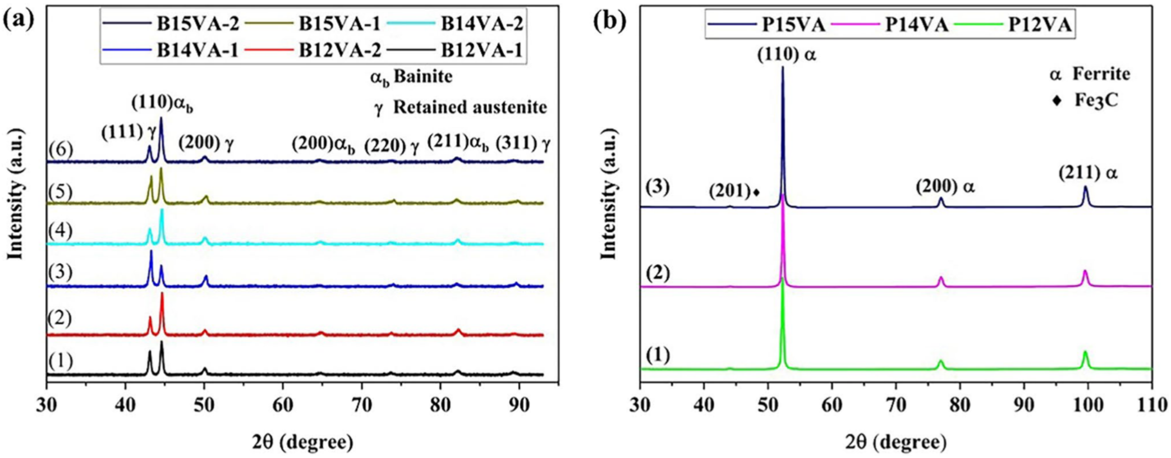

Figure 10: XRD pattern of the steel austempered at 250 °C (a) and undergone pearlite transformation at 550 °C (b) (Gupta et al., 2023).

From the above examples, copper's efficiency level depends predominantly on its microstructure and phases. Hence, studying the phases of the heat treatment end product will help achieve a better understanding of copper's working mechanism against corrosion.

2.2.2 Phases in Steel

The phases present in the steel have a significant influence on the effectiveness of copper. One example that is already mentioned in Chapter 2.1.3 will be the ferrite and cementite phases, in which the presence of both phases can boost the galvanic effect. Copper is, therefore, more effective as it is able to suppress the galvanic while, at the same time, shielding it from further corrosion.

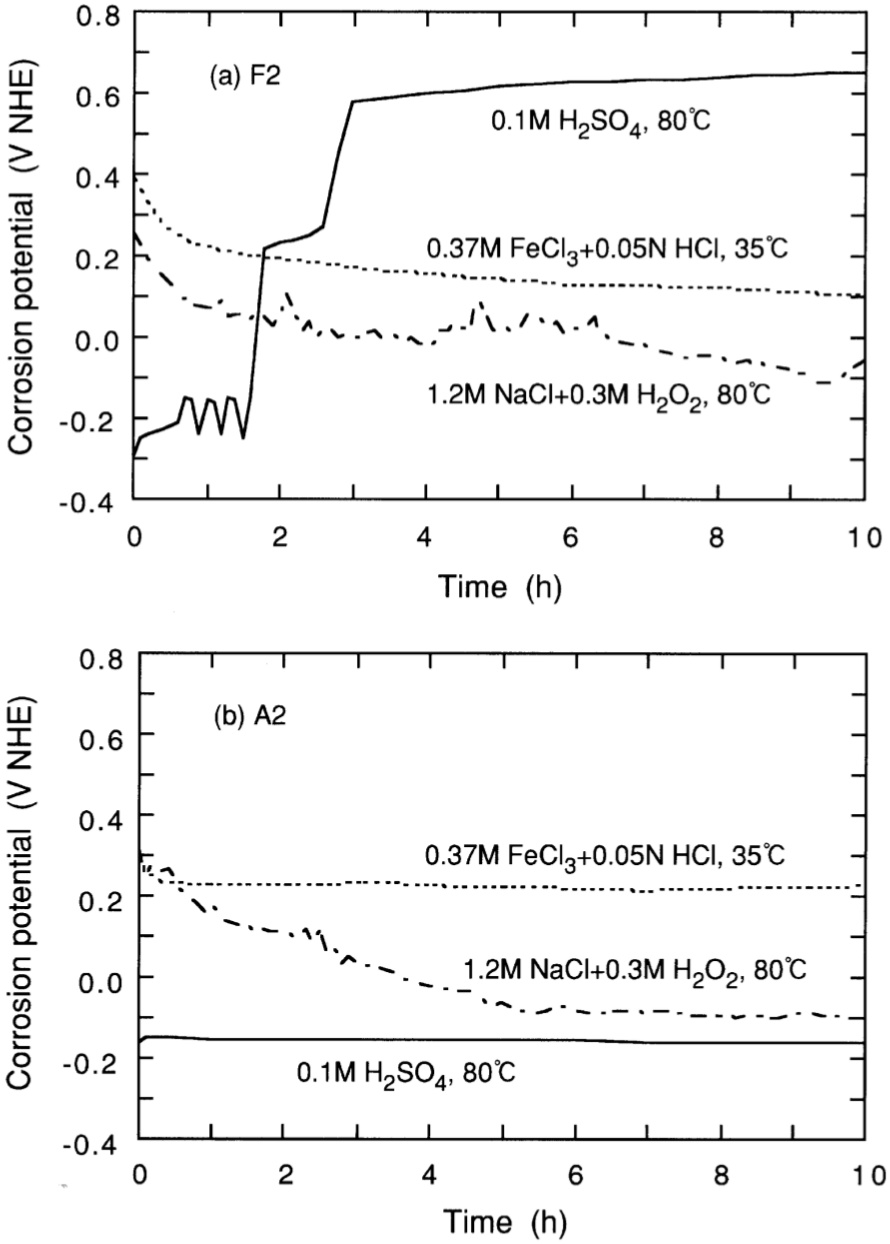

Figure 11: Corrosion potential of ferritic (a) and austenitic (b) stainless steel with Cu in different test mediums over time (Ujiro et al., 2001).

It is also noticed that copper in austenitic steel has a weaker corrosion resistance effect than in ferritic steel, no matter the testing medium (Ujiro et al., 2001). This is shown using Figure 11, where the variation of corrosion potential in austenitic steel in various testing solutions is lower than that of ferritic steel. This is because the ferrite phase's higher active corrosion potential results in easier deposition and accumulation of Cu atoms on the surface of the steel. Also, the deposited Cu will cover the anodic surface of ferritic steel much more uniformly, reducing pitting corrosion (Ujiro et al., 2001). This can be observed from the smaller pitting potential of ferritic steel as compared to austenitic steel in chloride mediums in Figure 12.

Interestingly, copper does not always have a negative influence on pitting corrosion. As long as localised corrosion happens at a high enough active potential range, Cu can have a positive effect against pitting corrosion. The turning point in the potential at which Cu addition switches from beneficial to harmful is much higher for ferritic steel than austenitic steel (Ujiro et al., 2001). This is attributed to the larger active corrosion potential of ferrite inside a pit in the steel. In addition, when limited NaCl is added to the steel, copper has a positive effect on pitting corrosion, as seen from the slope of the line in Figure 12,

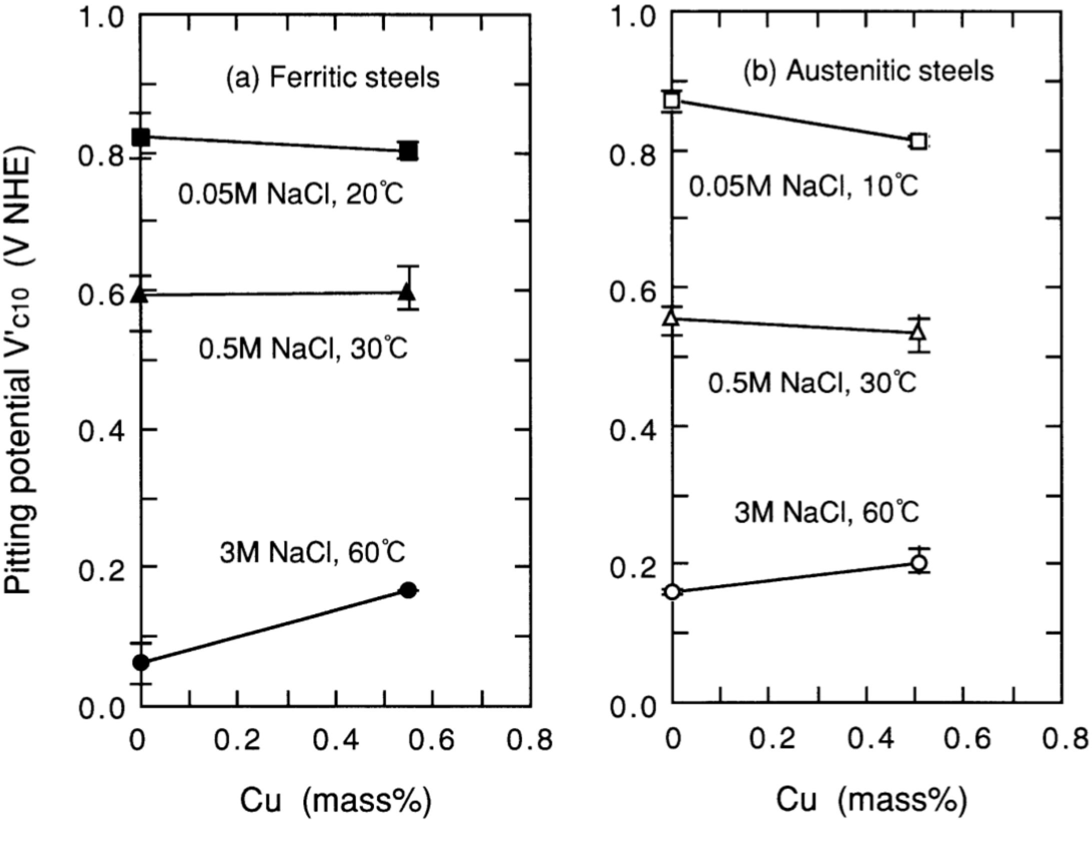

Figure 12: Pitting corrosion of ferritic (a) and austenitic (b) stainless steel in various chloride mediums (Ujiro et al., 2001).

From Chapter 2.2.1, it is understood that the pearlite phase and retained austenite enhanced corrosion while the bainite phase without retained austenite does not, and copper boosts the corrosion resistance of the pearlite phase better than the bainite phase. Also, it is clear that copper suppresses corrosion more effectively in the ferrite phase than in the austenite phase. Next, the effectiveness of copper in the martensite phase is explored by comparing as-cast and quenched high-carbon steel samples.

The as-cast steel contains a very coarse dendritic microstructure that consists of mainly austenite, while the quenched steel encompasses a finer microstructure and has undergone martensitic transformation to form a martensite phase (Zhang et al., 2019). Figure 13 shows that the quenched sample with martensite phase will have a larger corrosion rate. It is the consequence of a finer microstructure that intensifies the number of grain boundaries and interfaces where corrosion is much more susceptible to happen. With copper addition and accumulation at the surface, more areas prone to corrosion are protected, reducing the corrosion rate to a bigger extent than that of as-cast steel. Hence, copper is more effective against corrosion in the martensite phase than in the austenite phase.

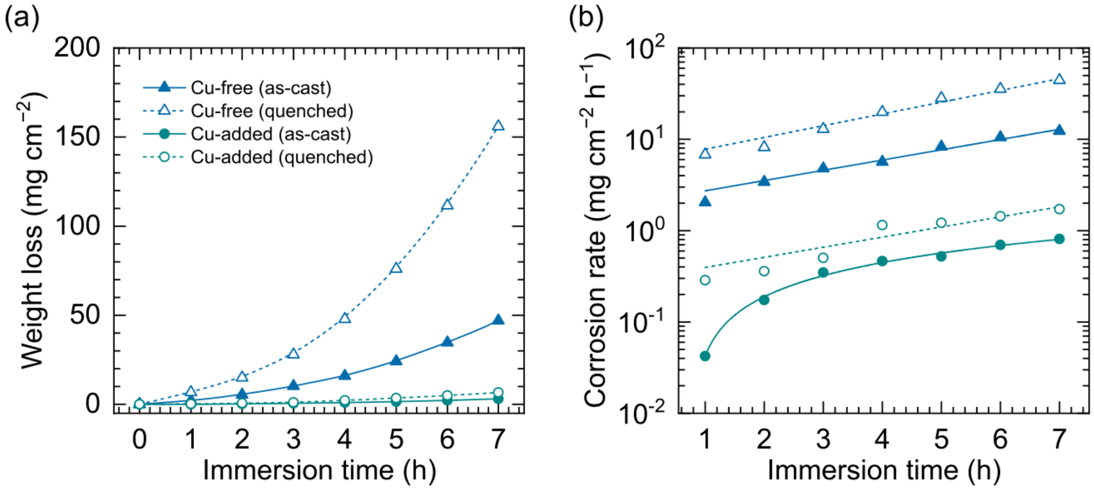

Figure 13: Weight loss (a) and corrosion rate (b) of as-cast and quenched Cu-free and Cu-added steel in H_2SO_4 solution (Zhang et al., 2019).

This section notices a trend: copper works more efficiently in steel samples containing phases more susceptible to corrosion. Hence, despite an actual comparison not being found between the bainite and martensite phases, it is predicted that copper will be more effective in the martensite phase than in bainite, as martensite is more prone to corrode.

2.2.3 Alloying Element

Besides iron and carbon, steel often contains other alloying elements, such as chromium, cobalt, nickel, silicon, manganese, calcium, etc., for better material properties. The presence of these alloying elements may have an adverse effect on the corrosion mechanism of copper. Also, a chromium content of greater than 4 wt% in steel has been well established as effective against corrosion (B. Sun, Zuo, Cheng, & Li, 2020). This raises the question of whether Cu, together with Cr, will lead to an overall improvement or depletion in corrosion resistance of bearing steel, as the high-carbon bearing steel used for the Master Thesis will contain a certain percentage of Cr content.

Choi et al. (2005) did a comparison between 4 different steel specimens, namely low-carbon steel, Cr added low-alloy steel, Cr, Ni and Cu added low-alloy steel, and Cr, Ni, Cu, and Ca added low-alloy steel. The specimens are tested using synthetic tap water in stagnant and flow (1 m/s) conditions. The results, as given in Figure 14, show that with more alloying elements added, the corrosion rate of the steel decreases (Choi et al., 2005). Also, Figure 14 proves that the effect of Cr alone against corrosion in both stagnant and flow conditions is much weaker than when Cr, Cu and Ni alloying atoms are all added. The addition of Ca further suppresses the corrosion rate of the steel. Likewise, Fan et al. (2023) points out that the corrosion resistance of Cr and Cu-added low-alloy steel is much higher than that when only Cr is used. Hence, adding more corrosion-reducing alloy will lead to an overall lower corrosion rate of the steel.

Separately comparing between Cr and Cu atoms, the corrosion resistance effect of 0.5 wt% Cu is stronger than that of 0.63 wt% Cr, with all other elements of the steel kept constant (Xu, Gao, Lv, & Pang, 2016). However, a direct comparison between the different elements is not entirely fair, as the working principle against corrosion of the alloy element is not the same. Cr works more effectively for stainless steel, while Cu is targeted more on micro-alloying steel. Nevertheless, the main subject for the Master Thesis is alloying steel. Hence, it can be concluded that Cu addition is more advantageous than Cr against corrosion in steel in the context of this literature review. A similar conclusion can also be derived when comparing Cu and Sn atoms (Pardo et al., 2006).

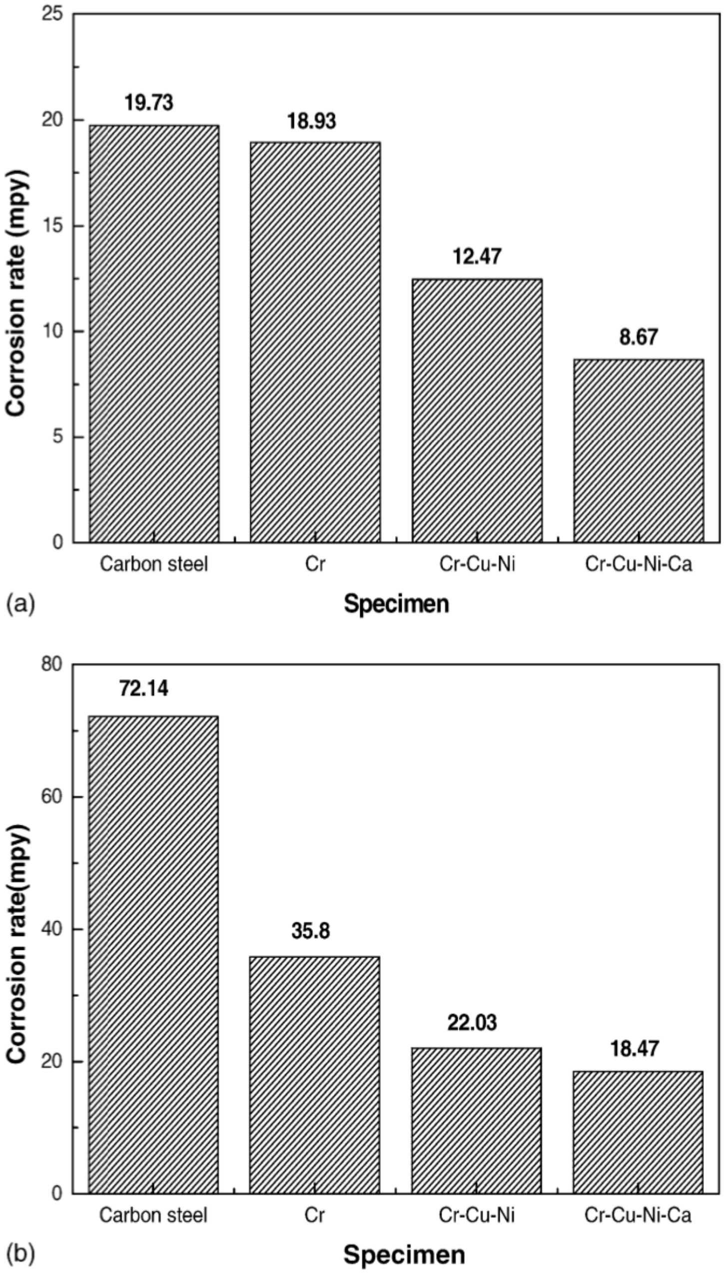

Figure 14: Corrosion rates of specimens in synthetic tap under stagnant and flow (1 m/s) condition respectively (Choi et al., 2005).

2.2.4 Testing Solution and Temperature

The testing solution and temperature do impact the effectiveness of copper against corrosion. Msallamova et al. (2023) points out that the corrosion activity of steels will increase with rising temperature, regardless of the testing environment. This can be shown from the results of corrosion testing with and without Cu at different temperatures using distinctive testing solutions, as seen in Figure 15. Also, it is noted from Figure 15 that the corrosion current density of the 1.51 wt% Cu steel is at least 2 times lower than that of 0.04 wt% Cu steel at all temperatures of exposure in rainwater solution, while for 3.5 wt% Cl^- solution, Cu is less effective against corrosion at high temperature. Both solutions are at around pH 7.

Furthermore, it is noticed that Cu is slightly more efficient against corrosion in rainwater than in 3.5 wt% Cl^- at all temperature ranges (Msallamova et al., 2023). A reasonable explanation was that the alloying elements in the steel can form nano cells in the 3.5 wt% Cl^- environment. These localised nano-batteries can act as a source for pitting corrosion, thus decreasing the corrosion resistance of the steel (Liu et al., 2021).

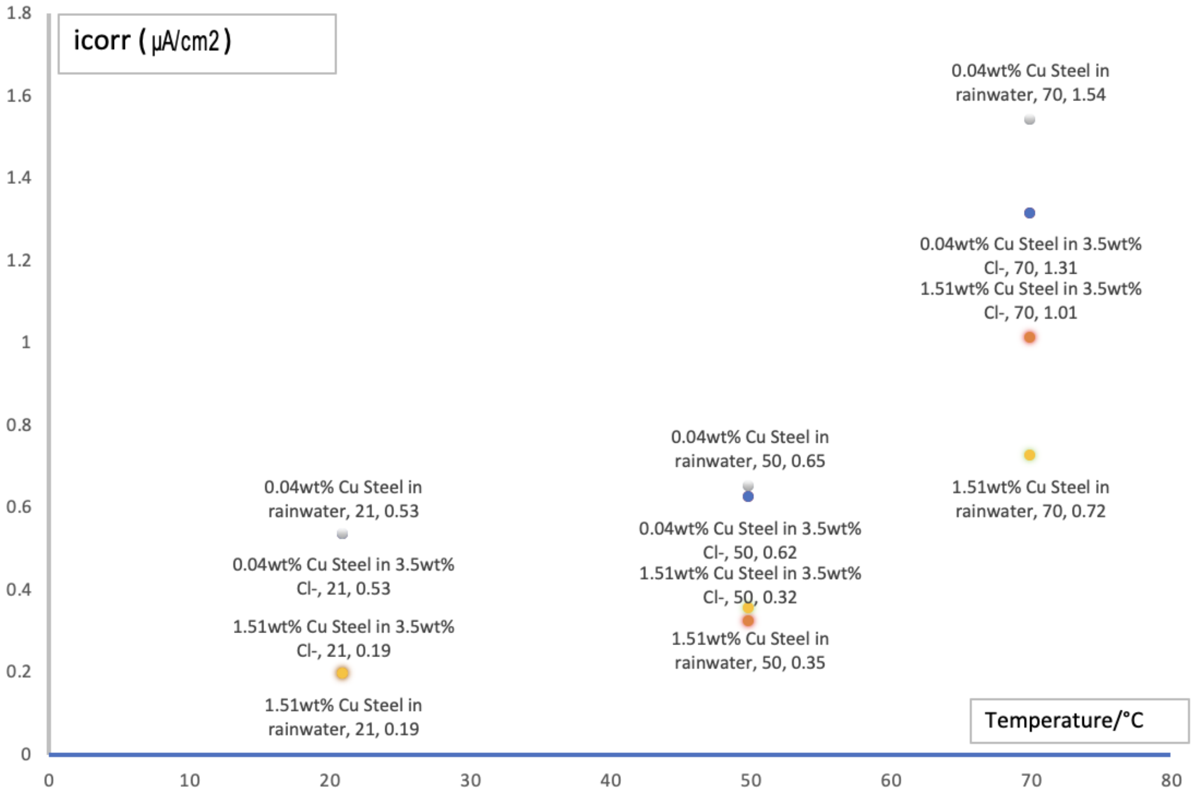

Figure 15: Corrosion density of steel with and without copper at different temperatures in different test mediums (Msallamova et al., 2023).

In addition, Pardo et al. (2006) states that by decreasing the testing temperature from 50 °C to 25 °C, the effect of Cu on the corrosion resistance of steel becomes less significant. This is attributed to the steel's 3 possible electrochemical behaviour in acidic conditions: active, passive or active-passive. Without the availability of Cu, stainless steels presented an active behaviour and a high corrosion rate when immersed in acid at 50 °C. The presence of nano-sized copper particles at the material surface reduces the overpotential of cathodic reaction, enabling the transition of the steel from an active region to a passive one (Pardo et al., 2007). At 25 °C, the behaviour of the steel was preferentially more passive than at 50 °C, limiting the effect of the copper.

Therefore, the temperature of the testing environment and the environment itself might affect copper's effectiveness in restricting steel corrosion. Hence, it is crucial to consider roller bearings' temperature and working condition when selecting the testing medium for the Master Thesis.

In summary, copper will improve the steel's resistivity against corrosion. The mechanism for this is the deposition and, thus, accumulation of nano-sized copper particles at the surface of the steel, forming a protective layer that protects the steel and suppresses galvanic cells. The effectiveness of copper can vary depending on the alloy elements in the steel, the testing environment, the phases in the steel, and the heat treatment process. Hence, it is critical to consider all these factors when designing the experiment for the Master Thesis.

2.3 Disadvantages of Copper on Corrosion of Steel

As mentioned briefly before, the most prominent side effect of copper is the enhancement of localised corrosion, like pitting or crevice corrosion. Additionally, copper harms the steel's strength, hardness and other mechanical properties. The mechanical part of it will be explained later in Chapter 2.5.1 (Xi et al., 2017; Zhang et al., 2019). The following parts will look only into the downsides of copper on the corrosion of steel.

2.3.1 Pitting Corrosion

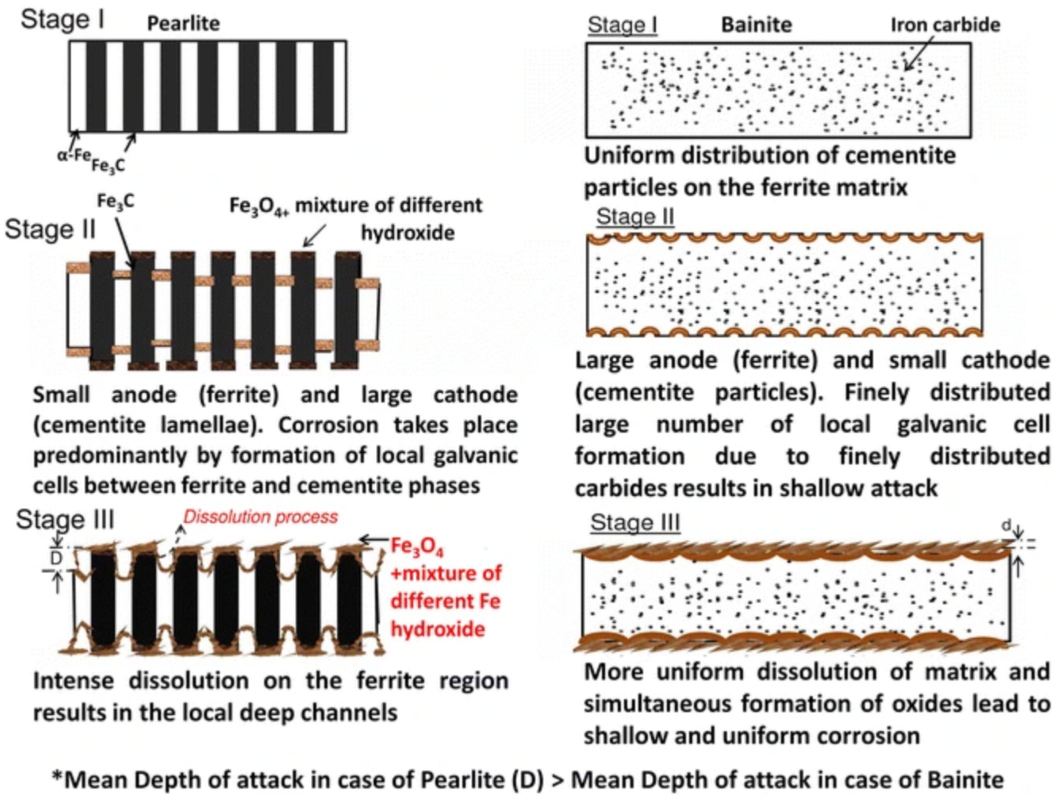

Figure 16: Schematic representation of the corrosion mechanism in pearlite and bainite phase due to the presence of ferrite and cementite (Moon et al., 2015).

Pitting corrosion is a localised type of corrosion that includes the attack of the surface with the formation of shallow holes, deep penetrations or undercuts (Yasakau, Zheludkevich, & Ferreira, 2018). It often involves a localised electrochemical process that is separated into anodic and cathodic parts, with the presence of an electrolyte for the movement of charges.

Using the example of the carbon steel used in Chapter 2.1.3 to explain pitting corrosion, when both ferrite and cementite (pearlite phase) are available in the steel, in the presence of a working electrolyte, the cementite will be the cathode while ferrite is the anode. The ferrite phase will oxidise and dissolve, while the cementite phase remains at the surface. As time moves on, the majority of the surface will be covered by cementite, while ferrite can be found in the holes. Hence, there will be a large cathode (Cementite) and a small anode (ferrite). This results in intense oxidation at the anode, dissolving more ferrite phase and leading to localised, deep penetrations (Moon et al., 2015). The schematic representation of the process in the pearlite and bainite phase can be seen in Figure 16. The explanation also fits well when ferrite and martensite are both present or when cementite particles exist inside the martensite phase, with ferrite/martensite as the anode and martensite/cementite particles as the cathode (Hao et al., 2021).

When added to the system, copper will form a protective layer on the surface that confines the movement of charged particles. However, the protective layer cannot shelter the entire surface and can act as a corrosion cathode. Hence, pitting corrosion happens in regions where the iron is not safeguarded, with the presence of a large cathode (Cu film) and a small anode (Fe). With more Cu on the surface, such localised corrosion is reinforced due to the area effect (large cathode, small anode).

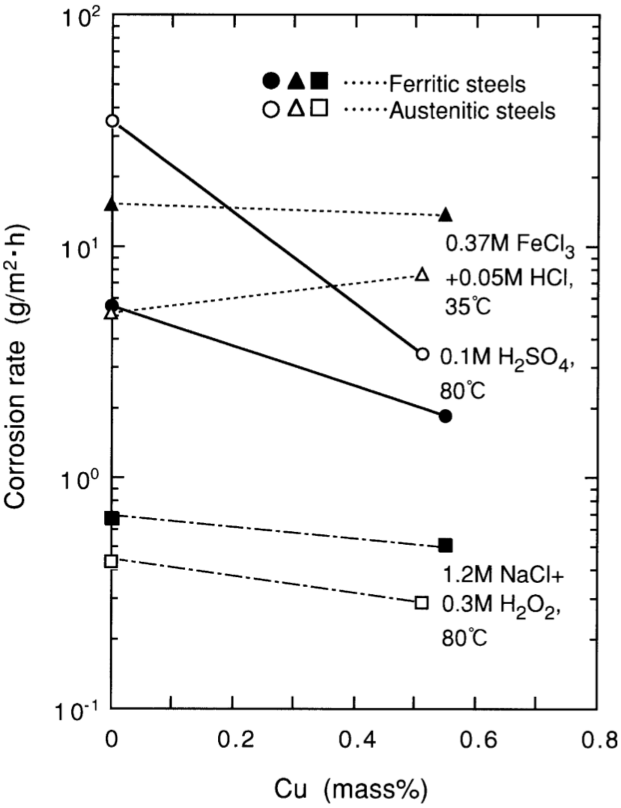

Figure 17: Corrosion rate of austenitic and ferritic stainless steel in different test mediums as a function of the copper content (Ujiro et al., 2001).

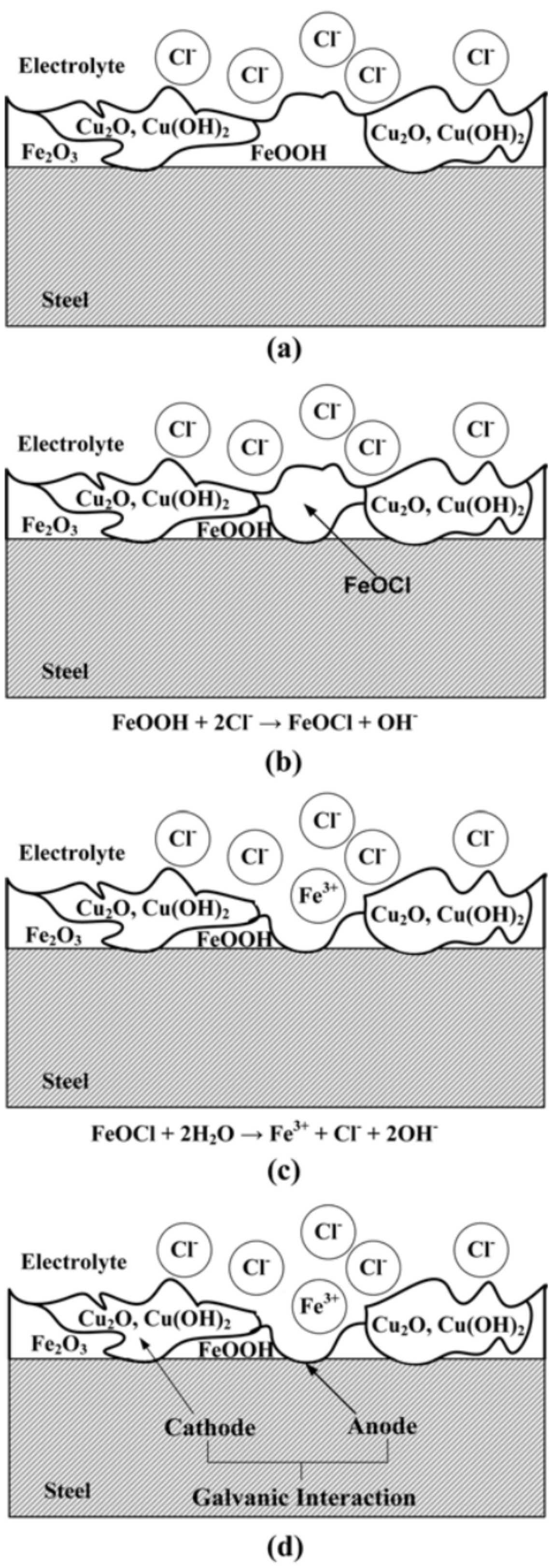

Figure 18: Schematic representation of the corrosion mechanism of steel with Cu in NaCl solution (Jang et al., 2009).

Such an effect is especially prominent when chloride ions are available in the solution used as the medium. Using Figure 17 as an example, when chloride ions are available in the test medium, the overall corrosion rate in ferritic and austenitic steel remains relatively constant despite increasing copper content. For austenitic steel in 0.37 M $FeCl_3$ + 0.05 M HCl at 35 °C, the overall corrosion rate increases with higher copper content (Ujiro et al., 2001). This is because the effect of copper promoting pitting corrosion is more dominant than its capability to restrict uniform corrosion. Therefore, the overall corrosion rises instead of falling.

The reason behind copper's less effective corrosion resistance is the presence of chloride ions, with the entire process schematically illustrated using Figure 18. In this scenario, chloride ions react with the iron oxide layer formed during rusting, thus dissolving it in the chloride solution (Jang et al., 2009). As a result, the iron oxide layer is removed, uncovering the steel under it. As stated in Chapter 2.1.2, Cu_2O and $Cu(OH)_2$ are found on the surface of the steel with Cu. Using the equilibrium potential equation provided in Figure 19, we know that Cu_2O and $Cu(OH)_2$ are more noble compared to iron. This creates a galvanic cell, with the copper oxide as the cathode, the iron as the anode and the chloride solution as the electrolyte. Therefore, the iron corrodes due to galvanic corrosion and the iron oxide layer created preferentially dissolved in the chloride solution, exposing more steel underneath it, and the cycle will continue again endlessly. In addition, due to the area effect (large cathode and small anode), the galvanic interaction is constantly enhanced, accelerating the oxidation at the uncovered sites (Jang et al., 2009). As a result, the pitting corrosion is intensified multiple times, resulting in the formation of deep penetrations.

$$\begin{aligned}
&Fe = Fe^{3+} + 3e^{-},\ E^0 = +0.04\ V_{SHE}\\
&2Cu + H_2O = Cu_2O + 2H^{+} + 2e^{-},\ E^0 = +0.471\ V_{SHE}\\
&2Cu + H_2O = Cu(OH)_2 + 2H^{+} + 2e^{-},\ E^0 = +0.609\ V_{SHE}
\end{aligned}$$

Figure 19: Equilibrium potential equations of the anode and cathode.

Therefore, the accumulation of copper on the surface of the steel and the formation of copper oxides can result in the selective dissolution of more active constituents (Fe), resulting in localised corrosion. However, that is not the only issue. If a high concentration of copper is used in steel, it can lead to the precipitation of the ε-Cu phase in the steel matrix. This effect is linked with the exceeding of the solubility of copper in ferrite or austenite. The presence of the ε-Cu precipitate will decrease the stability of the protective film, promoting anodic polarisation of the steel in certain regions and thus initiating pitting corrosion (Banas & Mazurkiewicz, 2000). The mechanism of how ε-Cu precipitate works is shown in Figure 20. The ε-Cu particles on the passivated film are extremely susceptible to local attacks, causing the depletion of the phase. As a result, the protective film will become discontinued, exposing the steel beneath it (I. Hong & Koo, 2005). Therefore, a galvanic cell with the passivated film as the cathode and the uncovered steel as the anode will form, corroding the steel further. Thus, localised corrosion occurs.

In addition, the ε-Cu phase will also affect the size and distribution of pits, often resulting in very small and deep pits that are difficult to notice (Banas & Mazurkiewicz, 2000). According to research, the copper content of above 3.5 wt% for the austenite phase will initiate the precipitation of the ε-Cu phase (I. Hong & Koo, 2005).

Moreover, when a passive film is already available in the steel to protect it against corrosion (stainless steel), the addition of copper to create a new protective film can cause substantial side effects. It is revealed that adding Cu to such steels will lead to the existence of a duplex passive film structure composed of two oxide layers of distinct semiconductivity (n-type and p-type). Copper's contribution will be the increment of donor and acceptor concentration by

Cu^{2+} ions, making the passive films more susceptible to penetration of insidious ions (Oguzie et al., 2010). The result of it is a discontinued film, thus revealing the steel below it. Hence, Cu enhances the effect of pitting corrosion.

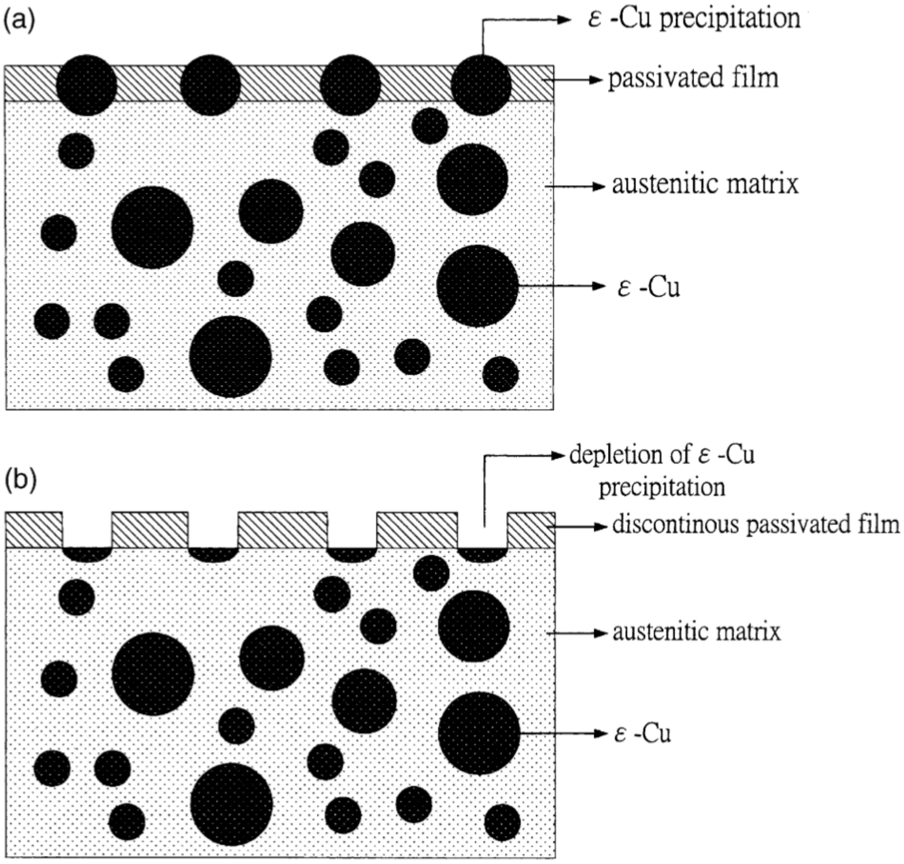

Figure 20: Schematic representation of the effect ε-Cu precipitate on pitting corrosion (I. Hong & Koo, 2005).

The reinforced pitting corrosion due to copper addition is detrimental to the steel's strength and other mechanical properties. Therefore, it is vital to consider the impact of pitting corrosion when applying copper to restrict general corrosion of the steel.

2.3.2 Crevice Corrosion

Crevice corrosion, similar to pitting corrosion, is a form of localised corrosion. The difference is that crevice corrosion occurs on hard-to-reach metal surfaces, such as interstices or gaps between two joining surfaces in which a solution is trapped and not renewed, and depletion of oxygen happens (Syrett & Begum, 2016). Similar to the explanation for the effect of copper on pitting corrosion, the protective film created by the addition of copper is not enough to cover the entire surface, resulting in pit-like areas in the crevice (Xu et al., 2016). Thus, crevice corrosion is enhanced due to the area effect (large cathode and small anode). In addition, if Cr is present in the steel, the reaction to form $Cr(OH)_3$ is more ready to happen compared to Cu, leading to Cu having no effect on the rate of crevice corrosion (Xu et al., 2016).

Likewise, the presence of Cl^- or ${SO_4}^{2-}$ ions in the solution will destroy areas of the protective film, leading to more localised corrosion inside the crevice. Hence, it can be concluded that the presence of copper negatively affects the crevice corrosion rate in steel.

2.4 Effect of Different Content of Copper

Thus far, all the comparisons have been made by looking into steels with Cu and without Cu. It is surprising to find out that if the steel already contains a certain amount of copper, adding more copper to it does not significantly impact the corrosion resistance of the steel, no matter the testing medium (Díaz et al., 2018).

Figure 21 gives the corrosion rate of steel with 0.25 wt%, 0.50 wt% and 1.00 wt% Cu in various atmospheric conditions for a period of 2 and 5 years. It can be seen that increasing the copper content of the steel from 0.25 wt% to 1.00 wt% only produces a very slightly higher corrosion resistance in the different atmospheric conditions (Díaz et al., 2018). Therefore, it can be concluded that adding more copper is not worth the price as it compromises the strength of the steel without significantly benefiting its corrosion resistance.

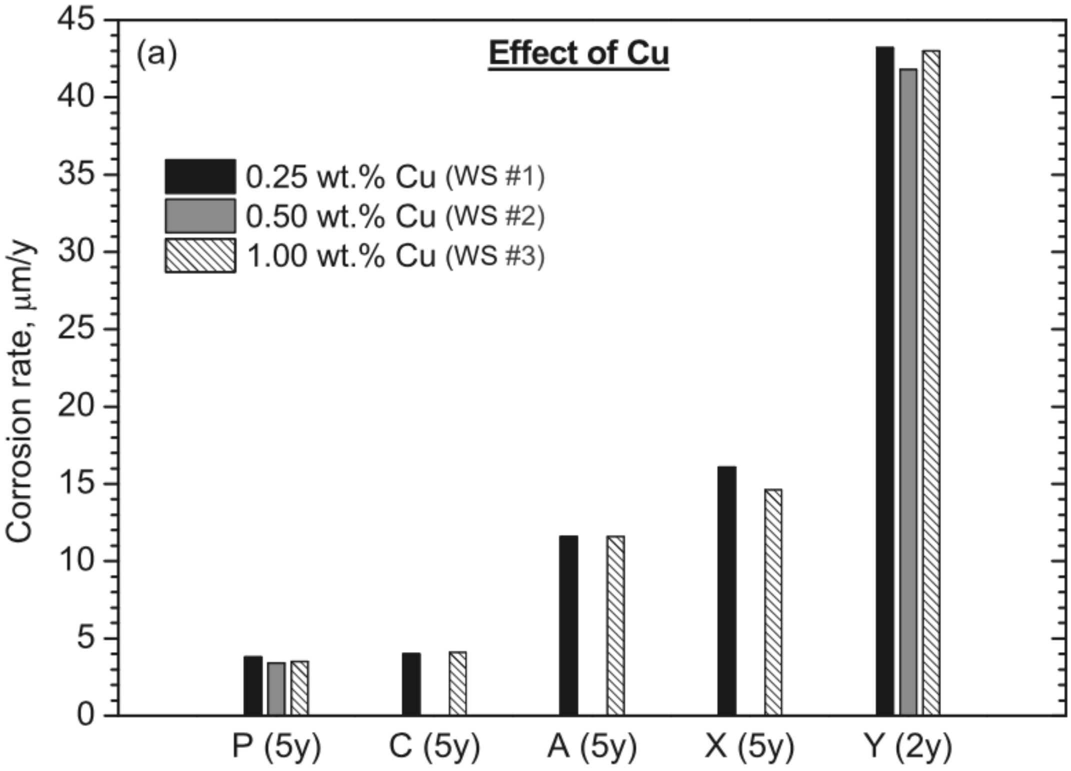

Figure 21: Effect of copper content on the corrosion rate of steel in various atmospheric conditions, with P being urban environment, C being city environment, A being SO_2-limited industrial environment, X being SO_2-dense industrial environment, Y being marine environment (Díaz et al., 2018).

2.5 Impact of Copper on other Properties

Copper's effect on steel is not limited to corrosion. Properties like strength, toughness, and hardness are also affected by the introduction of copper to steel (Sekunowo et al., 2014). Hence, it is crucial to analyse copper's impact on other aspects of steel to determine the overall outcome of the steel's performance. From there, a more conscious decision can be made regarding the application of copper on high-carbon bearing steel.

2.5.1 Mechanical Properties

The mechanical properties of steel are the part that copper brings the most disadvantage to. It has been proven that the presence of greater than 0.25 wt% Cu in steels will lead to the formation of complex compounds that cause microstructure distortions, which in turn results in vital losses in the mechanical strength of steel (Cavaliere, 2023). Also, the precipitation and growth of the ε-Cu particles will diminish the yield strength and ultimate tensile strength of the steel further (Y. Sun, Zhong, & Wang, 2019). This is the outcome of the copper content in the steel matrix exceeding the maximum tolerated level (maximum allowable Cu content before a negative effect on properties of steel occurs), resulting in the diffusion of copper into the grain boundaries and surface. The following is a discussion of the impact of copper on specific mechanical properties.

1. Hardness
    - The Vickers hardness of the steel will drop when copper is included in its composition (Sekunowo et al., 2014; Zhang et al., 2019). With increasing copper content, the hardness of the steel will continue to decrease, as shown in Figure 22a.

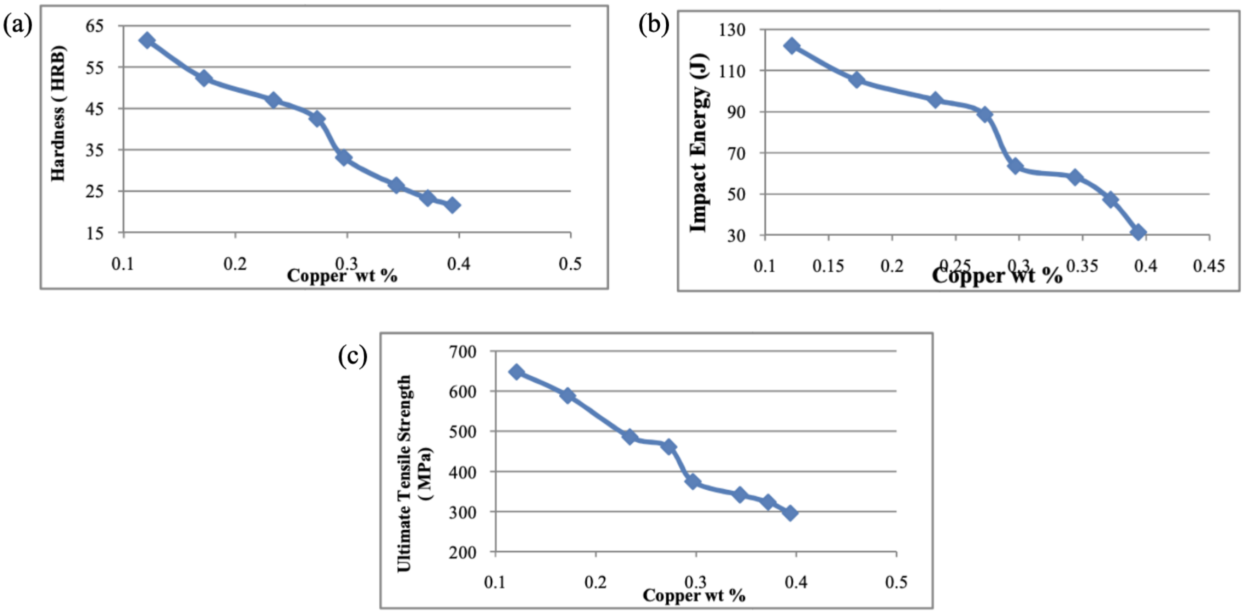

Figure 22: Effect of copper variation on the (a) hardness, (b) impact energy, (c) ultimate tensile strength of low-carbon steel (Sekunowo et al., 2014).

2. Impact toughness
    - The impact test done on steel with and without copper demonstrated a significant drop in impact toughness when copper is added (Salvetr et al., 2023; Sekunowo et al., 2014). Impact toughness indicates the toughness of a material and is calculated by finding out the amount of energy that a material is able to absorb before rupturing (Wu, 2017). A material with high toughness is indicated by its high impact energy. Figure 22b shows the variation of impact energy and, therefore, impact toughness with copper.

3. Ultimate tensile strength

- Ultimate tensile strength takes a downward trend with increasing copper content (Sekunowo et al., 2014; Xi et al., 2017), as given in Figure 22c. However, yield strength and ultimate tensile strength can take an upward trend after heat or ageing treatment with higher copper content (Salvetr et al., 2023; Xi et al., 2017). This is because, with the right treatment, the steel would separate large amounts of nanoscale-size Cu-rich precipitates from the steel matrix. These randomly distributed Cu-rich precipitates would accumulate and pin the dislocations during the deformation process, thus effectively enhancing the strength of the steels (Xi et al., 2017).

Therefore, when applying copper to cope with the corrosion of high-carbon bearing steel, it is critical also to consider its detrimental effect on the mechanical properties and find a balance between the two factors.

2.5.2 Antibacterial Properties

Another effect of copper is its ability to limit the growth of bacteria. As shown in Figure 23, with higher copper content, fewer bacteria can grow on the steel, thus improving the antibacterial properties of the steel.

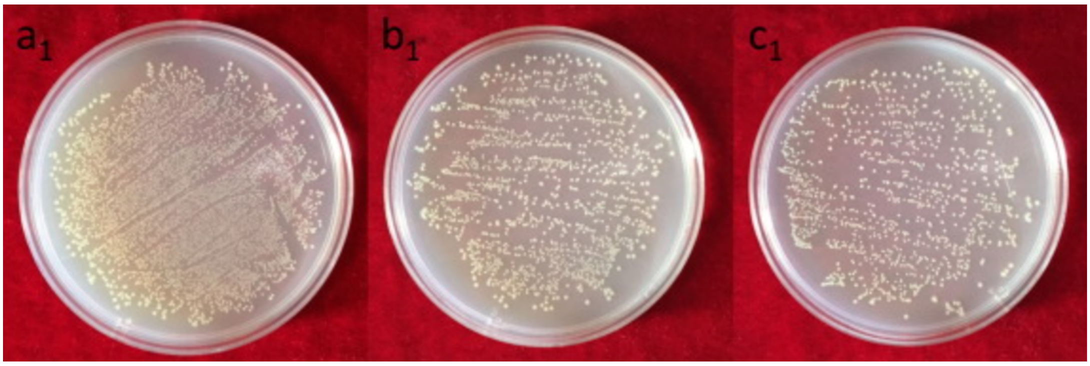

Figure 23: Photos of bacterial colonies for steels in Escherichia coli suspension at 37 °C for 24 h: (a) steel without Cu, (b) steel with 2.5wt% Cu and (c) steel with 3.5wt% Cu (Xi et al., 2017).

2.6 Summary of the Literature Review

In conclusion, a mild amount of copper is effective against corrosion in steel by the deposition and accumulation of nano-sized copper particles on the surface of the steel. However, these copper particles and copper oxide on the surface can act as a cathode to form a galvanic cell with the iron that is not protected, leading to pitting corrosion. The problem is also enhanced due to the area effect, which is the presence of a large cathode (ferrite) and small anode (Copper oxide). In addition, the presence of other alloying elements, such as Cr, Ni, Mn, etc., might also interfere with Cu, leading to weaker corrosion resistance.

The condition of the testing medium is also crucial. Temperature, the presence of Cl- ions, etc., will all lead to an increased corrosion rate. The phases inside the steel, the quenching temperature, austempering time, etc., of the heat treatment process will also play a part in altering the effectiveness of copper. Therefore, it is vital to consider all factors when determining the efficiency of copper against corrosion of high-carbon bearing steel.

2.7 Research Gaps and Research Questions

The relevant information about the effect of copper on steel corrosion has been listed. However, while this explained many observations and scenarios, it also raised many new questions on the topic.

1. Extent of effectiveness
    - It is confirmed that copper has two opposite effects on the corrosion of high-carbon bearing steel, suppressing uniform corrosion and promoting pitting corrosion. In addition, the conditions of the testing solution will influence the corrosion rate of steel (Cl- ions improve pitting corrosion, and temperature increases the corrosion rate). Hence, under the circumstances of roller bearing, it is unsure whether copper will bring stronger corrosion resistance to the steel or weaken it. If the corrosion resistance is boosted, to what extent is the improvement?
2. Phases
    - As mentioned in Chapter 4.3, the phases have an impact on the corrosion rate and, thus, the effectiveness of copper. Ferrite, cementite, pearlite, bainite and martensite phases have all been researched, but there are no articles that compare the corrosion of the phases with the addition of copper in high-carbon bearing steel. Hence, it is unclear which phase will be most effective against corrosion, which is not, with the addition of copper.
3. Presence of Cr content
    - The 100Cr6 bearing steel used for the Master Thesis will contain a certain amount of Cr. The addition of Cr, like Cu, will inevitably increase the passivation tendency of the material's surface (B. Sun et al., 2020). The study of stainless steel also states that Cr and Cu can have an interfering effect on corrosion resistance. However, the claim is made when testing steels with a very high Cr content. It would be interesting to determine whether a low Cr content will also lead to such an interfering effect.
4. Increasing copper content
    - It is stated in Chapter 2.4 that a change in the copper content in steel creates a negligible difference in its efficiency against corrosion. However, when doing research, only one source points towards this fact and the source involves a 5-year corrosion test using the weight-loss method in atmospheric conditions (Díaz et al., 2018). It is believed that five years is too long for the corrosion test, and many other factors could possibly alter the corrosion results during the duration. Hence, more evidence is needed to show that the point is valid.
    - In addition, in chapter 2.5.1, it is stated that higher copper content has a detrimental effect on the mechanical properties of the steel. Hence, the selection of copper should be done in a way that maximises the performance of the steel and minimises the compromising of any properties.

Bearing all this in mind, the main research question for the Master Thesis will be structured in this manner:

What is the effect of copper on the corrosion of high-carbon bearing steel with a martensite/bainite microstructure?

The sub-research question for the topic will include:

1. To what extent will copper be efficient against corrosion in high-carbon bearing steel?
    - This sub-research question is directed at the effectiveness of copper against corrosion. Corrosion tests will be carried out for both steel samples with and without copper. By comparing the difference in corrosion rate, the effectiveness of copper is determined.
2. What are the phases in high-carbon bearing steel that will be most effective against corrosion by the addition of copper?
    - This sub-research question aimed at the effect of different steel phases on the corrosion resistance ability of copper-added steel. This is done by comparing the corrosion rate of copper-added steel with different phases using a corrosion test. Moreover, the steel surface after corrosion will be observed using LOM, SEM, and EDS to discuss the corrosion mechanism of the phases further and how copper could affect the results.
3. In a high-carbon bearing steel alloyed with only a mild amount of Cr and Cu, will there be an interfering effect that would weaken the corrosion resistance of the steel?
    - This sub-research question aimed to discover the possibility of an interfering effect between Cr and Cu. This is done by analysing the surface of steel with and without copper using surface analysing techniques such as SEM, EDS, XRD and XPS to find out the possibility of a double passive layer on the surface of the corroded steel sample. From there, a conclusion will be made about the tendency for an interfering effect to exist.
4. Will tolerating more residual copper further impact the corrosion resistance of the high-carbon bearing steel?
    - This sub-research question is targeted at the effect of different copper content on the resistibility of the steel to corrosion. However, to answer this question, a corrosion test must be done for steel with different percentages of copper content. This is not possible for this report and, hence, will not be investigated here.

3 Experimental Procedure

The main objective of the study is to analyse the effect of copper on the corrosion mechanism of high-carbon bearing steel. It also focuses on answering the sub-research questions listed in Chapter 2.7. As concluded from the literature review in Chapter 2, the phases inside the steel and the test environment influence copper's effectiveness in corrosion. Therefore, to select the most optimum corrosion test and treatment process, a simple study was done on the possible testing methods and treatment options to be considered in this Master's Thesis before finalising the experiment plan.

This chapter details the material composition, heat treatment process, and techniques used for corrosion and microstructure analysis.

3.1 Materials

SKF B.V. provided two variants of high-carbon bearing steel. One represents the chemical composite of standard 100Cr6 steel produced by industrial ore-based steelmaking routes, while the other (100Cr6Cu) was a lab melt produced by adding chromium and 0.5 wt% copper to pure iron. Their actual compositions are provided in Table 3. The samples were cylindrical with a diameter of 4 mm and a length of 10 mm. A total of 18 samples, 9 for each type of steel, were used in the experiments.

Table 3: Chemical composition of the 100Cr6 bearing steel in wt%

Steel	C	Mn	Si	Cr	Cu	Ni	Fe
100Cr6	0.96	0.32	0.29	1.43	0.03	0.04	Balance
100Cr6Cu	0.97	0.37	0.22	1.40	0.46	0.25	Balance

3.2 Heat Treatment

Chapter 2.2 show that heat treatment parameters influence the fraction and composition of the different phases in the steel, therefore impacting copper's effectiveness on corrosion. Hence, it is critical to study the heat treatment process to achieve control of most of the microstructures during the test. The phases that will be of interest for the project are martensite with different degrees of tempering and lower-bainite.

3.2.1 General Guidelines

The continuous cooling transformation (CCT) diagram for 100Cr6 bearing steel is shown in Figure 24. This CCT diagram does not correspond 100% to the steel used in the Master Thesis, as CCT diagrams are significantly dependent on the initial microstructure, austenitisation temperature and time, heating rate, cooling type, actual steel composition and residual element contents, etc. Nevertheless, it can still be used as an indication of expected phases formed during different heat treatments.

Two types of heat treatment were planned for the Master Thesis: type 1 for the formation of martensite with different tempering degrees and type 2 for the formation of bainite.

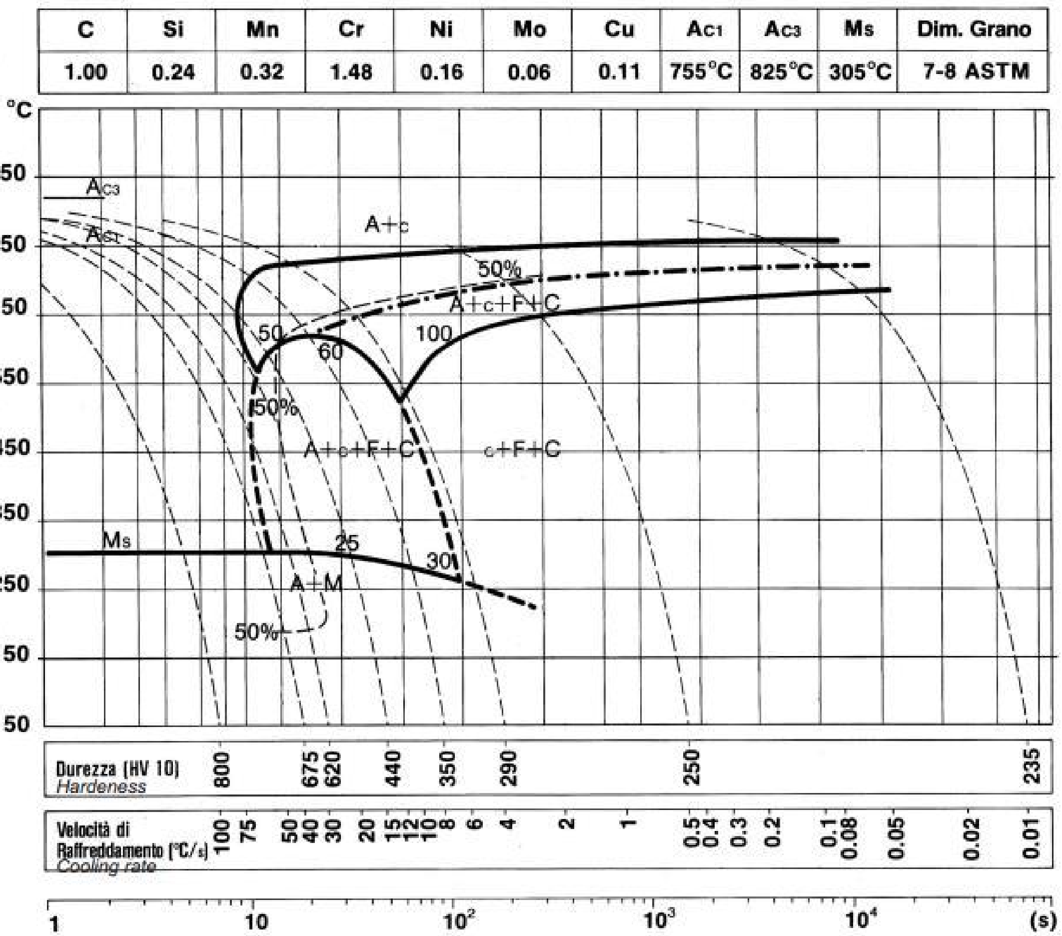

C	Si	Mn	Cr	Ni	Mo	Cu	Ac1	Ac3	Ms	Dim. Grano
1.00	0.24	0.32	1.48	0.16	0.06	0.11	755°C	825°C	305°C	7-8 ASTM

Figure 24: CCT diagram for 100Cr6 bearing steel (Tran et al., 2017).

1. Type 1 heat treatment

   Type 1 heat treatment includes a process known as tempering. It is used to improve the toughness and decrease the hardness of the steel that has been through-hardened by heating it to form austenite and then quenching it to form martensite. The treatment first involves heating the steel to the austenite region and maintaining it for some time for austenite transformation. The austenitisation temperature should be in the range of 850 to 900 °C, and the time should be between 15 and 30 minutes to ensure complete austenite transformation. Then, it is quenched to room temperature to form the martensite phase. The CCT diagram in Figure 24 visually explains the process. After quenching it to room temperature, it is reheated again to the tempering temperature, which is selected between 125 °C and 700 °C, for some time (Industrial Metallurgists, LLC, n.d.). Then, it is air-cooled to room temperature.

   For this project, two tempering conditions were selected.

   (a) A very low tempering temperature between 150 and 200 °C to keep part of the retained austenite untransformed.

   (b) A higher tempering temperature between 200 and 250 °C to transform most of the retained austenite from the matrix.

2. Type 2 Heat Treatment

   Type 2 heat treatment aims at the formation of bainite through a process known as austempering. The austenitisation part of type 2 is similar to type 1. After that, the steel is oil-quenched to the austempering temperature and remains there for some time. Then it is air-cooled to room temperature (Foster et al., 2022). The austempering temperature and time should be selected to ensure bainite formation. For lower bainite, the austempering temperature should be between 250 and 400 °C, and the austempering time should be of at least 1.5 hours.

3.2.2 Final Settings

The samples taken from each type of steel were divided into three batches, which were hardened into three distinctive microstructures. They were martensite with two degrees of tempering (160 °C for one hour and 240 °C for one hour, leading to TM-160 and TM-240, respectively) and lower-bainite (B).

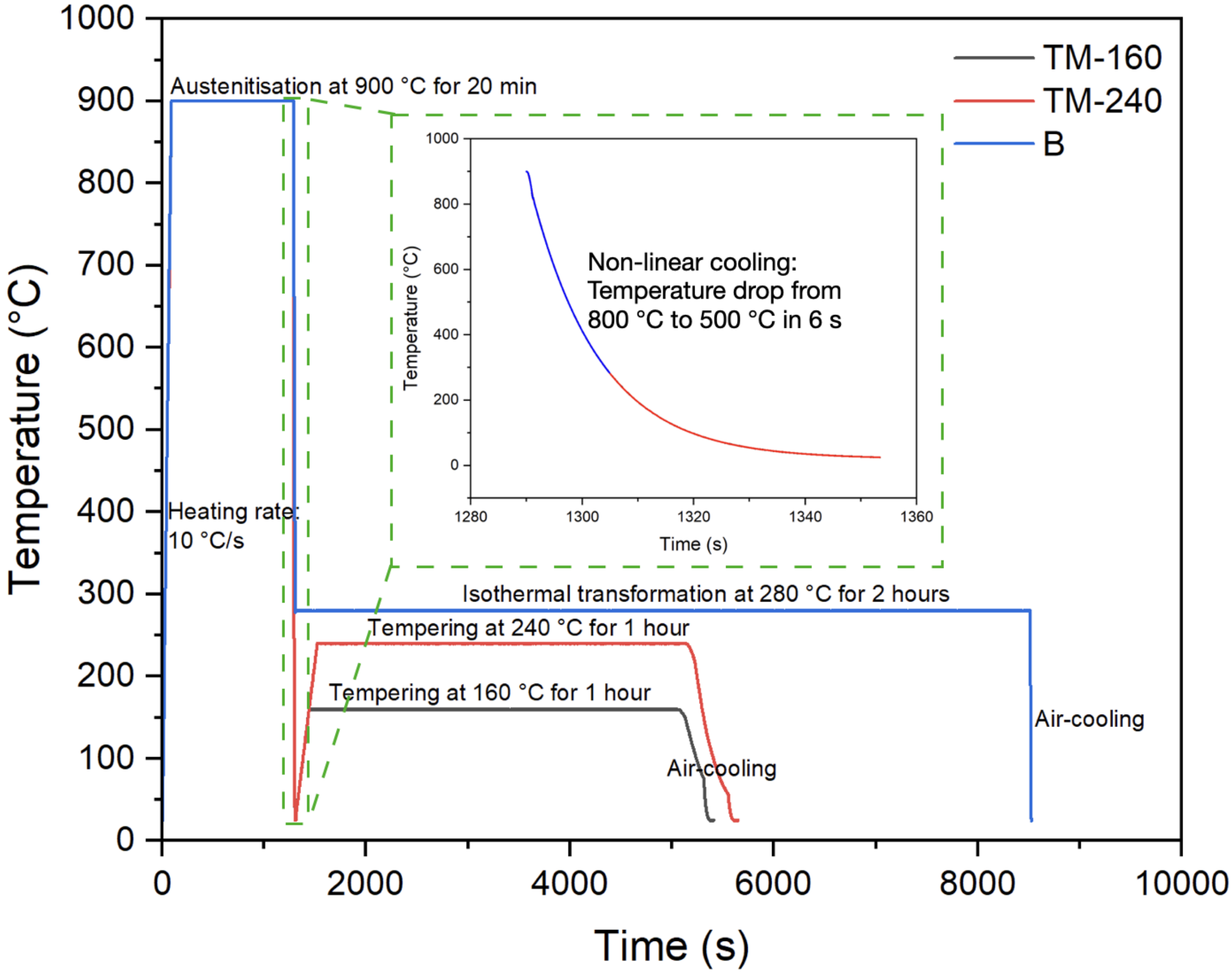

Figure 25: Heat treatment process for the bearing steel.

A DIL805 quenching dilatometer was used for the heat treatment. To obtain the desired phases, the steel samples were first heated to the austenitising temperature of 900 °C at 10 °C/s in the DIL805 quenching dilatometer and remained there for 20 minutes. The steel then underwent a non-linear cooling to room temperature for both martensites and to 280 °C for bainite. The non-linear cooling was constructed in such a way the temperature should drop from 800 °C to 500 °C within 6 s. Helium gas was used for the cooling. TM-160 was then reheated at 10 °C/s to 160 °C and remained there for an hour before air-cooling it back to room temperature. TM-240 underwent a similar process at 240 °C. B was treated at 280 °C for 2 hours before air-cooling back to room temperature. Figure 25 illustrates the entire heat treatment process. Each heat treatment process was repeated three times for each type of steel. The final air-cooling step was not critical.

3.3 Microstructure Characterisation

Microstructure analysis was done on the steel surface before and after corrosion using techniques such as Light Optical Microscopy (LOM), Scanning Electron Microscopy (SEM), Energy Dispersive X-ray Spectroscopy (EDS), X-ray Diffraction (XRD) and X-ray Photoelectron Spectroscopy (XPS). Benchmarking was performed using the surface before corrosion. After corrosion, attention shifted to corrosion products, corrosion type, and the impact of copper.

3.3.1 Light Optical Microscopy

The samples, after heat treatment, were first embedded using conductive resin. Next, the sample surface was metallurgically prepared, by finishing with SiC abrasive papers of a grit size of 2000 and polishing with 3 and 1 µm polishing liquid. The steel was then cleaned with isopropanol in an ultrasonic bath for 20 minutes. Afterwards, it was etched with a 2 vol.% Nital solution. The polished and etched surfaces of the uncorroded steel samples were then observed under the VHX 7000N Digital Microscope to determine the phases present in the steel. Similarly, the corroded samples were seen under the LOM to check the type of corrosion that occurred during the corrosion test.

3.3.2 Scanning Electron Microscopy and Energy Dispersive X-ray Spectroscopy

An SEM-JSM-IT 100 was used to identify the phases in the uncorroded steel samples, with EDS trying to find out where the copper lies in the steel matrix. Also, the surfaces of all oxidised steel samples were studied using SEM combined with EDS to examine the morphology and corrosion product.

3.3.3 X-ray Diffraction

XRD was performed on the corroded steel samples, which were put in holder SD-52, using Bruker D8 Advance diffractometer Bragg-Brentano geometry with graphite monochromator and Vantec position sensitive detector. Co Kα radiation was used, with a voltage of 40 kV and a current of 40 mA. The detailed settings included the use of divergence slit V6, scatter screen 5 mm, and lead slaps on the right and left side of the sample. No spinning was applied. Coupled θ -2θ scan, step size was 0.042$^{\text{o}}$ 2θ, counting time per step was 4 s, 2θ range was from 25 $\sim$ 105.

The oxidised layer was closer examined by a two-dimensional (2D) XRD machine with a smaller beam size at three different locations of the corroded bainitic steel with 0.5 wt% Cu. 2D XRD refers to XRD applications with two-dimensional detectors and corresponding data reduction and analysis. The 2D diffraction pattern contains far more information than a one-dimensional profile collected with the conventional diffractometer (He, 2003). Hence, it can do a more in-depth study of the phases and chemical composition of the steel surface.

The instrument used here was Bruker D8 Discover diffractometer, Incoatec Microfocus Source (IµS). The sample was put on a standard holder. Cu Kα radiation was used, with a voltage of

50 kV and a current of 1000 µA. The detailed settings included using Montel Optics ELM32 with parallel beam, UBC collimator 0.5mm, UMC 1516 sample stage, and Eiger 2 500k detector. Coupled θ -2θ scan, step size was 0.05º 2θ, counting time per step was 6 s and 2θ range was from 20 $\sim$ 70. This XRD technique has a much lower penetration depth and thus can better examine the corroded steel's surface. All data evaluations were done by using the Bruker software DiffracSuite.EVA vs 7.1 and comparing the peaks in the XRD pattern with the database. A pre-selection of data was done by checking the expected oxides and phases in the steel. The peaks that had not yet been determined were checked by doing a specific search in the database.

3.3.4 X-ray Photoelectron Spectroscopy

XPS was performed to examine the chemical composition of the corrosion layer on the corroded steel surfaces. Sputtering was not done on the sample surface to avoid damage to the corrosion layer. A comparison between the corroded and uncorroded steel surfaces was also made. Peak fitting was done for the XPS results against adventitious carbon, a thin layer of carbonaceous material commonly found on the surface of most air-exposed samples (Biesinger, 2015). Its presence provides a convenient charge reference by setting the main line of the C 1s spectrum to 284.8 eV. The results were then analysed to determine the relative amounts of different chemical states contributing to a spectrum by comparing the data with the database.

3.4 Corrosion Test

Since the application of high-carbon bearing steel in roller bearings often involves a neutral environment of around pH 7, the testing solution will be at pH 7 in this Master Thesis to create conditions closely related to the actual aqueous corrosion environment of the bearing steel. The two main techniques used to test corrosion rate are the weight-loss method and the electrochemical polarisation test (Sagüés, 1993; Yang, 2020).

The weight-loss method includes the exposition of a tested metal specimen to a given condition for a sufficient exposure time. After which, the sample is removed from the testing medium, and the change in its weight before and after exposure is then determined (El Ibrahimi & Berdimurodov, 2023). The corrosion rate, C, is then calculated using the equation below.

$$C = kw/dAt \tag{1}$$

Where k is a constant that can be varied to get the corrosion rate in various units, w is the weight loss of the sample, d is the density, A is the exposure area and t is the exposure time.

The advantages of the method are as follows

- No sophisticated procedures or equipment are required.
- Corrosion rate obtained from direct measurement, without approximations or theoretical assumptions.
- Applicable to all testing mediums.

The disadvantages of the technique are

- Unable to monitor how the corrosion rate evolves with time.

- Period of exposure extremely long, often required acidic conditions or salt spray to speed up the corrosion. Using pure atmospheric settings (pH = 7) could take up to 5 years to get sufficient data on the corrosion rate (Díaz et al., 2018).
- Difficult to detect weight loss in specimens with high corrosion resistance.
- Results are average and sometimes not representative of the actual corrosion situation.
- Destructive in nature to the sample.

However, this technique requires selecting a testing medium that speeds up corrosion. If the test has to be done in neutral conditions, the only possibility is to use salt spray, which is undesirable due to the presence of large amounts of Cl- ions that boost pitting corrosion. Therefore, this technique will not be feasible for the experiment. The only option left will be the electrochemical polarisation method.

3.4.1 Electrochemical Polarisation Method

The electrochemical polarisation method is an electrochemical technique used to measure corrosion rates in the laboratory and monitor corrosion in the field (Papavinasam, 2021). It requires a three-electrode system containing a working electrode (testing metal), a counter electrode (platinum or graphite), a reference electrode (Ag/AgCl), and a conducting electrolyte (salt solution). Equipment needed will include a potentiostat, a potential-measuring instrument and a current-measuring instrument (Papavinasam, 2021). Figure 26 shows a schematic illustration of the electrochemical cell.

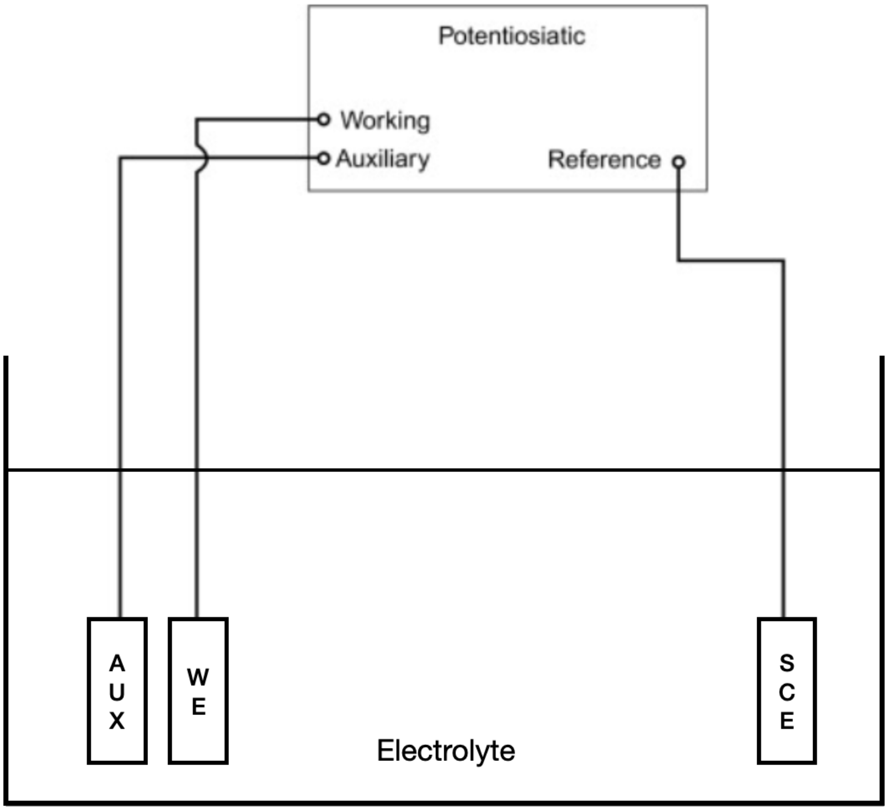

Figure 26: Schematic diagram of the electrochemical cell.

The positive sides of the technique are:

- Capable of measuring low corrosion rate.
- Short measurement duration.
- Able to monitor the corrosion rate throughout the experiment.
- The method has a well-established theoretical understanding.

The negative parts of the method are:

- Very complicated method
- Destructive in nature to the sample.
- Require a three-electrode system
- Cannot be done in an atmospheric environment; needs a testing solution.

Therefore, the requirement for the testing solution for the electrochemical polarisation test is much more lenient. The only prerequisite is that the solution conducts electricity. A very mild amount of salt will be sufficient for this requirement. Hence, the corrosion behaviour of the steel samples was studied using an electrochemical polarisation test.

3.4.2 Test Conditions

The instrument operated for the test was the VSP-300 potentiostat. A 100 ppm NaCl solution was used as the medium to create an accelerated atmospheric corrosion testing environment. For the measurements, a three-electrode system comprising a working electrode (the steel sample embedded in non-conductive resin, ground with SiC sandpapers up to a grit size of 2000, polished with 3 µm and 1 µm polishing liquid and cleaned with isopropanol in an ultrasonic bath for 10 minutes), a reference electrode (Ag/AgCl), and a counter electrode (Pt mesh) was utilised. Masking was done on the sample surface to avoid the formation of crevices during the corrosion process. During the test, a 0.071 cm^2 area of the polished steel sample was exposed to the 100 ppm NaCl solution. The results were then analysed using an EC-lab software. All the tests were repeated at least two times to ensure reproducibility.

Before the electrochemical polarisation test was conducted, a trial test confirmed the time taken for the steel sample to reach stable Open Circuit Potential (OCP). The OCP time was then set at 1 hour. The Tafel plot test was conducted at a scan rate of 0.166 mV/s and a scan range of 250 mv, more positive or more negative, with respect to OCP. From the graph obtained, the corrosion current and rate were determined by Tafel extrapolation.

Tafel extrapolation is a technique that applies a linear relationship between potential and log current that exists if the electrode is polarised to sufficiently large potentials, both in anodic and cathodic directions (Papavinasam, 2021). The result will be in the shape of a Tafel plot seen in Figure 27. The current at corrosion is then determined by the extrapolation of either anodic or cathodic or both to the corrosion potential. Finally, the corrosion rate, r, in mmpy, was calculated from the equation below.

$$r = 0.00327 * I(W/d) \tag{2}$$

Where I is the corrosion current in µA/cm^2, W is the equivalent weight of the steel and d is the density of the steel. The value of 0.00327 is due to the conversion of units.

The uncertainty of the corrosion rate was calculated using the standard deviation equation shown below.

$$\sigma = \sqrt{(\sum ri - u)^2/N} \tag{3}$$

where σ is the uncertainty of the results, ri is the corrosion rate of the i test, u is the mean corrosion rate of consistent measurement, and N is the total number of consistent measurements.

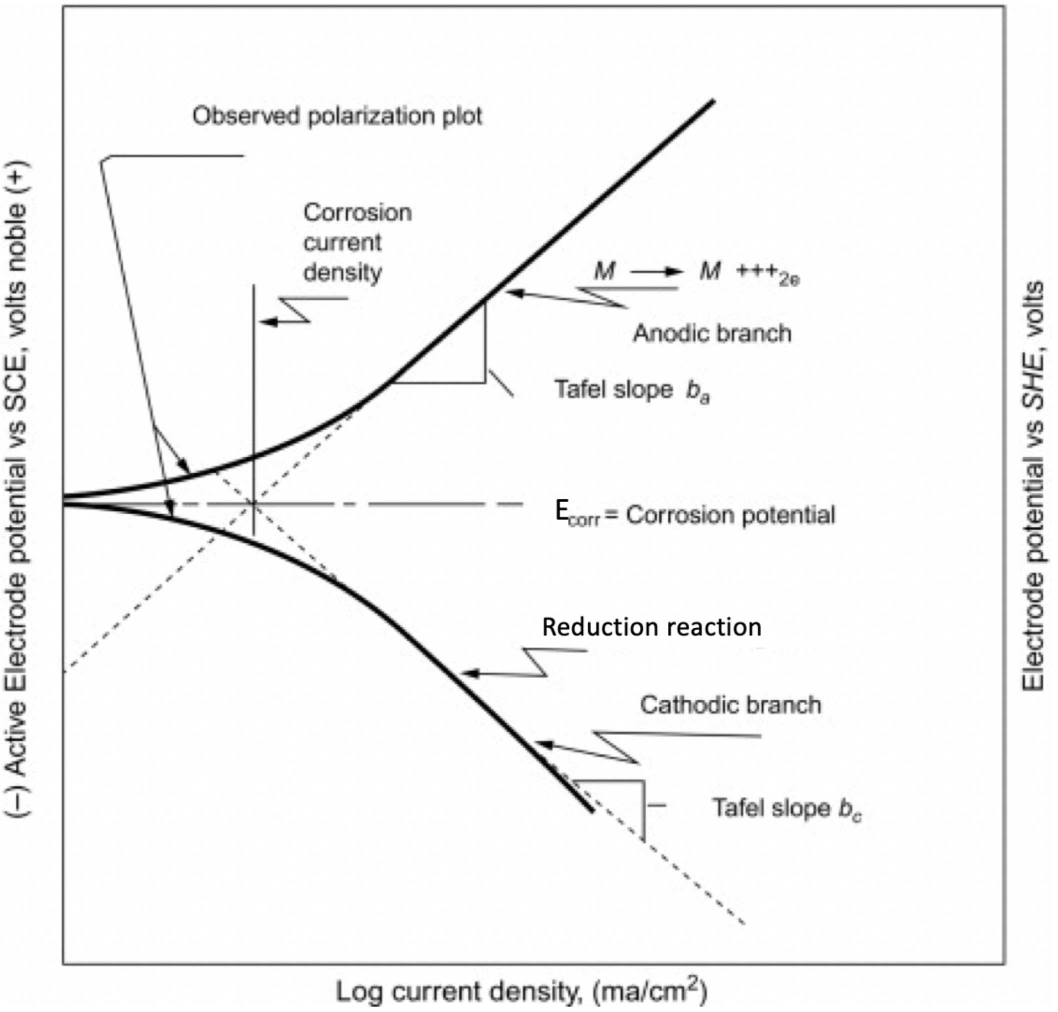

Figure 27: An example of a Tafel plot obtained using Tafel extrapolation (Papavinasam, 2021).

4 Results

This section presents the valuable findings from all the experiments conducted on the steel samples. It starts with the dilatometry curves and Tafel plot of the corrosion tests before moving to surface characterisation outcomes.

4.1 Analysis of Dilatometry Curves

Figure 28 depicts the dilatation curves, each corresponding to a representative experiment, during the heat treatment for the steels labelled TM-160, TM-240 and B (All treatments were repeated 3 times). For all the steels, a continuous increase in relative length was observed after the steels reached the stable austenitising temperature of 900 °C. From Figure 28a and b, it was noticed that the relative change in length for the steel with 0.5 wt% Cu was slightly higher than the steel without copper during the tempering process, which begins after cooling to room temperature. There were no visible changes in the shape of the change in relative length vs time curves when the tempering temperature was increased from 160 °C to 240 °C.

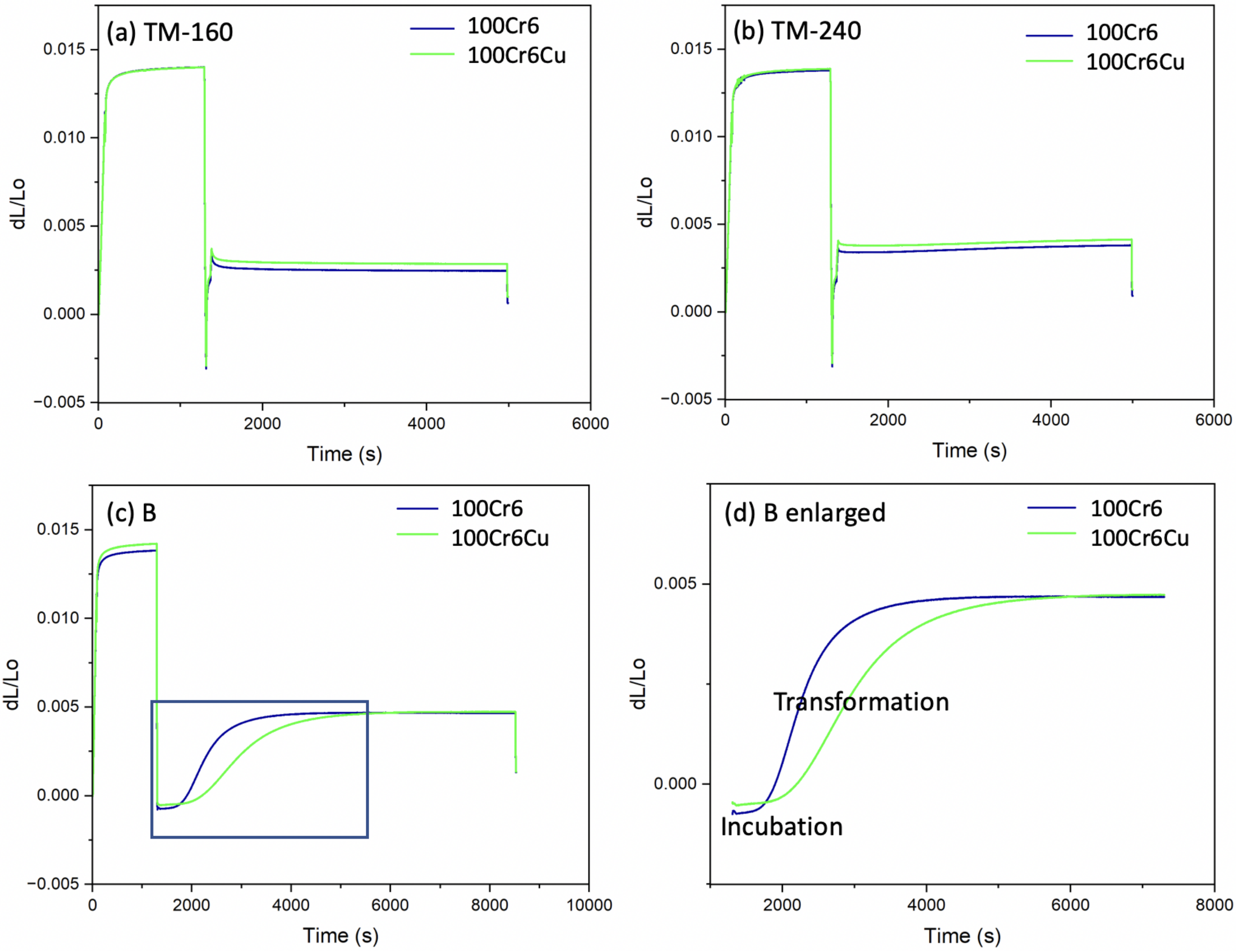

Figure 28: Dilatation curves for the formation of (a) TM-160, (b) TM-240, (c) B, (d) zoom-in image of a region for B.

During the austempering process, the steel with 0.5 wt% Cu took longer to form the bainite phase, as shown in Figure 28c. Taking a closer look at this region of the curve with Figure 28d, the incubation time (600 s > 400 s) for bainite formation was longer in the steel with 0.5 wt% Cu, and the transformation time (4400 s) of bainite was almost twice that of the steel without copper (2300 s).

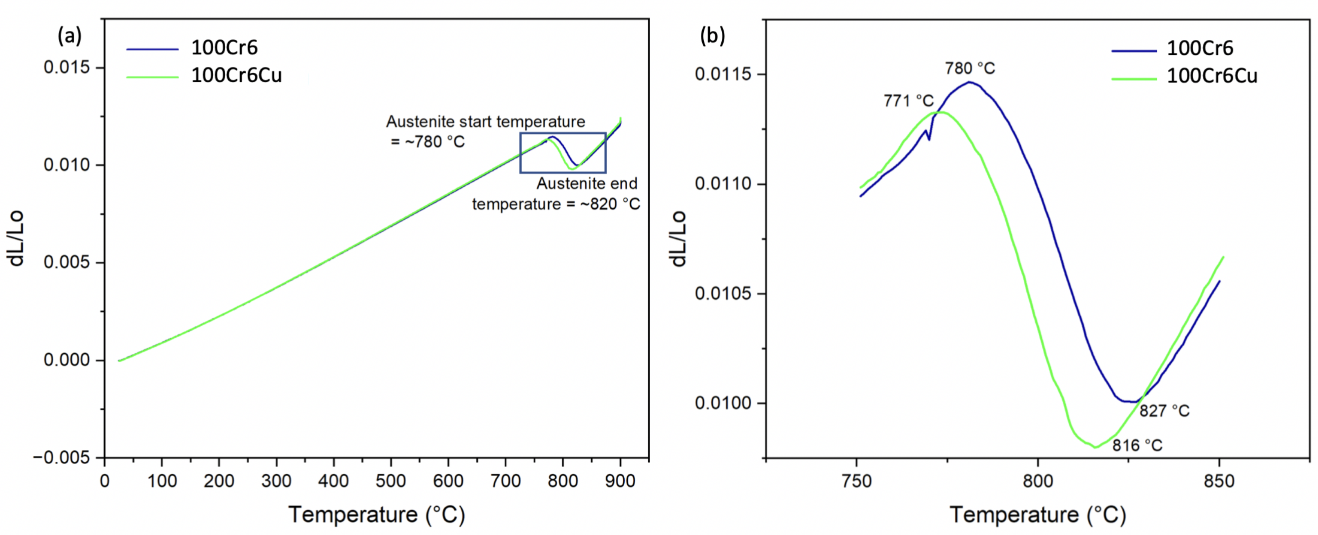

Figure 29: Change in relative length vs temperature for (a) the heating part of the heat treatment, (b) zoom-in image of the austenite phase change

Figure 29 depicts the austenite transformation during the heating process for the steel. The average austenite start temperature is around 780 °C, and the average austenite end temperature is around 820 °C. The presence of copper in the steel lowered both the steel's austenite start (771 °C < 780 °C) and end temperature (816 °C < 827 °C).

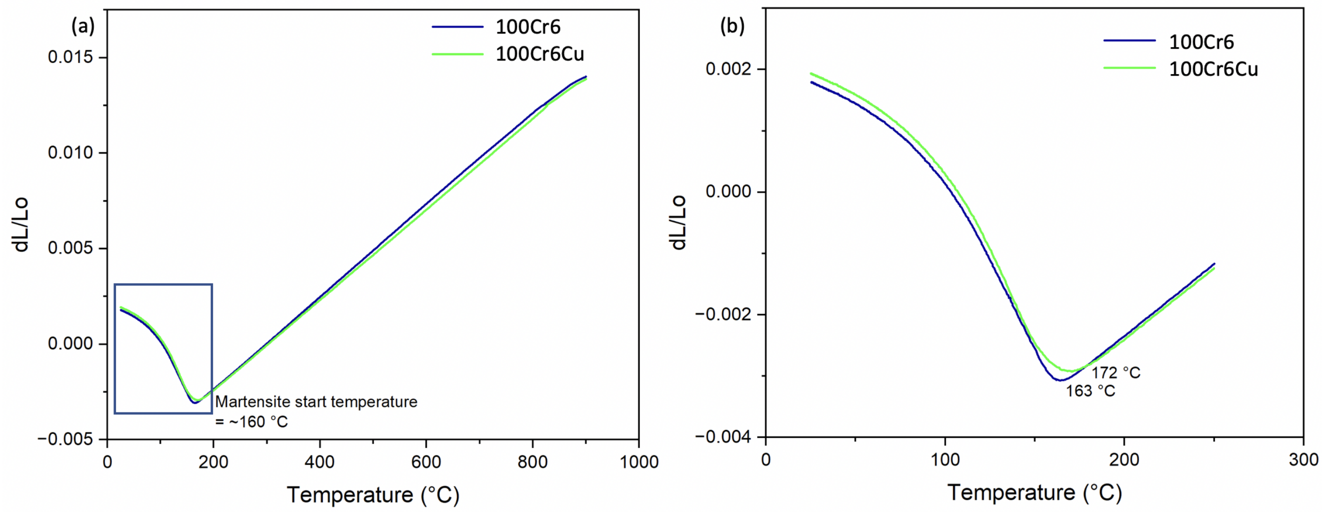

Figure 30: Change in relative length vs temperature for (a) the non-linear cooling part of the heat treatment, (b) zoom-in image of the martensite phase change

Figure 30 illustrates the change in relative length vs temperature curves for the non-linear cooling part of the heat treatment for TM-160 and TM-240. The curves for B were similar to what was observed in Figure 30, with the only difference being the curve ending at 280 °C. The average martensite start (Ms) temperature is around 160 °C, which differs enormously from the

305 °C given in the CCT diagram in Figure 24. However, the duration of the austenitisation process and degree of austenitisation were unknown for the CCT diagram. An incomplete austenite transformation could be possible for the CCT diagram, resulting in the higher Ms value.

From Figure 30b, the addition of copper to the steel increases the Ms temperature from 163 °C to 172 °C. However, this conclusion was not definite. When comparing the value from all the curves, it was realised that fluctuation in the Ms temperature was observed for the steel with copper, as shown in Table 4, with an equal number of cases of Ms temperature dropping with the addition of copper. The Ms temperature for 100Cr6 steel was relatively stable at 163 °C. Also, from the shape of the curve, the martensite phase transformation was not completed; austenite would be expected to be in the microstructure. A slight change in the slope of the curve was also observed at the start of the cooling process. This was due to the fluctuation when starting to cool.

Table 4: Ms temperature observed from the quenching of the 100Cr6Cu steel samples

Sample No.	Ms temperature (°C)
100Cr6Cu-1	172
100Cr6Cu-2	156
100Cr6Cu-3	160
100Cr6Cu-4	153
100Cr6Cu-5	170
100Cr6Cu-6	165

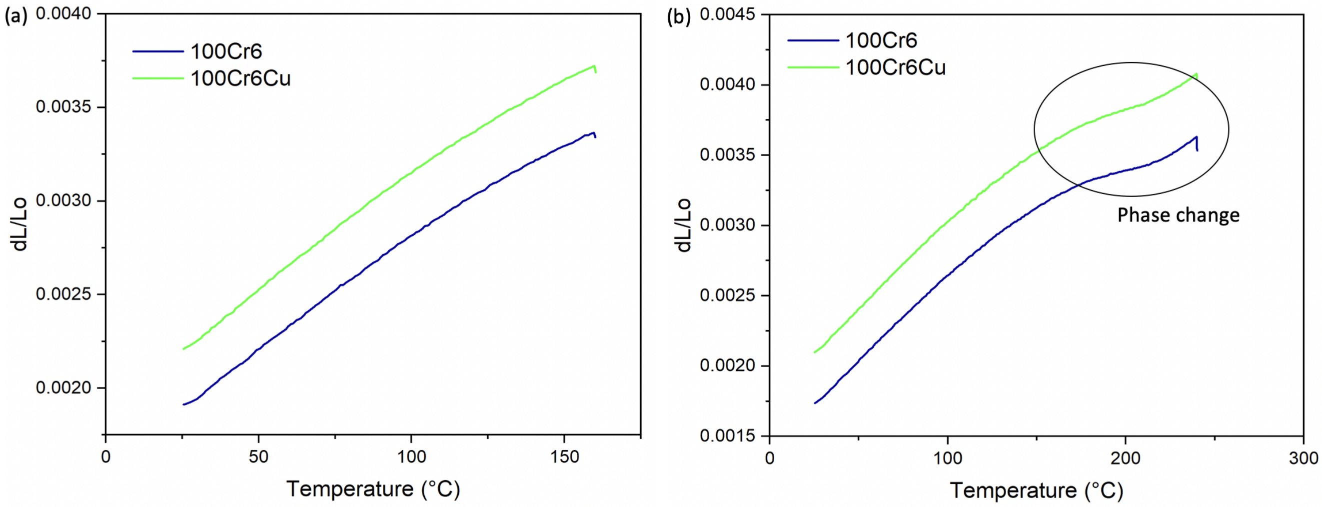

Figure 31: Change in relative length vs temperature for reheating of steel samples during the tempering process for (a) TM-160, (b) TM-240

From the change in relative length vs temperature graph during the reheating part for TM-160 and TM-240 shown in Figure 31, a phase change was observed when tempering at 240 °C (TM-240). A slight change in the slope of the curve was also recorded for TM-160 when reaching the end of the reheating process, suggesting the possibility that a phase change has already begun. For either TM-160 or TM-240, the phase transformation was not complete.

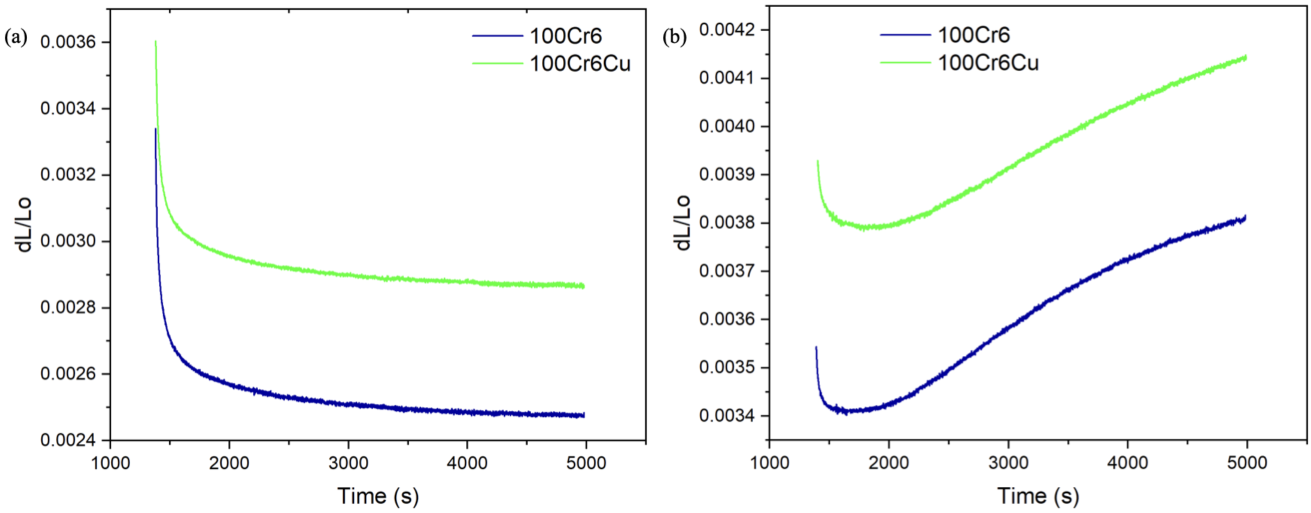

Figure 32: Change in relative length vs time for the tempering of steel samples for (a) TM-160, (b) TM-240

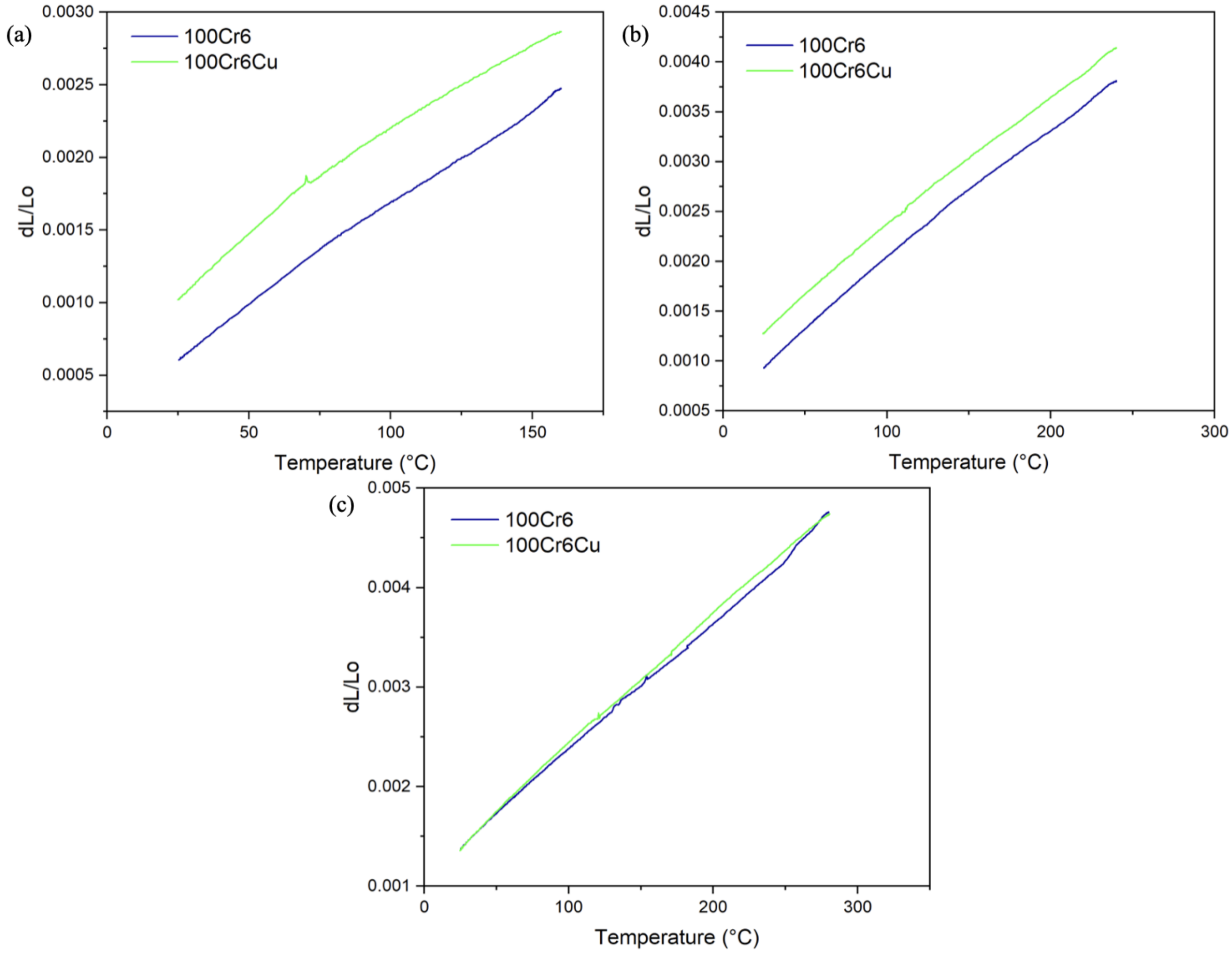

Figure 33: Change in relative length vs temperature for the final cooling of steel samples for (a) TM-160, (b) TM-240 and (c) B

Figure 32 gives the change in relative length vs time graph for the tempering process of the steel. For both TM-160 and TM-240, a sharp decrease in the relative change in length was observed at the initial stage of the process. Tempering at 160 °C results in a reduction of relative length, while tempering at 240 °C shows an increase in relative length. For both graphs, no changes in the shape of the curve were observed when copper was added to the steel.

No visible phase change was found in the final cooling stage of the heat treatment, as shown in Figure 33.

4.2 Characterisation of Steel Surface

The microstructures and phases of the steel after heat treatment were analysed using LOM, SEM and EDS. Figure 34 gives the LOM images of the steels at X2500 magnification. Figure 34 a, b, d, e shows typical martensite phases, with the alternating plate-like part relating to plate martensite. In addition, the grain size of the martensite phase in TM-240 was coarser than that of the TM-160. Figure 34 c, f gives typical bainite phases, with bainite sheaves seen in many parts of the image. For all the steels, it was also noticed that the microstructure became coarser from a to c and from d to f. The black spots in Figure 34a were from some contamination source.

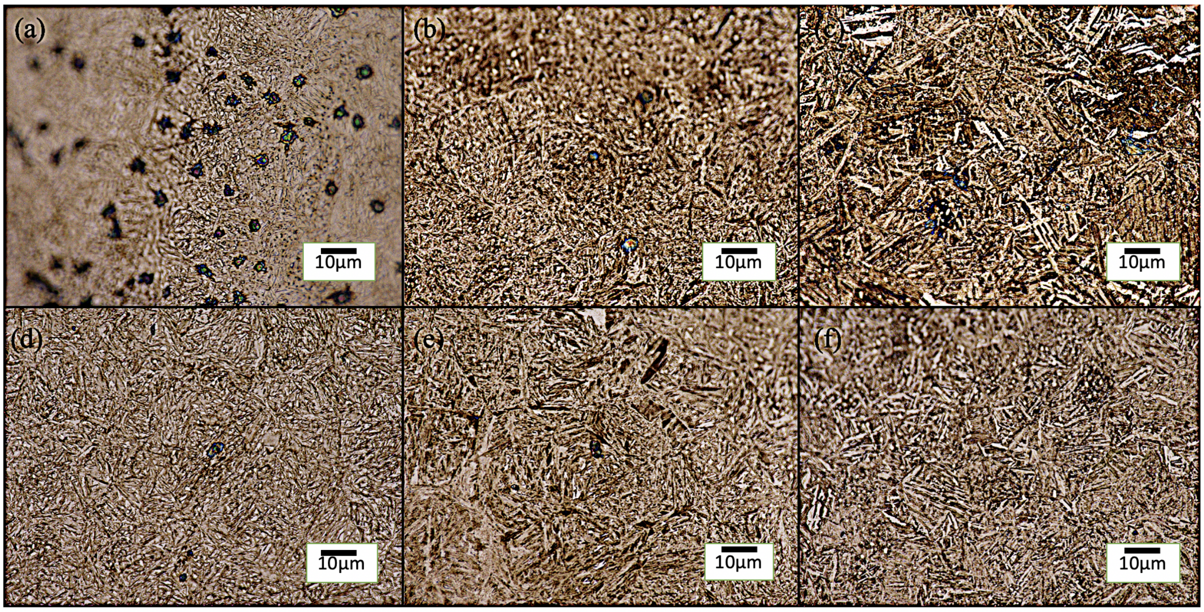

Figure 34: LOM images at X2500 of the uncorroded steel without and with 0.5wt% Cu respectively. TM-160 (a, d), TM-240 (b, e), B (c, f)

Figure 35 depicts the SEM images of the steels at X5000 magnification. The typical microstructure of martensite and bainite can be seen in the respective steel samples. The overall observation was very similar to the photos from LOM in Figure 34. Comparing Figure 35c and f, the bainite microstructure for the steel with 0.5 wt% Cu differed from that for the steel without copper, with the latter showing a more distinctive bainite sheaves with a larger grain size.

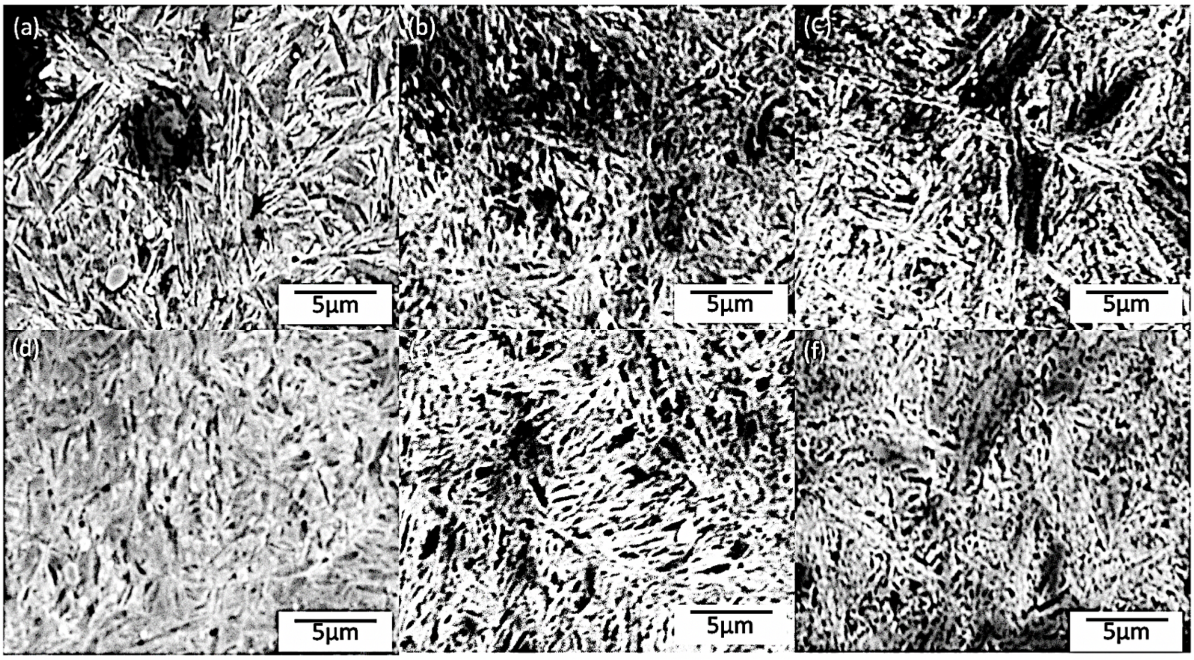

Figure 35: SEM images at X5000 of the uncorroded steel without and with 0.5wt% Cu respectively. TM-160 (a, d), TM-240 (b, e), B (c, f)

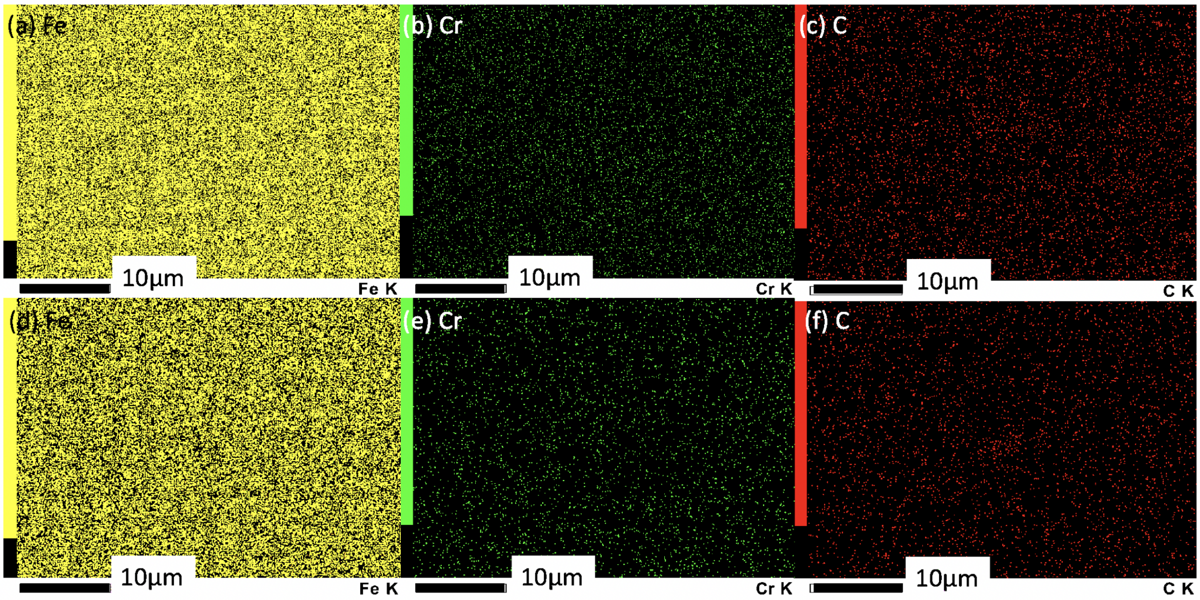

Figure 36: EDS pattern at X3000 of the uncorroded steel with bainite phase. Without Cu (a, b, c), with 0.5 wt% Cu (d, e, f)

The results from the EDS analysis of the surface were very similar for every steel. Using the B steel texture at X3000 as an example, the EDS pattern, as seen in Figure 36, shows that only three elements were distributed evenly on the surface of the steel, namely Fe, C and Cr. Cu was not detected for the B steel with copper, suggesting that either the concentration of Cu on the surface is too low or there is no Cu available in the range of the penetration depth of EDS, given that the detection limit of EDS for bulk material is at 0.1 wt%. This result is consistent for the TM-160 and TM-240 steel.

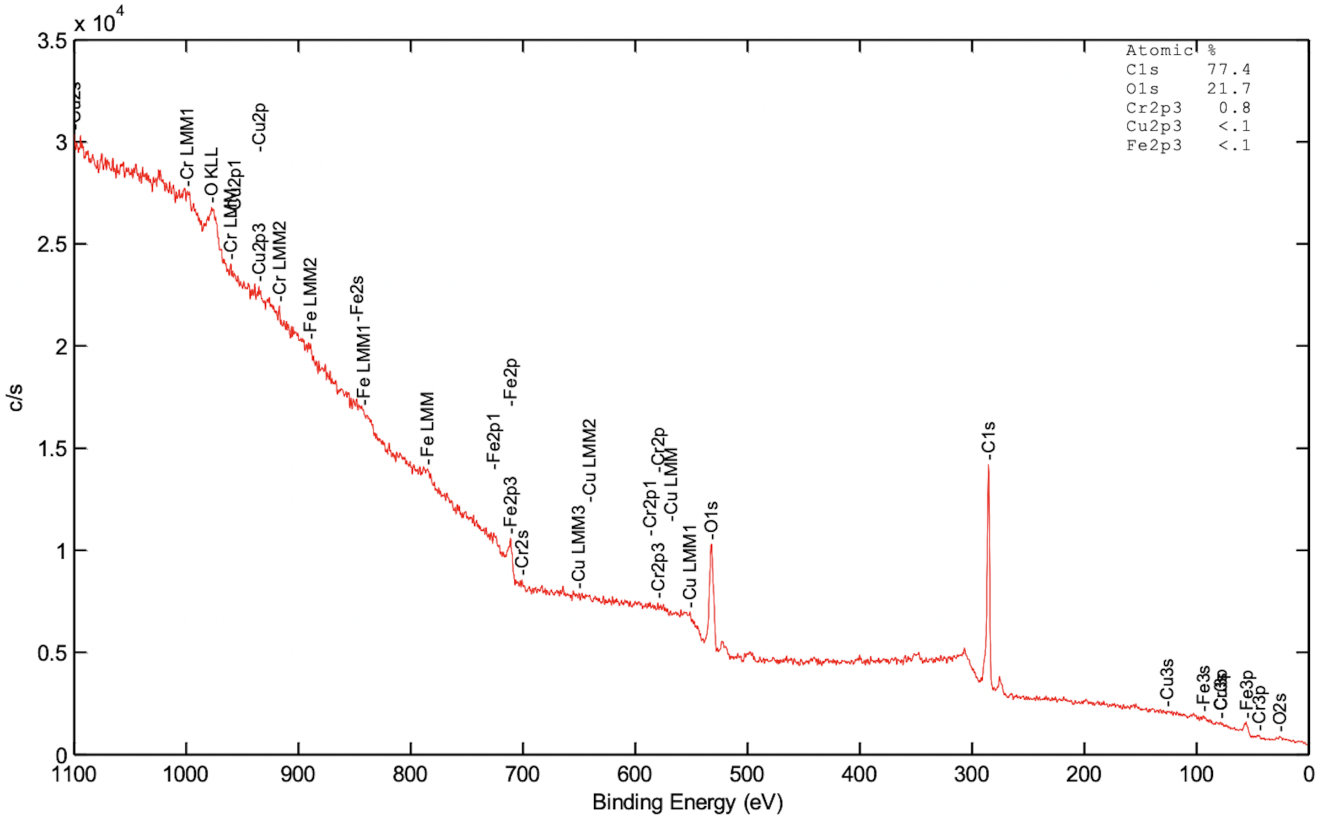

Figure 37: XPS spectrum of the B steel with 0.5 wt% Cu before corrosion

Figure 37 depicts the general XPS spectrum of the B steel with 0.5 wt% Cu before corrosion. Peaks were seen in the general spectrum if the machine detected the element on the top 1 to 10 nm surface. From the general spectrum, the surface was covered by a thin layer of adventitious carbon and oxygen. Fe and Cr were also detected on the surface, with the individual spectra of Fe and Cr showing distinctive peaks. However, the spectra of Cu showed only noise and no unique peaks of Cu were found. Given that the detection limit of XPS is at 0.1 at%, which is way lower than the amount of copper present in the steel (0.5 wt%), it can be derived that Cu was not present on the steel surface initially. This finding was consistent with the results from the EDS analysis in Figure 36.

4.3 Results of Corrosion Tests

Two different electrochemical corrosion tests were conducted on the steel, one with masking and the other without. In the test result without masking, crevice corrosion was observed at the interface between the non-conductive resin and the side of the steel. This made the results uncontrollable and, therefore, unreliable. The full results for the test without masking can be found in Appendix B. The corrosion results from the test with masking applied are presented below.

Table 5: Average corrosion results of the bearing steel with masking

Steel	Eocp (mV)	Ecorr (mV)	icorr (µA/cm^2)	Corrosion rate (mmpy)
100Cr6 (TM-160)	-313.8	-306.3	2.55	0.0298 ± 0.0020
100Cr6Cu (TM-160)	-299.6	-284.5	2.09	0.0245 ± 0.0010
100Cr6 (TM-240)	-247.8	-203.4	0.75	0.0088 ± 0.0001
100Cr6Cu (TM-240)	-269.2	-221.8	0.71	0.0083 ± 0.0017
100Cr6 (B)	-315.5	-320.0	2.57	0.0301 ± 0.0011
100Cr6Cu (B)	-287.6	-266.6	2.35	0.0275 ± 0.0009

Table 5 gives the mean corrosion results of the bearing steel with masking. The OCP value of the reaction was retrieved from the test's OCP curve. Tafel extrapolation was done to obtain the Ecorr and Icorr values. The corrosion rate and uncertainty were calculated using equation 2 and equation 3 respectively, by assuming iron was oxidised to Fe^{2+}, using the density of the 100Cr6 bearing steel (7.81 Kg/dm^3), the molar weight of 100Cr6 bearing steel (55.349 g/mol), a exposed surface area of 0.071 cm^2, and only taking the results of consistent measurements.

From Table 5, the below conclusions were derived.

- Adding copper to the bearing steel improved the corrosion resistance of the steel, with TM-160 yielding the best resistance against corrosion.
- TM-240 has the lowest corrosion rate, while the corrosion rates of TM-160 and B were similar. This outcome was in line with the conclusion drawn from the literature review, with cementite in bainite (B) and retained austenite in less-tempered martensite (TM-160) boosting the corrosion of the steel due to the galvanic effect. The lower percentage of retained austenite in tempered martensite (TM-240) will, therefore, lead to a weaker corrosion rate of the phase.
- Adding Cu to bainite (B) was also less effective against corrosion than adding Cu to the less-tempered martensite phase (TM-160), as shown by the percentage decrease of the corrosion rate of TM-160 and B when copper was added.
- The effect of copper on the corrosion of the tempered martensite phase was minimal.

Figure 38 compares the Tafel plot between steels with masking with 0.5 wt% Cu and without Cu for TM-160, TM-240 and B. The conclusions from the Tafel plot are listed below.

- The results were repeatable and reliable, with the exception of TM-240. However, although the curves for TM-240 were 'jumpy', the results were not significantly different from other repetitions. The unstable readings could be due to contact problems, the presence of bubbles near the sample or reference electrode, leakage of the solution, etc.
- Overall, the reduction curve of the Tafel plot was smooth, with no steep slopes observed. This meant there was no evidence of oxygen limiting the reduction reaction.
- In general, all curves show active behaviour without the presence of a passivity region

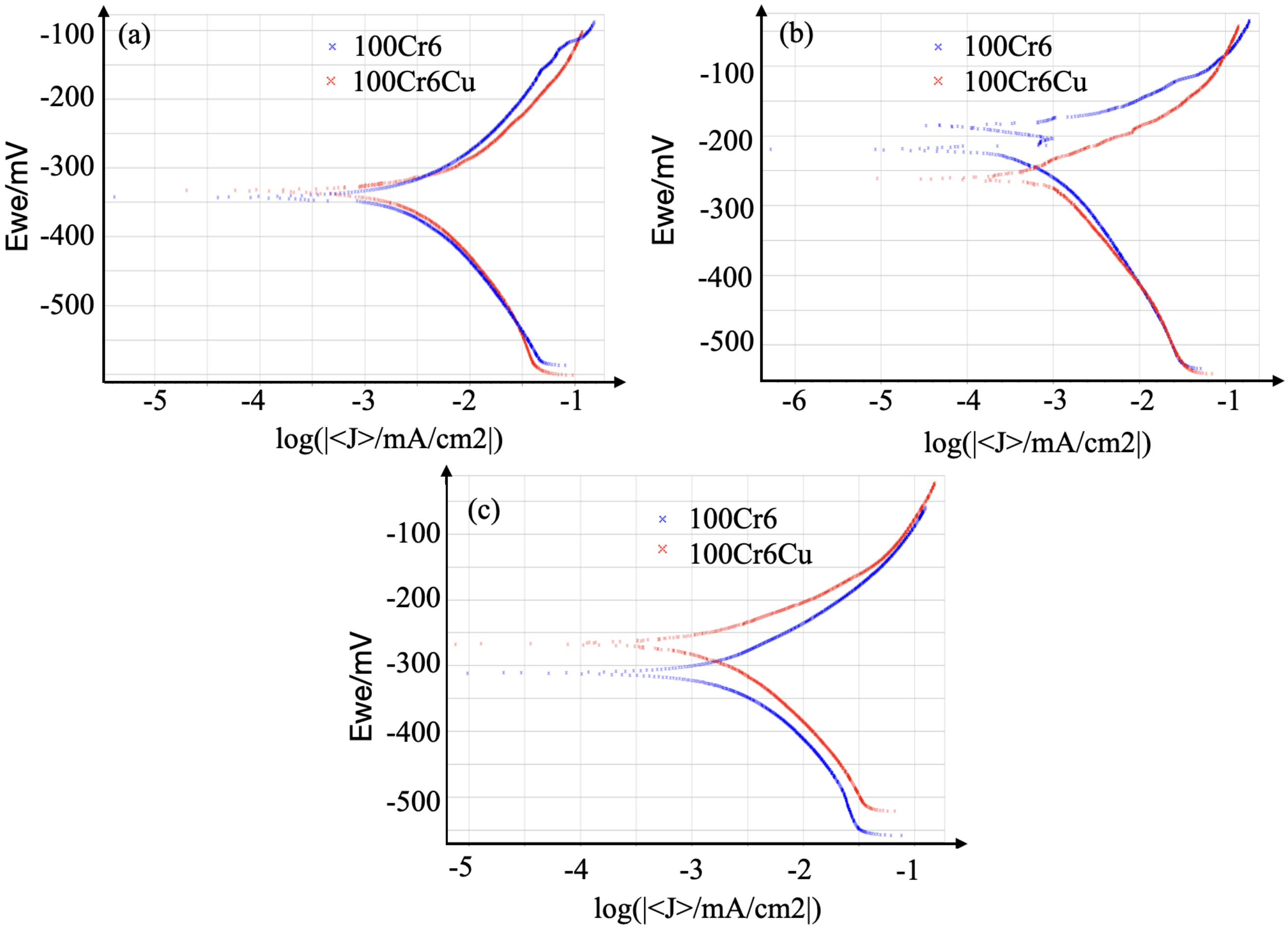

Figure 38: Tafel plot of the bearing steel with masking, (a) is for TM-160, (b) is for TM-240 and (c) is for B

The detailed result for the corrosion test with masking can be found in Appendix A

4.4 Characterisation of Corroded Steel Surface

XRD, LOM, SEM, EDS, and XPS were used to closely examine the steel surfaces after corrosion. The results are as follows.

4.4.1 XRD Patterns

Figure 39 illustrates the overall XRD pattern of the corroded steel samples. The coloured lines represent the 2θ value where the associated phases were present. The overall shape of the XRD patterns was as expected, with retained austenite found in both TM-160 and TM-240 and cementite found in B. The fraction of the retained austenite was calculated using Rietveld fitting, and the results were given in Table 6. Cementite was considered in the refinement, while possible phases from the oxides were excluded. The error given by the software was in the order of 0.001, but the actual error was probably more prominent due to the overlapping peaks between FCC austenite and BBC ferrite. Therefore, the uncertainty of the results is assumed to be around 0.01.

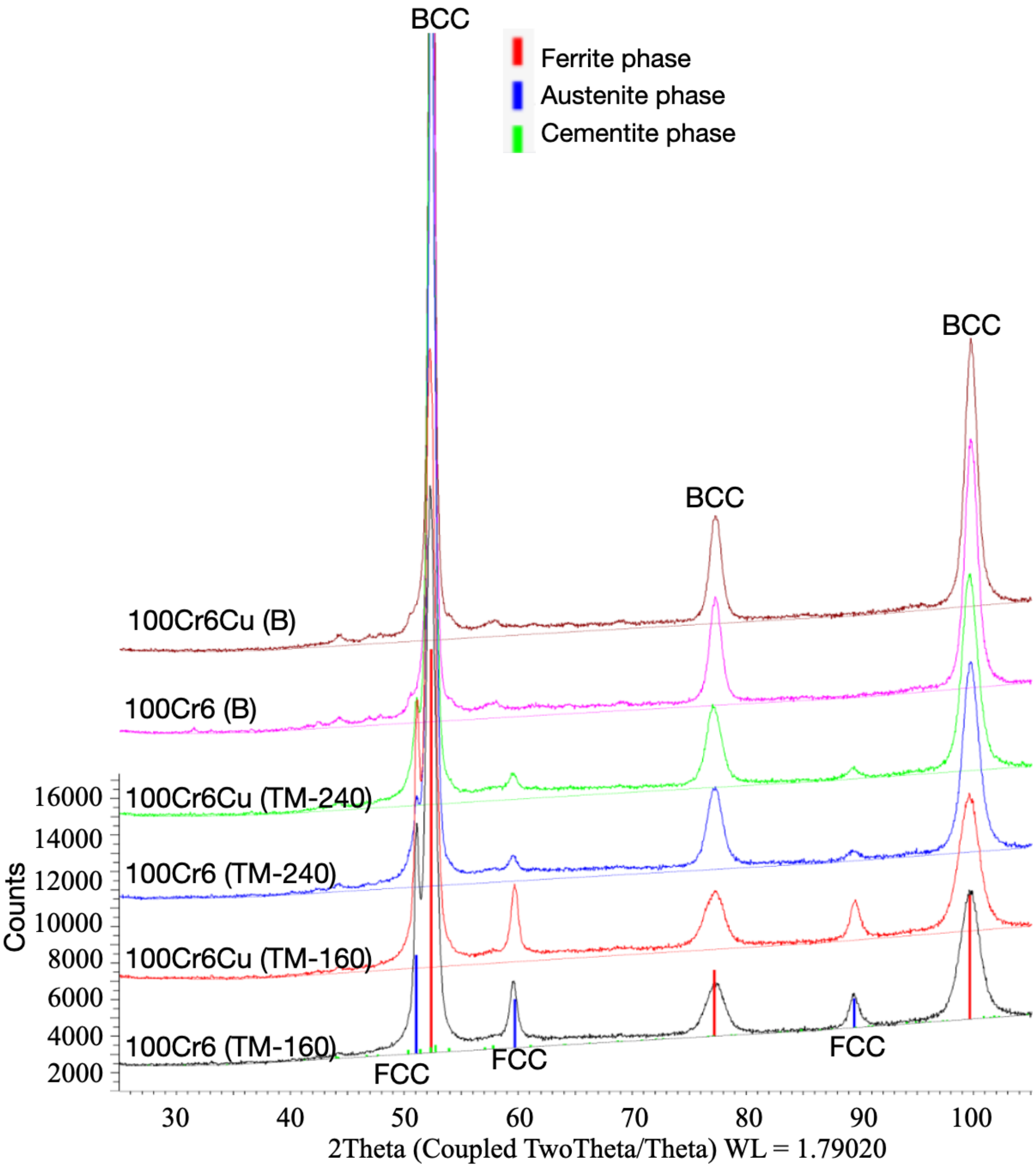

Figure 39: The overall XRD patterns of the bearing steel.

From Table 6, the fraction of retained austenite in TM-160 (0.19) was much higher than that in TM-240 (0.08), while very little austenite was detected from B. Also, a higher fraction of retained austenite was seen in the steel with copper than that without for TM-160. In addition, judging from the peak height of austenite and cementite peaks shown in Figure 39, the amount of austenite in TM-240 with copper and the amount of cementite in B with copper was also higher.

Small peaks at 2θ between 40 and 46 deg were also seen from Figure 39. These peaks were not in the location of the 2θ value for ferrite, austenite or cementite. As corroded surfaces were used for the XRD scan, it was predicted that these should be peaks from the corrosion products. The portion of the XRD pattern was enlarged for a more detailed analysis.

Table 6: Fraction of retained austenite in the bearing steel after heat treatment, calculated using Rietveld fitting

Steel	Fraction of retained austenite
100Cr6 (TM-160)	0.19 ± 0.01
100Cr6Cu (TM-160)	0.20 ± 0.01
100Cr6 (TM-240)	0.08 ± 0.01
100Cr6Cu (TM-240)	0.08 ± 0.01
100Cr6 (B)	0.01 ± 0.01
100Cr6Cu (B)	0.01 ± 0.01

Figure 40 gives a closer look into the small peaks (2θ = 40 to 45 deg) in the XRD pattern of the TM-160 steel, which most likely belongs to cementite for the steel with no copper. Peaks belonging to oxides were not found for the steel without copper despite the fact that the steel has undergone corrosion. One extra peak was discovered at $2\theta =$ 42 deg for the steel with 0.5 wt% Cu, and it could belong to two different possibilities: FeO or Cu_2O. However, no other visible peaks were there to distinguish between the two candidates. In addition, chromium oxide was not found in either steel sample.

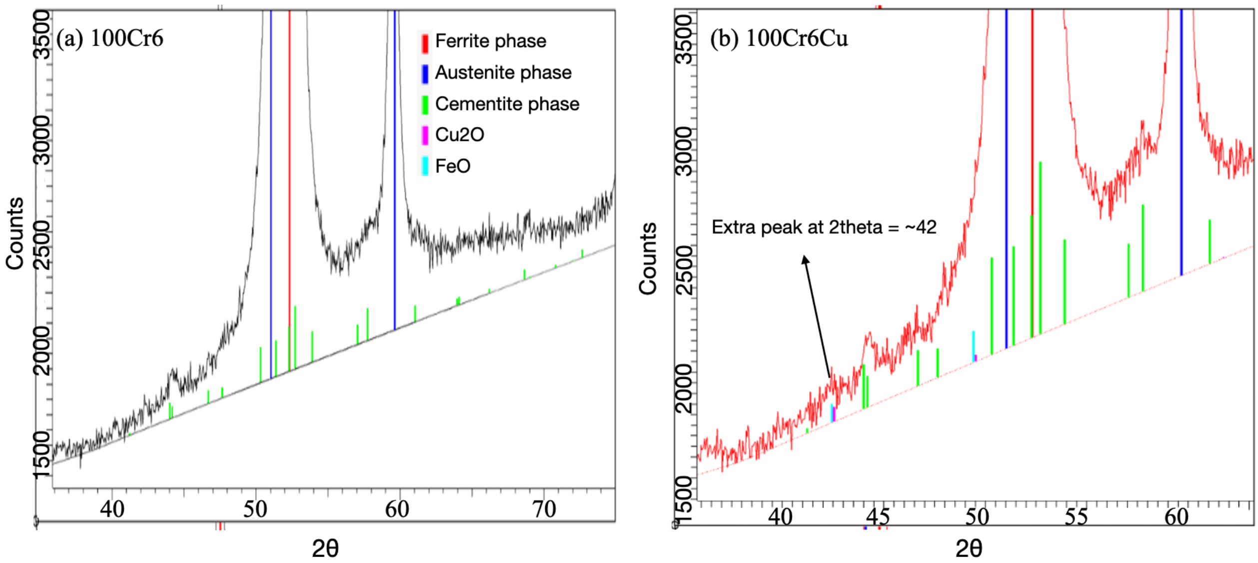

Figure 40: The zoom-in XRD pattern of the TM-160 steel, (a) for without Cu and (b) for with 0.5 wt% Cu

Small peaks at $2\theta =$ 44 deg from cementite were found for the XRD pattern of TM-240 steel without Cu, as depicted in Figure 41. An additional peak at $2\theta =$ 42 deg, most likely belonging to FeO, was also noticed. Cu_2O was another candidate for that peak, but this sample contains no Cu. No difference in the XRD pattern was observed for the sample with 0.5 wt% Cu. However, given the presence of copper in the steel, the same issue as with the peak at $2\theta =$ 42 deg for TM-160 occurred. Likewise, peaks belonging to chromium oxide were not discovered in the XRD pattern.

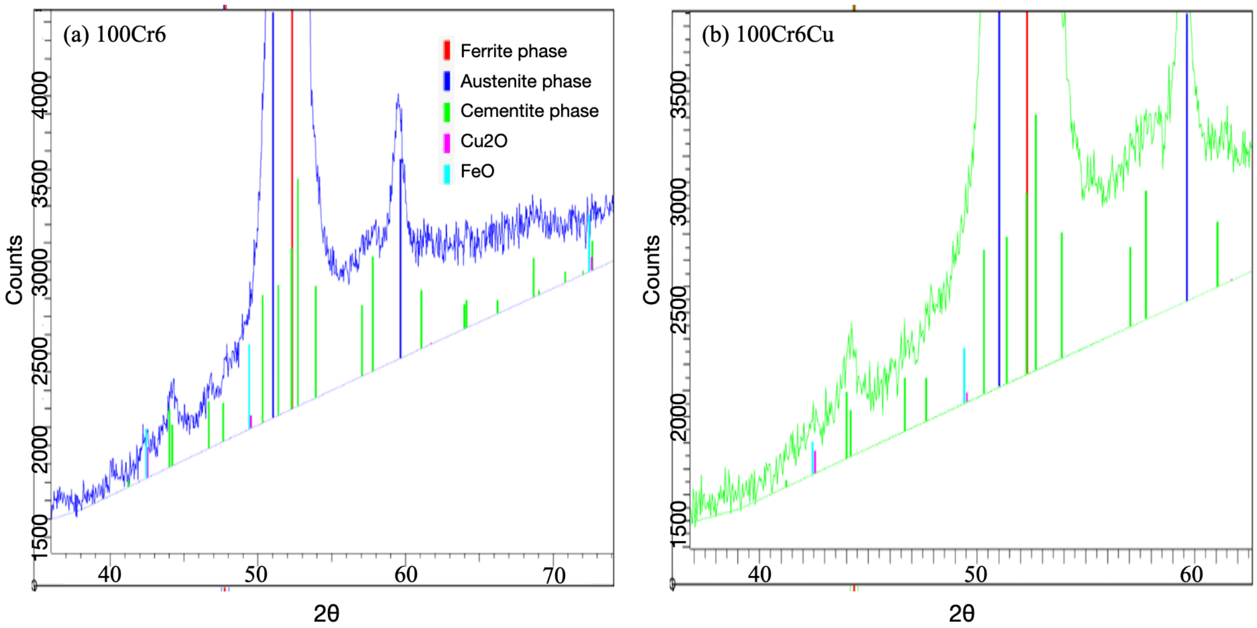

Figure 41: The zoom-in XRD pattern of the TM-240 steel, (a) for without Cu and (b) for with 0.5 wt% Cu

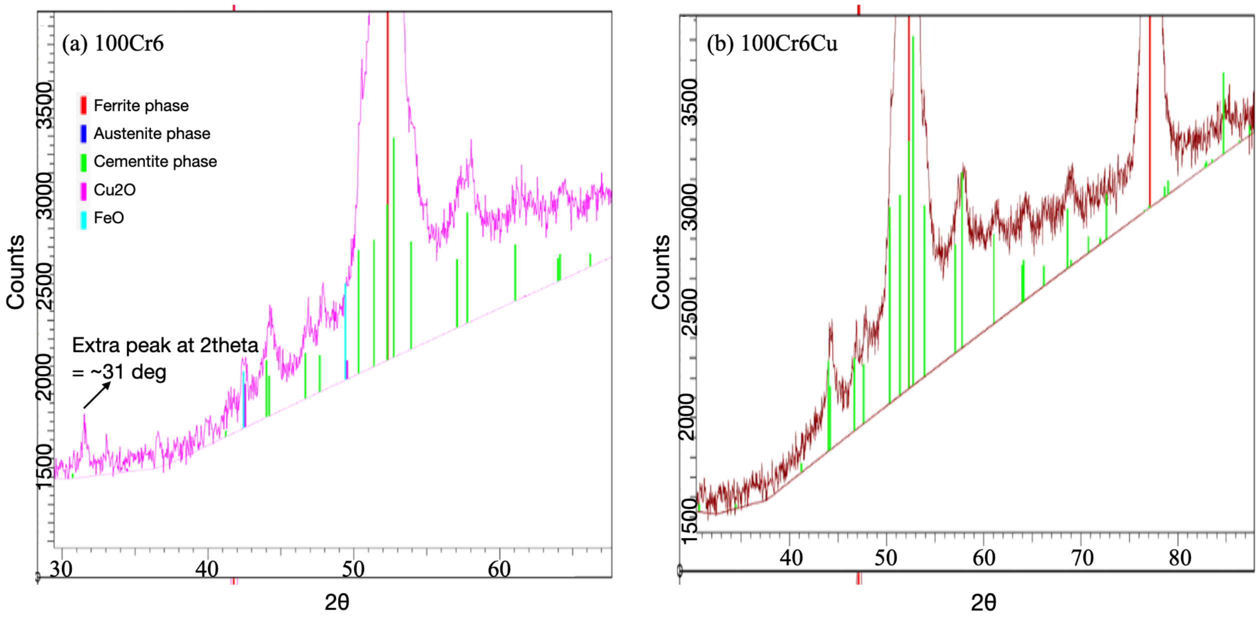

Figure 42: The zoom-in XRD pattern of the B steel, (a) for without Cu and (b) for with 0.5 wt% Cu

From the zoom-in image of the XRD pattern for B steel without Cu, as seen in Figure 42, a peak at $2\theta =$ 42 deg belonging to FeO was found. Another peak at $2\theta =$ 31 deg could be from Fe_2O_3, but it was hard to confirm the existence of Fe_2O_3 with the single peak, while other peaks from the database were missing in the XRD pattern. The XRD pattern of the B steel with 0.5 wt% Cu exhibits mainly ferrite and cementite peaks. A small peak at $2\theta =$ 42 deg belonging to two possible candidates was also available. No other oxides were detected by the XRD detector. This could be the result of the XRD's deep penetration depth, given that the oxide layer's thickness was believed to be only around 2 µm. In addition, the inability to distinguish between overlapping peaks has created a lot of trouble during the analysis of the

XRD pattern.

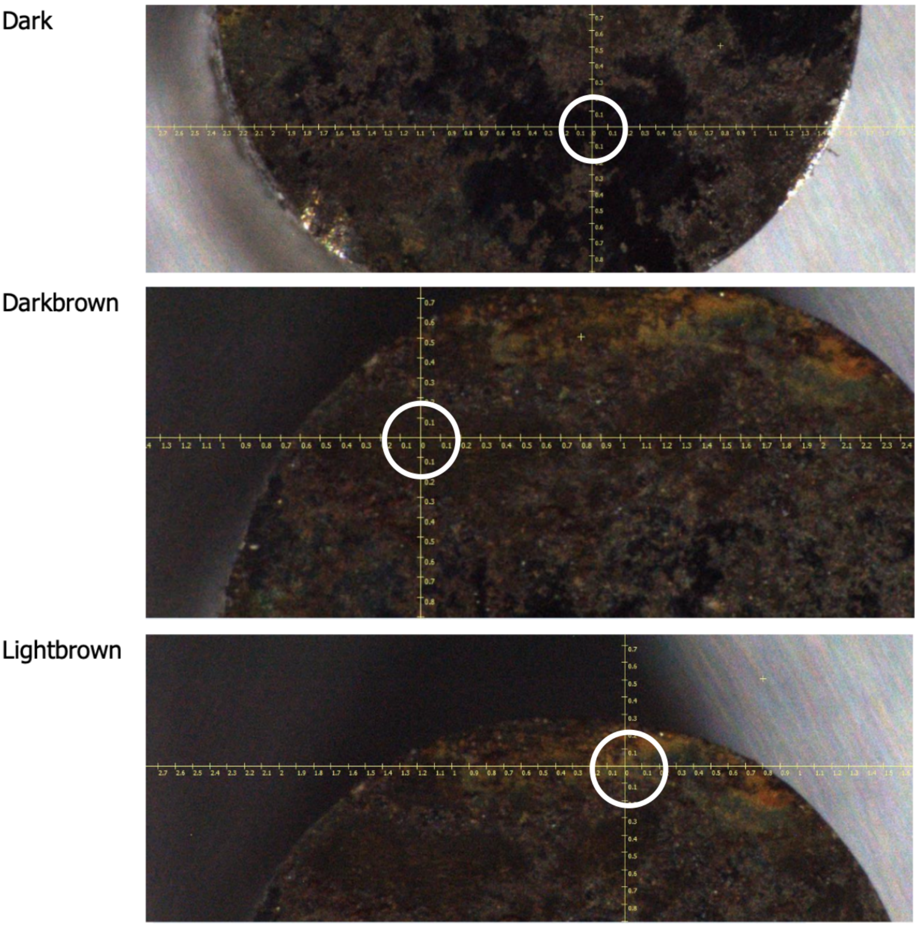

Figure 43: The three points on the corroded surface of the B steel with 0.5 wt% Cu that will be examined under an XRD with a smaller beam size. The names of it are dark, dark-brown and light-brown, respectively

To reduce the penetration depth and to better characterise the steel surface, a 2D XRD machine with a smaller beam size (0.2*0.2 mm), Cu Ka source, and refined acceleration voltage and current was used on three points of the corroded surface, as shown in Figure 43. The dark point represents the bainitic matrix, the dark-brown point is associated with an oxide layer, and the light-brown point is a region of severe corrosion. The white circle denoted the total surface scanned by the 2D XRD machine.

The 2D XRD pattern of the three points on the corroded surface of the bainite steel with 0.5 wt% Cu is given in Figure 44. The maximum intensity line corresponds to the BCC ferrite phase. High-intensity regions (light-red rectangles/lines in black boxes) belonging to cementite can be found in all three 2D XRD patterns. In addition, more areas with high intensity can be seen for the dark-brown and light-brown parts of the steel surface. The continuous light band of the 2D XRD pattern also suggest that the grain size of the phases is very small (< 10 µm). The XRD pattern was more closely examined by converting it from 2D into 1D.

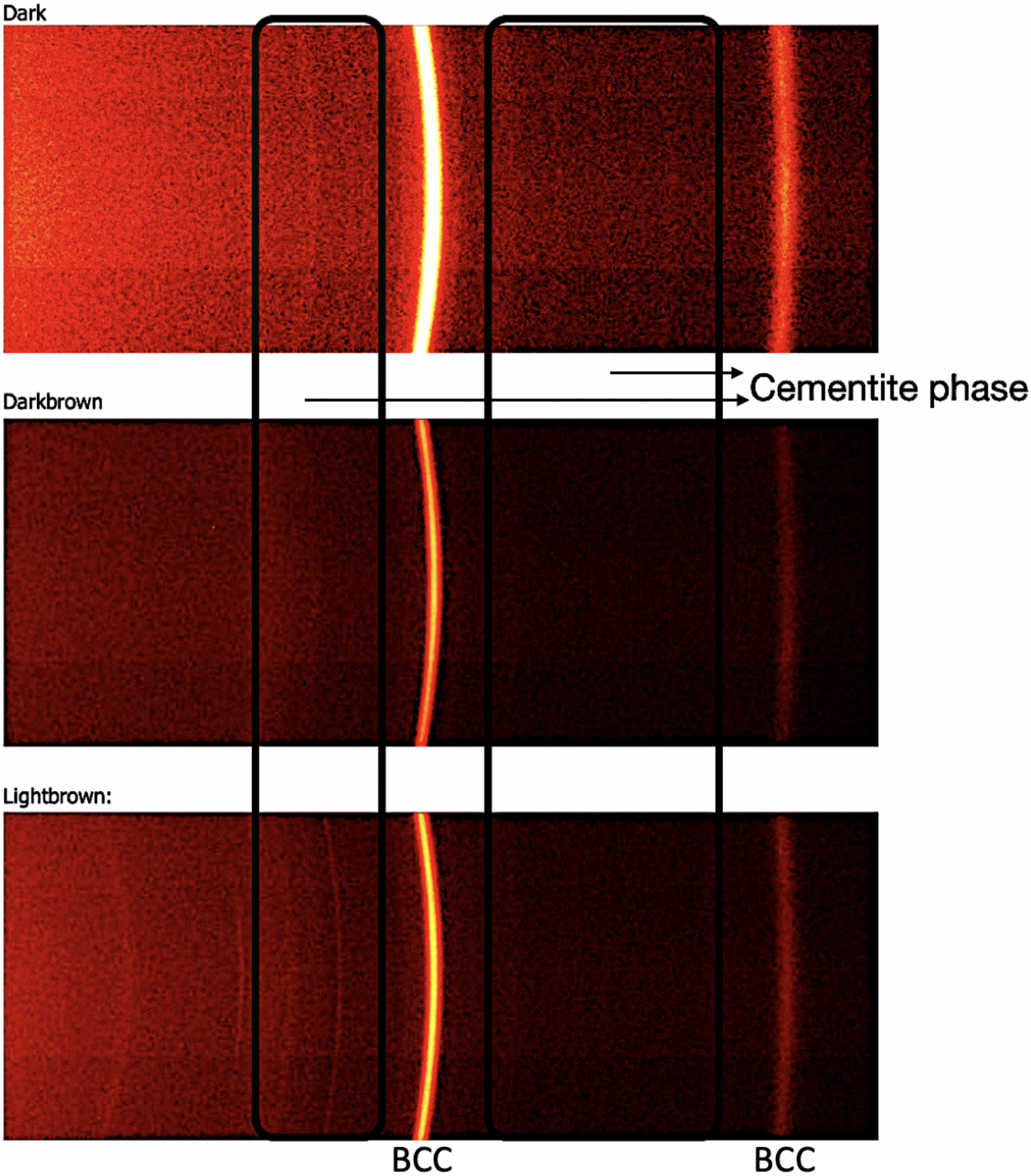

Figure 44: 2D XRD pattern of the three points on the corroded surface of the bainite steel with 0.5 wt% Cu.

Figure 45 gives a closer look at the 1D XRD pattern of the corroded surface of the B steel with 0.5wt% Cu. For the dark part shown in Figure 45a, no peaks belonging to oxides were discovered from the pattern. This finding correlates with the hypothesis that this region of the steel was not rusted, as observed from the LOM images shown in Chapter 4.4.2.

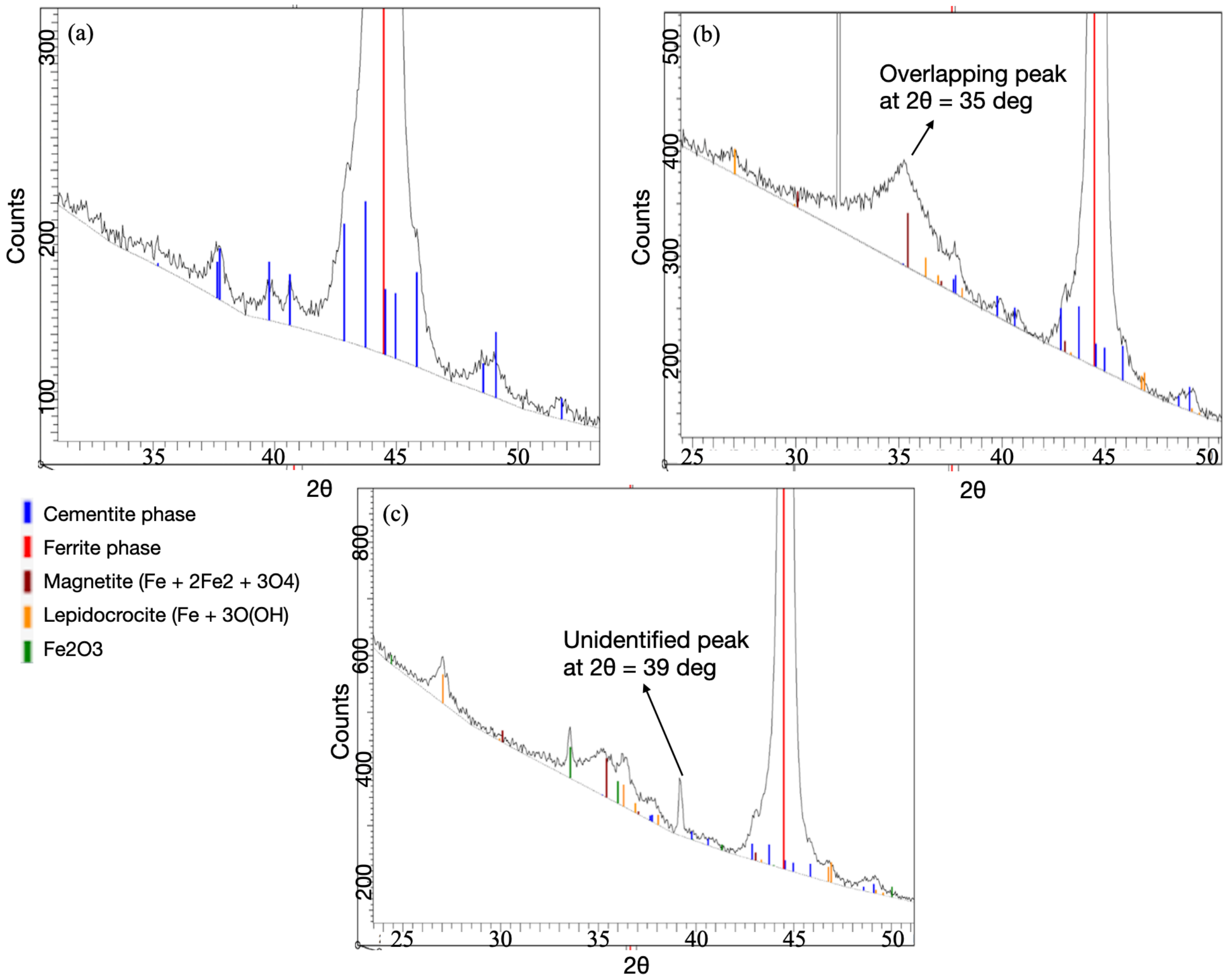

Figure 45: Zoom-in 1D XRD pattern of the corroded surface of the B steel with 0.5 wt% Cu, (a) for the dark part, (b) for the dark-brown part and (c) for the light brown part

Extra broad overlapping peaks at $2\theta =$ 35 deg can be observed from the zoom-in 1D XRD pattern at the dark-brown part of the corroded surface of the B steel with 0.5wt% Cu in Figure 45b. The possible phases were identified as magnetite and lepidocrocite, two types of iron oxide/iron hydroxide. The empirical formula of magnetite is Fe_3O_4, while the empirical formula of lepidocrocite is FeO(OH), two common corrosion products expected in corroded steel samples. The sharp spike at $2\theta = 31$ deg came from some high-intensity pixels on the detector, possibly from a cosmic ray. FeO and Cu_2O could also be on the surface, as the broad peak is believed to be the result of multiple peaks overlapping with each other. However, a better technique would be required to confirm the existence of FeO and Cu_2O. A specific search was also done for Cr2O3 and Cr2O5 but yielded no results, despite test results from past experiments suggesting that Cr_2O_3/Cr_2O_5 might also be possible (Lupu et al., 2024).

The enlarged 1D XRD pattern of the light-brown part of the corroded B steel surface, as shown in Figure 45c, seems to be the combination of the first 2 XRD patterns, with some new peaks also seen. Fe_2O_3 was identified, together with Magnetite and Lepidocrocite. FeO and Cu_2O were possible, but another surface analysis technique would be required to confirm its presence. One sharp peak at $2\theta =$ 39 deg cannot be identified. It fit well with $CuFe_2O_4$ from the database, but the lattice parameter was very different from similar entries, so it was unreliable.

In conclusion, the XRD results corresponded well with the expected phases of the TM-160, TM-240, and B steel. Possible oxides such as FeO, Cu_2O, Fe_2O_3, and FeOOH were detected. However, the overlapping peaks in the XRD pattern created many difficulties during the identification of the corrosion products, resulting in uncertainty with the oxides found. In addition, the deep penetration depth of the technique could result in many possible oxides on the surface that the machine cannot detect. For example, chromium oxide was expected to be present, but no candidates from the database were found despite a specific search for Cr_2O_3 being done on the XRD pattern. The whole table showing the oxides found with each XRD technique and XPS can be found in Table 7 in Chapter 4.4.4

4.4.2 LOM Images

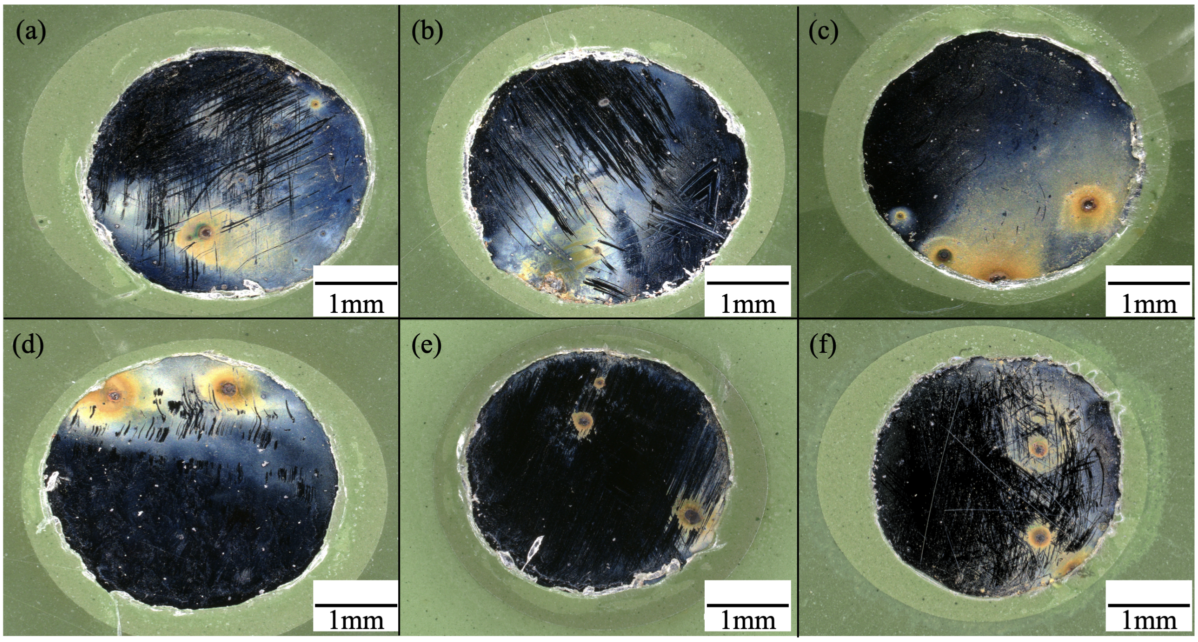

Figure 46: LOM images at X50 of the corroded steel with masking without and with 0.5 wt% Cu respectively. TM-160 (a,d), TM-240 (b,e), B (c,f)

Pitting corrosion can be seen from the LOM images of the corroded steel surface with masking at X50 magnification, as shown in Figure 46. Evidence of possible uniform corrosion can also be found in the TM-160, TM-240 and B steel given in Figure 46a, b, c, f. However, more examination was needed to determine whether there was uniform corrosion or just corrosion products from pitting corrosion spreading to further locations. The magnitude of corrosion on the surface of the steel correlates with the corrosion results obtained in Chapter 4.3, with the TM-240 showing very little corrosion evidence. There were always regions on the surface that were not rusted for all the samples. In addition, masking the sample surface successfully avoided corrosion at the side of the steel surface or crevice corrosion at the interface between the non-conductive resin and the steel. Also, the pits on B steel without Cu were the largest by size compared to the other pits that formed in TM-160 steel, TM-240 steel or B steel with 0.5 wt% Cu.

4.4.3 SEM and EDS Images

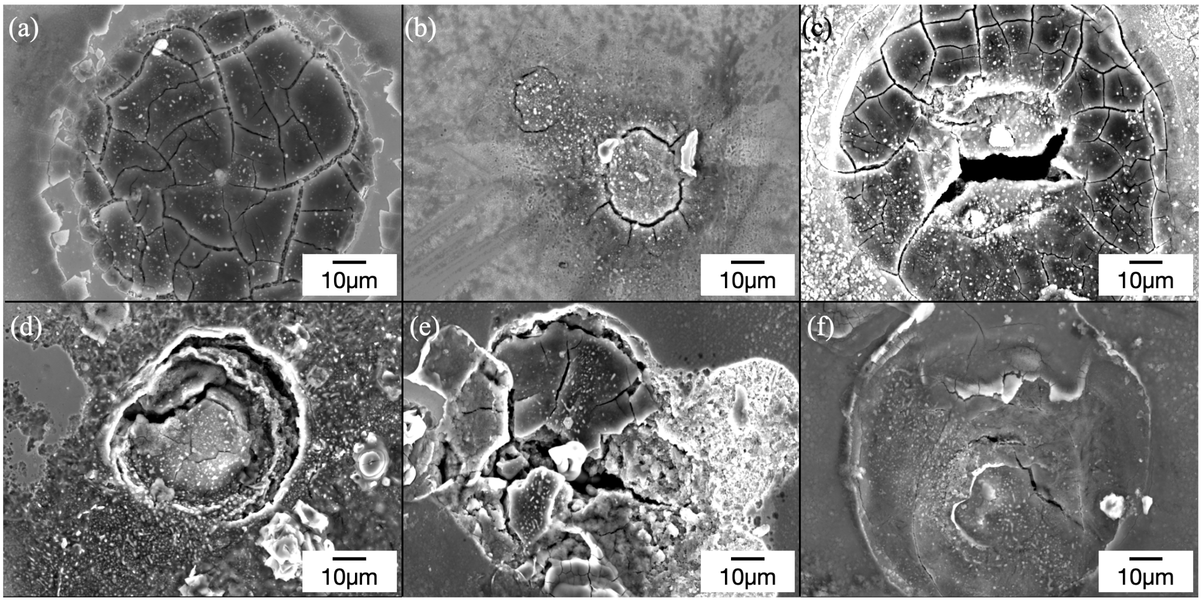

Figure 47: SEM images at X1000 of the pitting corrosion occurring in the 100Cr6 bearing steel with masking without and with 0.5 wt% Cu respectively. TM-160 (a, d), TM-240 (b, e), B (c, f)

Pitting corrosion was dominant for the steel sample that had undergone a corrosion test with masking. Figure 47 gives the shape of the pits in an SEM at X1000 magnification. It was observed that the pit size of the TM-240 without Cu was much smaller than the other types of steel. In addition, a very deep pit was seen for the bainite steel without Cu, similar to the findings from LOM images, suggesting that pitting corrosion was more severe for the bainite steel without Cu. The pit for TM-160 steel with 0.5 wt% Cu was surrounded by a layer of uniform corrosion.

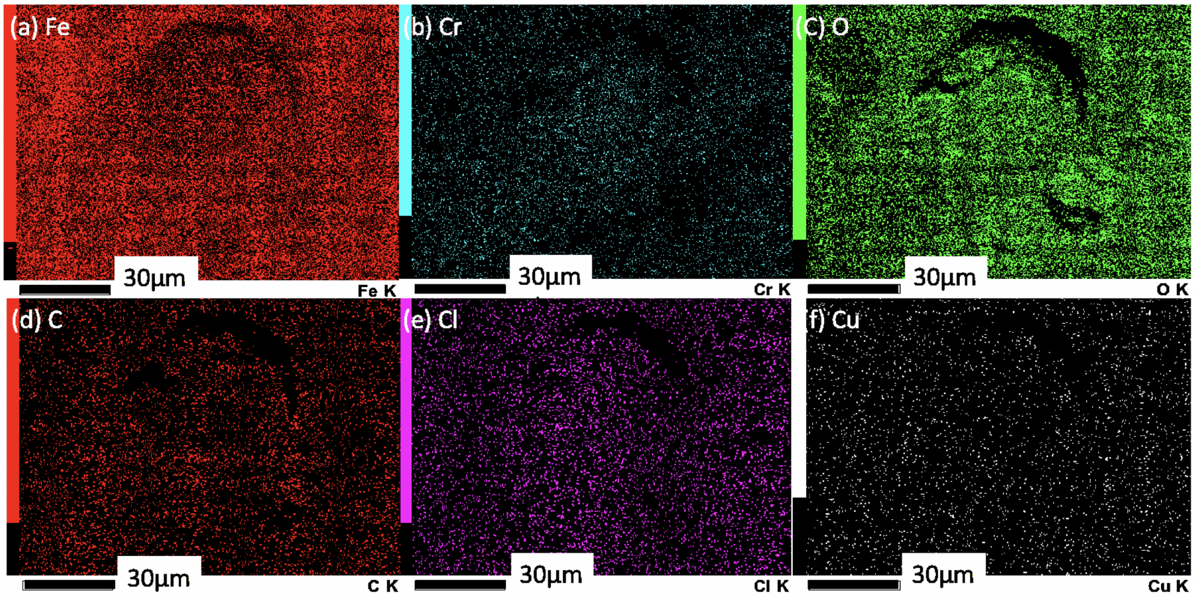

Figure 48: EDS pattern at X1000 of the pitting corrosion occurring in the TM-160 steel with masking with 0.5 wt% Cu

The EDS results showed the presence of Cu on the surface of the TM-160 steel with 0.5 wt%, while a similar EDS pattern for the steel sample before corrosion points towards the absence of Cu on the surface. Copper, as shown from the EDS pattern of the pitting corrosion in TM-160 steel in Figure 48f, was even distributed across the surface with a mass percentage of 1.54. It was unsure whether these copper existed as nanoparticles or if there was a layer of copper oxide on the surface of the steel. It can also be deduced from the pattern that Cl was concentrated at the location where the pit exists, suggesting that Cl has an important role in promoting the pitting corrosion of the steel. This observation was consistent with the findings from the literature review.

On the other hand, Cr was concentrated in the pit and around the pit, with the border of the pit showing a lack of Cr. This EDS mapping coincides with the EDS mapping of Fe and O. It was possible that Cr and Fe have undergone a similar corrosion process during the formation of the pit. Parallel observations were made of all the pits that were found in the steel samples with masking. Copper was the only thing missing from the pits in the steel without Cu. For some of the pits, Na and K from the electrolyte and Si, a source of contamination, were also detected by EDS.

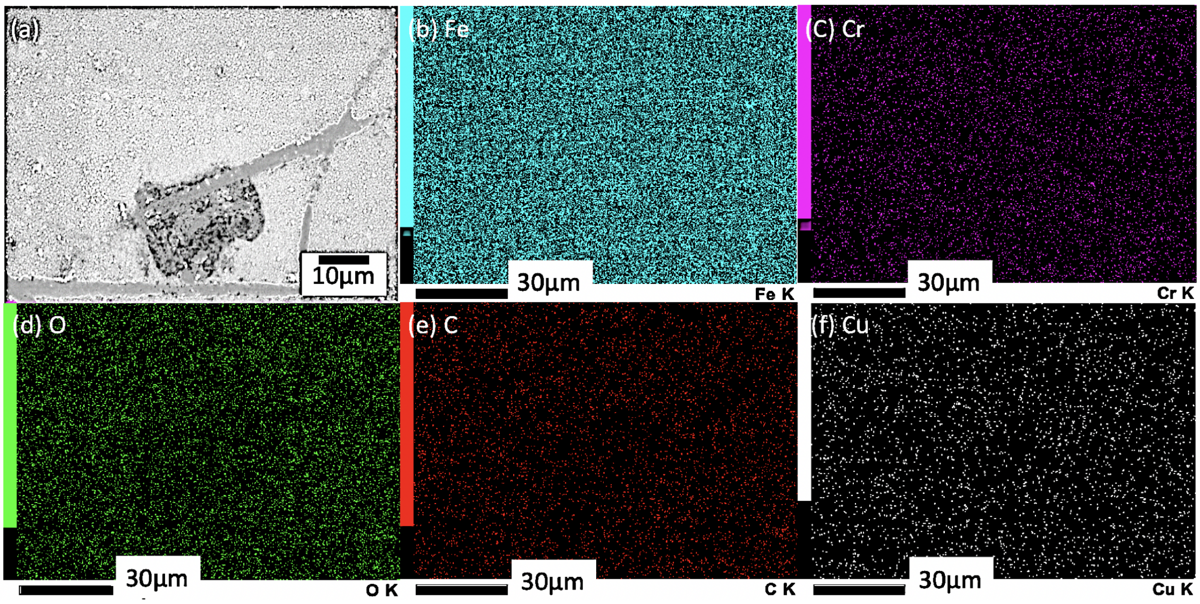

Figure 49: SEM image and EDS pattern at X1000 of the corrosion occurring in the B steel with masking with 0.5 wt% Cu

Figure 49 depicts the SEM images and corresponding EDS pattern of corrosion in the B steel with masking and with 0.5 wt% Cu. From the SEM image in Figure 49a, it can be observed that a layer of corrosion product was on the surface of the steel. Judging from the photo, no material loss was noticed; hence, it was not uniform corrosion but oxide products from the pitting corrosion nearby. The layer comprises five different elements, all distributed evenly across the image. However, Cl, a booster for pitting corrosion, was not found on the surface. Similar SEM images and EDS patterns were seen for steel without Cu, with only the Cu element missing from the EDS pattern. For some surfaces, Si, a source of contamination, was also seen in the EDS pattern.

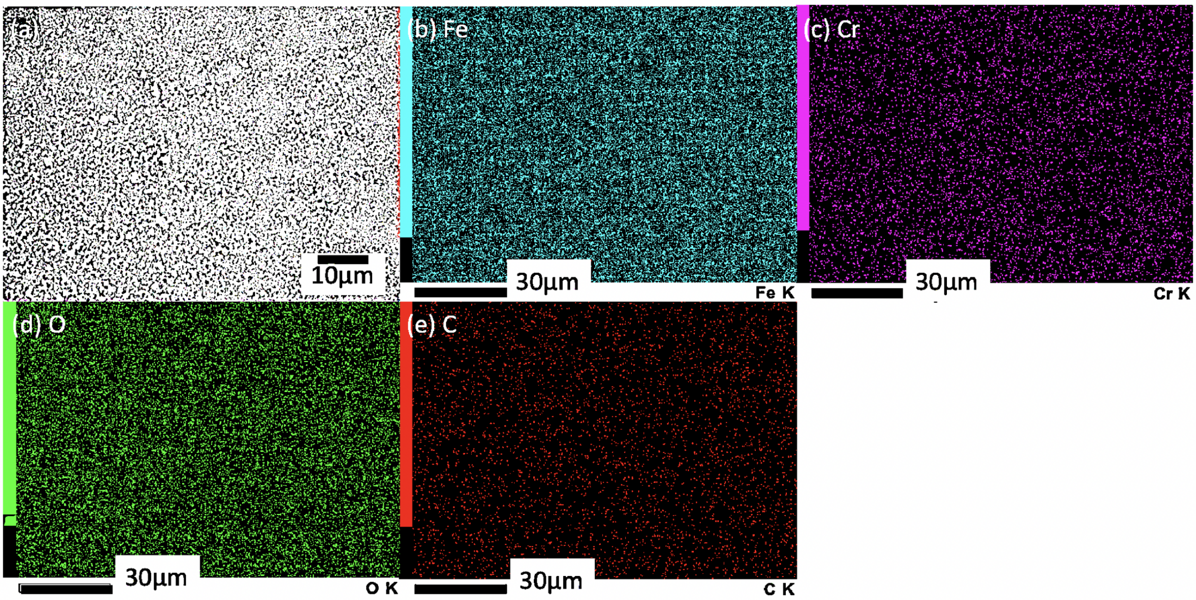

Figure 50: SEM image and EDS pattern at X1000 of the uniform corrosion occurring in the B steel with masking without Cu

Figure 50 depicts the SEM images and corresponding EDS pattern of uniform corrosion in the B steel with masking and without Cu. As seen from Figure 50a, the entire surface was covered by a layer of corrosion products. The EDS pattern in Figure 50 b, c, d, f suggested that there are regions with slightly lower intensity for Fe, Cr, O and C, particularly for Cr, which was more concentrated in some areas of the surface than other. Compared with the EDS pattern before the corrosion of the steel in Figure 36, where all Fe, Cr and C were evenly distributed. The uneven distribution of elements might suggest a loss of material from the surface. Hence, uniform corrosion might have occurred in this region.

In general, Cl was consistently detected in the EDS scan in regions where pitting corrosion occurred, whereas in locations where pitting corrosion did not happen, Cl was not found. This suggests that Cl has a vital role in the steel's pitting corrosion mechanism. Cu was detected in regions of corroded surfaces, indicating that Cu was part of the oxide layer on the surface of the corroded steel with 0.5 wt% Cu. Also, uniform corrosion was more prominent in steel without copper content.

4.4.4 XPS Patterns

A sizeable overlapping peak can be found for the Fe and O spectra from the XPS spectrum of the B steel without Cu after corrosion, as seen in Figure 51. After peak fitting of the Fe 2p spectra, the iron oxides on the surface were determined to be FeO and Fe_2O_3. The ratio of the oxides was around 1:1 after calculating the area under the graph. The peak fitting outcome of oxygen spectra also suggested the existence of FeOOH. This result was in line with the findings from the XRD pattern in Chapter 4.4.1. Chromium oxides, which cannot be detected using XRD, were also not detected by XPS in this material. The detection limit of XPS is at 0.1 at%. It was unlikely to not detect Cr given that the amount of Cr in the steel was at about 1.5 wt%. Therefore, the most convincing possibility was that chromium was not part of the corrosion layer on the surface.

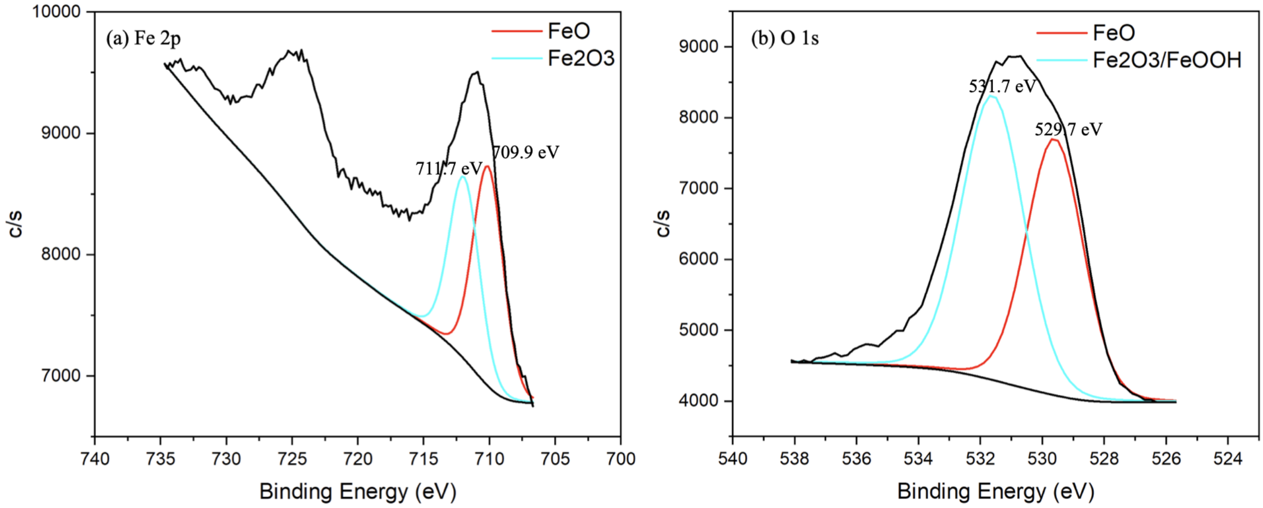

Figure 51: XPS spectrum of the B steel without Cu after corrosion, (a) is the spectra for Fe 2p, (b) is the spectra of O 1s

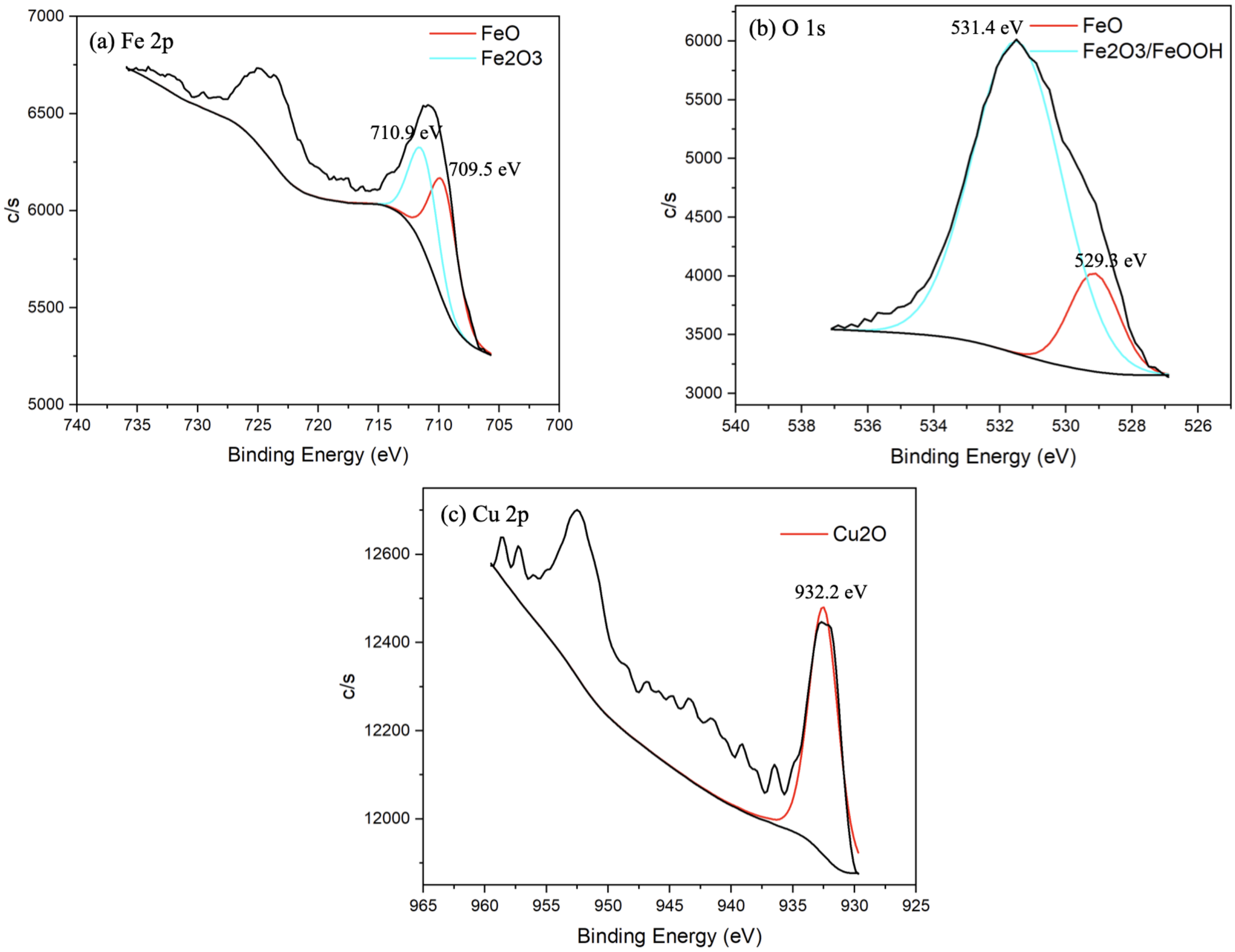

Figure 52: XPS spectrum of the B steel with 0.5 wt% Cu after corrosion, (a) is the spectra for Fe 2p, (b) is the spectra of O 1s, (c) is the spectra for Cu 2p

The XPS spectrum of the B steel with 0.5 wt% Cu showed related results for the iron oxide, but the ratio of FeO and Fe_2O_3 was now 45:55, and the majority of iron oxides existed in the state of FeOOH, as seen from the oxygen spectra in Figure 52. In addition, the amount of iron oxide was much lower for this steel than for the B steel without Cu. The Cu spectra gave distinctive peaks belonging to Cu_2O. The ratio of the Cu_2O was much lower compared to the iron oxide. Oxides belonging to Cr was not detected on the surface.

Overall, the XPS results supported the findings from XRD, SEM, and EDS, confirming the presence of FeO, Fe_2O_3, and FeOOH on the steel's surface. Cu_2O was also detected in the steel, with 0.5 wt% Cu. The XRD finding that chromium oxide was absent from the steel surface was also affirmed despite EDS results suggesting otherwise. The overall summary of the oxides detected by each technique can be seen in Table 7

Table 7: General overview of the oxides detected using various techniques, independent of the sample

Oxides	Detected in 1D XRD?	Detected in 2D XRD?	Detected in XPS?
FeO	Yes	Uncertain	Yes
Fe_2O_3	Uncertain	Yes	Yes
Fe_3O_4	No	Yes	No
FeOOH	No	Yes	Yes
Cu_2O	Uncertain	Uncertain	Yes
Cr_2O_3	No	No	No
Cr_2O_5	No	No	No

5 Discussion

The study of copper's effect on the corrosion of high-carbon bearing steel suggests that copper boosts the steel's corrosion resistance despite the extent of its effectiveness varying with different phases. Copper has also changed the microstructure formation during the heat treatment process. Therefore, this chapter will discuss the effect of copper on high-carbon-bearing steel.

5.1 Effect of Copper on the Microstructure Formation

5.1.1 Copper as an Austenite Stabiliser

Copper is a well-known austenite stabiliser, which also suppresses martensite transformation (Ma, Song, Jiang, & Rong, 2022; Yuan, Xi, Yang, Zhao, & Yang, 2020). It was expected that the austenite start and finish temperature and the martensite start and finish temperature would decrease due to the presence of copper in the steel. As shown in the phase change diagram for heating in Figure 29, the austenite start and end temperature drop when 0.5 wt% Cu was added to the steel.

However, such a conclusion cannot be drawn from the change in relative length vs temperature graph for the non-linear cooling part of the steel in Figure 30. The Ms temperature of the steel with 0.5 wt% Cu was higher than that of the steel without Cu. Comparing all the data collected, as shown in Table 4, the Ms temperature for TM-160 and TM-240 steel with 0.5 wt% Cu was inconsistent for the three tests, varying between 153 °C and 172 °C. In contrast, the temperature was consistent for the steel samples without copper (around 163 °C). The Ms temperature refers to the temperature at which austenite begins to transform into martensite. It mainly depends on the composition of the material, but austenitising state, external stresses, grain size and stored deformation energy can also play a vital role (Capdevila, 2012). The inconsistency in the readings could be due to the presence of copper in the steel.

$$\begin{aligned} M_s\,(^{\circ}\mathrm{C},\ \mathrm{wt.\%}) &= 545 - 330\mathrm{C} \\ &\quad + 2\mathrm{Al} + 7\mathrm{Co} - 14\mathrm{Cr} - 13\mathrm{Cu} - 23\mathrm{Mn} - 5\mathrm{Mo} \\ &\quad - 4\mathrm{Nb} - 13\mathrm{Ni} - 7\mathrm{Si} + 3\mathrm{Ti} + 4\mathrm{V} + 0\mathrm{W} \end{aligned}$$

Figure 53: Ishida model equation for the estimating of the effect of alloy element on the Ms value of steel (Ishida, 1995).

The Ms temperature recorded during the non-linear cooling was also much lower than the value from the CCT diagram for 100Cr6 bearing steel (305 °C) shown in Figure 24. The austenitising temperature used in the CCT diagram was 850 °C, while the austenitising duration and degree of austenitisation were unknown. The vast difference in Ms temperature could be due to an incomplete austenite transformation in the CCT diagram. In addition, the austenite grain size and difference in chemical composition could also contribute to the deviation in Ms value. Using the Ishida model equation for the estimating of the effect of alloy element on the Ms value of steel shown in Figure 53, the Ms temperature for the bearing steel used in the experiment was estimated to be around 186 °C, which is much more similar to the results recorded (163 °C).

5.1.2 Effect of Copper on Tempering

Copper showed no visible effect on tempering, as derived from the similar shape of the dilatometry curves shown in Figure 32, LOM and SEM images of the TM-160 and TM-240 steel with and without copper content. This finding was in line with literature sources, which state that tempering steel with copper gives no visible difference in the microstructure of the steel (Salvetr et al., 2020). However, a slight increase in change in relative length was observed during tempering when copper was added to steel, as shown in Figure 28. This could be due to copper's austenite stabilising ability, as more retained austenite remained after quenching and then transformed during tempering, leading to the higher change in relative length for the copper-containing steel. Also, it was noted from the overall XRD pattern in Figure 39 and from Table 6 that retained austenite was slightly more significant in the samples with copper content after tempering.

5.1.3 Effect of Copper on Austempering

As shown in Figure 28c and d, copper significantly influenced the austempering process. The time taken for both incubation and transformation increases for the steel with copper. From the SEM images in Figure 35c and f, the grains in the steel with copper content were finer than that of the steel without copper, with the latter showing a more distinctive sheaves microstructure. From the observations, copper alters the morphology of bainite. During the process, multiple mechanisms were simultaneously working. These included the nucleation of the bainite nucleus, the lengthening of the sheaves, etc. With the information at hand, the specific mechanism that was restricted by the presence of copper cannot be determined. A reasonable explanation will be that copper is an austenite stabiliser; this property of copper retarded the growth of bainitic ferrite. As a result, a much longer time was needed to develop the bainite phase in the steel. Nevertheless, further research is required to explain the heat treatment curve for bainite formation.

5.1.4 Effect of Copper on Phase Composition

From the overall XRD pattern in Figure 39, retained austenite and cementite peaks were slightly more evident in steel samples with copper content. However, the difference was very marginal. From Table 6, the fraction of retained austenite in TM-160 with copper was only 1 % higher than that without copper, while the results were the same for TM-240. Nevertheless, it would not be surprising for the amount of retained austenite in TM-160 and TM-240 steel with 0.5 wt% Cu to be higher, given the austenite stabilising effect of copper. Copper cannot suppress cementite formation during bainitic transformation (Yıldırım, 2022). Therefore, the amount of cementite in B steel with and without copper should be the same. The difference in cementite content could be due to the bainite phase's slower growth rate in the steel sample with 0.5 wt% Cu.

5.2 Effect of Copper on Corrosion

The clear-cut conclusion will be that copper is effective against corrosion in high-carbon bearing steel, the expected outcome supported by the literature review. The XRD and XPS results from Figure 48 and Figure 52 also proved the accumulation of copper on the steel's surface and the presence of Cu_2O in the oxide layer. Cu_2O was detected in the XRD pattern and the XPS spectrum. EDS mapping of the corroded steel surface with copper content in Figure 48 and

Figure 49 also showed that copper was distributed uniformly on the surface. Therefore, it can be confirmed that there was a passive layer with Cu_2O on the surface of the steel, which will be capable of shielding the steel underneath it from further corrosion, as described in Chapter 2.1.2

Comparing the EDS map and XPS spectrum before and after corrosion, both techniques could not detect copper on the surface of the steel before corrosion but showed precise mapping or spectra of copper on the surface after corrosion. This phenomenon suggested that copper was deposited and accumulated on the surface of the steel during the corrosion process. The deposition of copper precipitates on the surface of the steel will be capable of weakening the galvanic effect between different phases in the steel, thus suppressing the corrosion rate of the steel, as described in Chapter 2.1.3.

5.2.1 Effectiveness of Copper Against Corrosion in Different Phases

Copper's effectiveness against corrosion in different phases depends on how readily corrosion occurs in each phase. The corrosion rate of the TM-160 and B steel was higher than that of the TM-240 steel. This was due to the presence of retained austenite in TM-160 and cementite in B steel. As discovered in Chapter 2.2.2, retained austenite in tempered martensite and cementite in bainitic ferrite will promote corrosion on the surface of the steel by enhancing the galvanic effect. Retained austenite and cementite are less prone to corrosion than tempered martensite or bainite. Therefore, during the reaction, retained austenite in tempered martensite and cementite in bainitic ferrite will act as cathodes and continuously enhance the galvanic effect between the two phases, leading to severe corrosion.

As confirmed by the XRD pattern in Figure 39, TM-160 contained a considerable amount of retained austenite, and B contained cementite. The peaks for retained austenite were much smaller for TM-240 compared to TM-160, and the peaks for cementite were not visible in the XRD pattern, suggesting that TM-240 contained much lesser retained austenite (8 % << 20 %) and a negligible amount of cementite.

Therefore, due to the significant presence of retained austenite in tempered martensite for TM-160, the corrosion rate of the steel will be very high. Thus, copper's ability to suppress the galvanic effect will be more effective in TM-160 steel. The corrosion rate calculated in Table 5 for TM-160 steel with masking supports this conclusion. In addition, the corrosion potential for the TM-160 with Cu, shown in Table 5, was also higher, suggesting that it has a lower tendency to rust, as high corrosion potential indicates a lower possibility for metals to corrode (Kedici, Aksüt, Kílíçarslan, Bayramog Lu, & Gökdemir, 1998).

For TM-240, copper's ability to hinder the galvanic effect is limited due to the decreased percentage of retained austenite and the lack of cementite. Thus, the impact of copper on the corrosion of TM-240 steel is expected to be less visible. This hypothesis aligns with the results tabulated in Table 5 for TM-240 steel with masking, with the corrosion rate showing a mild decrease when 0.5 wt% Cu was added to the steel. However, the corrosion potential in Table 5 declined when copper was added, indicating a higher tendency for corrosion. Nevertheless, there is nothing to worry about, as the lower potential was likely due to the instability of the OCP curve and the Tafel plot when collecting the results.

Likewise, the galvanic effect between the cementite phase and the bainitic ferrite phase in B steel was suppressed by the presence of copper on the steel's surface. Therefore, copper was expected to be more effective in B steel than in TM-240 steel, as shown by the corrosion rate of the two steels in Table 5. The higher corrosion potential for B with copper also indicates a lower likelihood of corrosion. The difference in effectiveness in TM-160 and B could be due to the microstructure's inhomogeneity level. By comparing the area under the peaks for austenite and cementite in the XRD pattern in Figure 39, it was noticed that the proportion of retained austenite in TM-160 was higher than the percentage of cementite in B. Therefore, the level of inhomogeneity in TM-160 will be higher than that of B steel, resulting in a higher degree of suppression of galvanic effect, and thus leading to an overall higher effectiveness of copper in TM-160 than in B.

In general, copper is the most effective against corrosion in the less-tempered martensite phase, with a large amount of retained austenite (TM-160), followed by the bainite phase (B). Copper is the least efficient against corrosion in the more-tempered martensite phase, with a limited amount of retained austenite (TM-240).

5.2.2 Pitting Corrosion

The LOM images of the corroded steel with masking shown in Figure 46 show pitting corrosion for all the steels. The average size of the pits in TM-160 and TM-240 with copper was more significant than that in TM-160 and TM-240 without copper despite the lower corrosion rate recorded from the test results. More pits were also found for the TM-240 with copper than for TM-240 without copper. It was understood here that copper promotes the pitting corrosion of the steel while restricting the uniform corrosion on the surface, a finding already concluded from the literature review in chapter 2. The impact of the restriction was more dominant than the enhancement of pitting corrosion, resulting in a drop in the overall corrosion rate when copper was added to the steel. However, the average pit size and number of pits observed in the sample without copper were more prominent than in the sample with copper for B steel, as shown in Figure 46c and f. It seemed to be that copper also suppresses pitting corrosion for bainite.

In addition, Cl was detected in the EDS map in regions with pitting corrosion but not in other areas, as shown in Figure 48 and Figure 50. This observation suggests that the chloride ions may have promoted the pitting corrosion on the steel's surface. As mentioned in Chapter 2.3.1, chloride ions dissolved the iron oxide in the corrosion layer, exposing the steel underneath it to corrosion. The new iron oxide formed will again dissolve in the chloride solution, repeating the cycle continuously. As a result, Cl promotes pitting corrosion, resulting in the formation of deep pits.

5.2.3 Uniform Corrosion

Uniform corrosion occurs only when material is lost from the surface. A minimum amount of uniform corrosion was detected in the steel samples, both with and without copper. In many suspected uniform corrosion cases, the oxide layers from pitting corrosion covered the surface without any material loss in that region, as shown in Figure 49. This is not uniform corrosion, as uniform corrosion implies a material loss from the steel surface. However, some suspected cases of such corrosion were discovered, mainly in B steel without copper, as shown in Figure 50. This supports the literature review's conclusion that copper suppressed uniform corrosion, as uniform corrosion was not found in steel samples with copper content. Also, when regions more prone to corrosion exist (pitting sites), pitting corrosion is more likely to occur than uniform corrosion.

5.2.4 Interfering Effect Between Cr and Cu

Cu_2O was detected in the XPS spectrum in Figure 52c of the steel with copper, while no trace of any chromium was found in the XRD or XPS scan. This shows that the oxide layer from corrosion consists of copper oxide, iron oxide and iron hydroxide. At the same time, there is no evidence that chromium participates in forming the passivation layer. Hence, there is no interfering effect between Cr and Cu.

6 Conclusion

In summary, the effect of copper on the corrosion of martensitic or bainitic through-hardened high-carbon bearing steel was investigated in an attempt to turn copper from a tramp element to an alloy element in steels manufactured from steel scrap. The following results were concluded from the experiment.

1. The electrochemical polarisation test showed that adding 0.5 wt% Cu to the steel slightly increased the corrosion resistance of the steel. The effect was most prominent in steel tempered at 160 °C (TM-160), followed by bainite steel (B). The difference in corrosion rate was insignificant in steel tempered at 240 °C (TM-240). The open circuit potential and corrosion potential of TM-160 and B steel with copper were also higher, indicating a lower tendency to rust.
2. The test results also showed that TM-160 and B steel have a much higher corrosion rate than TM-240 steel. It was observed from the XRD results that retained austenite was present in TM-160, while cementite was present in B steel. TM-240 steel contains little amounts of both retained austenite and cementite. It was believed that the retained austenite in TM-160 and cementite particles in B boost the corrosion on the steel surface due to the galvanic effect.
3. Pitting corrosion occurred in all the steel samples, with Cl detected in the EDS mapping nearing the pitting corrosion sites of the steel. This showed that Cl was involved in the pitting corrosion, promoting it and resulting in the formation of deep pits.
4. XRD pattern and XPS spectrum suggest that Cu_2O was present in the oxide layer, while no evidence showed the availability of chromium oxide in the layer. Hence, there is no interfering effect between Cu and Cr.
5. It was clear from the dilatation curves that copper was an austenite stabiliser, with austenite start and end temperature dropping with the addition of copper. The fluctuation in martensite start temperature and higher relative change in length during tempering for steel with copper could also be due to the austenite stabilising effect of copper.
6. Likewise, the presence of copper seems to influence the austempering process significantly, with a much more prolonged incubation and transformation time observed for steel with copper. The reason behind this is still unknown; further research is needed to explore the reasoning behind the observation.

From there, a few recommendations for future experiments are suggested.

1. The Electrochemical polarisation test is not the best option for performing corrosion tests on high-carbon bearing steel due to fluctuation in data. A combination of both the weight-loss method and the electrochemical test should provide a more complete analysis.
2. XPS can only detect the existence of iron and copper oxides on the surface after corrosion but cannot monitor the deposition and accumulation of copper on the surface. Another technique would be needed, and a suggestion would be using Auger Electron Spectroscopy (AES) depth profile.
3. Pitting corrosion was most prominent in the steel; an analysis of the pit size and depth could provide more information on the pitting corrosion and its severity in different samples.

7 Acknowledgement

Richard Huizenga, from the Department of Materials Science and Engineering of the Delft University of Technology, has been acknowledged for the XRD analysis.

Prasaanth Ravi Anusuyadevi and Prasad Gonugunta from the Department of Materials Science and Engineering of the Delft University of Technology, have been acknowledged for the XPS analysis.

References

Banas, J., & Mazurkiewicz, A. (2000). The effect of copper on passivity and corrosion behaviour of ferritic and ferritic–austenitic stainless steels. *Materials Science and Engineering: A*, *277*(1-2), 183–191.

Banerjee, M. (2017). 2.1 fundamentals of heat treating metals and alloys. *Comprehensive materials finishing*, 1–49.

Bhadeshia, H. (2012). Steels for bearings. *Progress in materials Science*, *57*(2), 268–435.

Biesinger, M. (2015). X-ray photoelectron spectroscopy (xps) reference pages. *Surface Science Western, University of Western Ontario, Ontario.*

Cao, Z., Liu, T., Yu, F., Cao, W., Zhang, X., & Weng, Y. (2020). Carburization induced extra-long rolling contact fatigue life of high carbon bearing steel. *International Journal of Fatigue*, *131*, 105351.

Capdevila, C. (2012). Neural networks modeling of phase transformations in steels. In *Phase transformations in steels* (pp. 464–503). Elsevier.

Cavaliere, G. (2023). *Analysis on copper, lead and tin removal in steel scrap sorting: Technologies involved, environmental considerations and economic aspects.*

Choi, Y.-S., Shim, J.-J., & Kim, J.-G. (2005). Effects of cr, cu, ni and ca on the corrosion behavior of low carbon steel in synthetic tap water. *Journal of alloys and compounds*, *391*(1-2), 162–169.

Counts, T. W. (2018). *Most recycled material in the world.* Retrieved from `https://www.theworldcounts.com/challenges/planet-earth/mining/advantages-of-recycling-steel`

Daehn, K. E., Serrenho, A. C., & Allwood, J. (2019). Finding the most efficient way to remove residual copper from steel scrap. *Metallurgical and Materials Transactions B*, *50*, 1225–1240.

Díaz, I., Cano, H., Lopesino, P., De la Fuente, D., Chico, B., Jiménez, J. A., … Morcillo, M. (2018). Five-year atmospheric corrosion of cu, cr and ni weathering steels in a wide range of environments. *Corrosion Science*, *141*, 146–157.

El-Egamy, S. (2008). Corrosion and corrosion inhibition of cu–20% fe alloy in sodium chloride solution. *Corrosion Science*, *50*(4), 928–937.

El Ibrahimi, B., & Berdimurodov, E. (2023). Weight loss technique for corrosion measurements. In *Electrochemical and analytical techniques for sustainable corrosion monitoring* (pp. 81–90). Elsevier.

Eurofer. (2015). *Steel and the circular economy.* Retrieved from `https://www.eurofer.eu/assets/Uploads/20151016_CircularEconomyA4.pdf`

European Parliament. (2023). *Circular economy: definition, importance and benefits.* Retrieved from `https://www.europarl.europa.eu/topics/en/article/20151201STO05603/circular-economy-definition-importance-and-benefits#:~:text=The%20circular%20economy%20is%20a,cycle%20of%20products%20is%20extended.`

Fan, L., Sun, Y., Wang, D., Zhang, Y., Zhang, M., Zhou, E., … Wang, F. (2023). Microbiologically influenced corrosion of a novel pipeline steel containing cu and cr elements in the presence of desulfovibrio vulgaris hildenborough. *Corrosion Science*, *223*, 111421.

Foster, D., Paladugu, M., Hughes, J., Kapousidou, M., Islam, U., Stark, A., … Jimenez-Melero, E. (2022). Formation of lower bainite in a high carbon steel–an in-situ synchrotron xrd study. *journal of materials research and technology*, *18*, 5380–5393.

Fu, J. (2016). Microstructure and corrosion behavior of hot-rolled gcr15 bearing steel. *Applied Physics A*, *122*(4), 416.

Global high carbon bearing steel market research report 2022-2032. (2024, February). Fatpos Global Pvt. Ltd. Retrieved from `https://www.reportlinker.com/p06382429/Global-High-Carbon-Bearing-Steel-Market-Research-Report-2032.html?utm_source=GNW`

Government of Netherlands. (n.d.). *Circular dutch economy by 2050.* Retrieved from `https://www.government.nl/topics/circular-economy/circular-dutch-economy-by-2050`

Gupta, S. K., Manna, R., & Chattopadhyay, K. (2023). Effect of austempering time on electrochemical and immersion corrosion behaviour of high carbon, carbide-free nanostructured bainitic steel in an aqueous 3.5% nacl. *Metals and Materials International*, *29*(9), 2533–2555.

Hao, X., Dong, J., Wei, J., Etim, I.-I. N., & Ke, W. (2017). Effect of cu on corrosion behavior of low alloy steel under the simulated bottom plate environment of cargo oil tank. *Corrosion Science*, *121*, 84–93.

Hao, X., Zhao, X., Chen, H., Huang, B., Ma, J., Wang, C., & Yang, Y. (2021). Comparative study on corrosion behaviors of ferrite-pearlite steel with dual-phase steel in the simulated bottom plate environment of cargo oil tanks. *Journal of Materials Research and Technology*, *12*, 399–411.

He, B. B. (2003). Introduction to two-dimensional x-ray diffraction. *Powder diffraction*, *18*(2), 71–85.

Hillert, M. (1962). The formation of pearlite. *Decomposition of Austenite by Diffusonal Process*.

Hong, I., & Koo, C. H. (2005). Antibacterial properties, corrosion resistance and mechanical properties of cu-modified sus 304 stainless steel. *Materials Science and Engineering: A*, *393*(1-2), 213–222.

Hong, J., Lee, S., Kim, J., & Yoon, J. (2012). Corrosion behaviour of copper containing low alloy steels in sulphuric acid. *Corrosion science*, *54*, 174–182.

Industrial Metallurgists, L. (n.d.). *Why temper through hardened steel.* Retrieved from `https://www.imetllc.com/hardened-steel-tempered/#:~:text=During%20the%20tempering%20process%20the,any%20given%20period%20of%20time.`

Ishida, K. (1995). Calculation of the effect of alloying elements on the ms temperature in steels. *Journal of Alloys and Compounds*, *220*(1-2), 126–131.

Jang, Y.-W., Hong, J.-H., & Kim, J.-G. (2009). Effects of copper on the corrosion properties of low-alloy steel in an acid-chloride environment. *Metals and Materials International*, *15*, 623–629.

Kedici, S., Aksüt, A. A., Kílíçarslan, M. A., Bayramog Lu, G., & Gökdemir, K. (1998). Corrosion behaviour of dental metals and alloys in different media. *Journal of oral rehabilitation*, *25*(10), 800–808.

Liu, H., Teng, Y., Guo, J., Li, N., Wang, J., Zhou, Z., & Li, S. (2021). Corrosion resistance and corrosion behavior of high-copper-bearing steel in marine environments. *Materials and Corrosion*, *72*(5), 816–828.

Lupu, F. C., Munteanu, C., Müftü, S., Benchea, M., Cimpoesu, R., Ferguson, G., … Arsenoaia, V. N. (2024). Evaluation of the wear properties and corrosion resistance of 52100 steel coated with ni/crc by cold spraying. *Coatings*, *14*(1), 145.

Ma, J., Song, Y., Jiang, H., & Rong, L. (2022). Effect of cu on the microstructure and mechanical properties of a low-carbon martensitic stainless steel. *Materials*, *15*(24), 8849.

Moon, A., Sangal, S., Layek, S., Giribaskar, S., & Mondal, K. (2015). Corrosion behavior of high-strength bainitic rail steels. *Metallurgical and Materials Transactions A*, *46*, 1500–1518.

Msallamova, S., Fojt, J., Novak, P., Salvetr, P., Michalcova, A., Kohoutkova, M., & Jaworska, L. (2023). Effects of cu microalloying on corrosion behavior of spring steel 54sicr6. *Materials Chemistry and Physics*, *309*, 128323.

Nidheesh, P., & Kumar, M. S. (2019). An overview of environmental sustainability in cement and steel production. *Journal of cleaner production*, *231*, 856–871.

Oguzie, E. E., Li, J., Liu, Y., Chen, D., Li, Y., Yang, K., & Wang, F. (2010). The effect of cu addition on the electrochemical corrosion and passivation behavior of stainless steels. *Electrochimica Acta*, *55*(17), 5028–5035.

Papavinasam, S. (2021). Electrochemical polarization techniques for corrosion monitoring. In *Techniques for corrosion monitoring* (pp. 45–77). Elsevier.

Pardo, A., Merino, M., Carboneras, M., Viejo, F., Arrabal, R., & Munoz, J. (2006). Influence of cu and sn content in the corrosion of aisi 304 and 316 stainless steels in h2so4. *Corrosion science*, *48*(5), 1075–1092.

Pardo, A., Merino, M., Coy, A., Arrabal, R., Viejo, F., & M'hich, A. (2007). Corrosion behaviour of aisi 304 stainless steel with cu coatings in h2so4. *Applied surface science*, *253*(23), 9164–9176.

Raabe, D., Jovičević-Klug, M., Ponge, D., Gramlich, A., da Silva, A. K., Grundy, A. N., … Ma, Y. (2024). Circular steel for fast decarbonization: Thermodynamics, kinetics, and microstructure behind upcycling scrap into high-performance sheet steel. *Annual Review of Materials Research*, *54*.

Sagüés, A. A. (1993). Corrosion measurement techniques for steel in concrete. In *Corrosion-national association of corrosion engineers annual conference-*.

Salvetr, P., Gokhman, A., Svoboda, M., Donik, Č., Podstranská, I., Kotous, J., & Novỳ, Z. (2023). Effect of cu alloying on mechanical properties of medium-c steel after long-time tempering at 500° c. *Materials*, *16*(6), 2390.

Salvetr, P., Jakub Kotous, J., Zmeko, J., Zbyšek Novỳ, Z., Motyčka, P., Dlouhỳ, J., & Gokhman, O. R. (2020). Influence of si and cu content on tempering and properties of 54sicr6 steel.

Samusawa, I., & Nakayama, S. (2019). Influence of plastic deformation and cu addition on corrosion of carbon steel in acidic aqueous solution. *Corrosion Science*, *159*, 108122.

School, C. B. (2024). *Steel sector overview.* Retrieved from `https://leading.business.columbia.edu/climate/steel/decarbonizing-steel/overview`

Sekunowo, O. I., Durowaye, S. I., & Gbenebor, O. P. (2014). Effect of copper on microstructure and mechanical properties of construction steel. *International Journal of Chemical, Molecular, Nuclear, Materials and Metallurgical Engineering*, *8*(8), 839–843.

Sun, B., Zuo, X., Cheng, X., & Li, X. (2020). The role of chromium content in the long-term atmospheric corrosion process. *npj Materials Degradation*, *4*(1), 37.

Sun, Y., Zhong, Y., & Wang, L. (2019). The interaction between ε-copper and dislocation in a high copper 17-4ph steel. *Materials Science and Engineering: A*, *756*, 319–327.

Syrett, B., & Begum, S. (2016). Corrosion, crevice. In *Reference module in materials science and materials engineering.* Elsevier. Retrieved from `https://www.sciencedirect.com/science/article/pii/B9780128035818027090` doi: https://doi.org/10.1016/B978-0-12-803581-8.02709-0

Tran, X. T., Vu, T. D., & Dang, K. Q. (2017). Numerical simulation of the heat treatment process for 100cr6 steel. *Acta Metallurgica Slovaca*, *23*(3), 236–243.

Ujiro, T., Satoh, S., Staehle, R., & Smyrl, W. (2001). Effect of alloying cu on the corrosion resistance of stainless steels in chloride media. *Corrosion Science*, *43*(11), 2185–2200.

Williams, E., & Komp, M. (1965). Effect of copper content of carbon steel on corrosion in sulfuric acid. *Corrosion*, *21*(1), 9–14.

Wu, J. (2017). *Pantograph and contact line system.* Academic Press.

Xi, T., Shahzad, M. B., Xu, D., Sun, Z., Zhao, J., Yang, C., … Yang, K. (2017). Effect of copper addition on mechanical properties, corrosion resistance and antibacterial property of 316l stainless steel. *Materials Science and Engineering: C*, *71*, 1079–1085.

Xu, Q., Gao, K., Lv, W., & Pang, X. (2016). Effects of alloyed cr and cu on the corrosion behavior of low-alloy steel in a simulated groundwater solution. *Corrosion Science*, *102*, 114–124.

Yamanaka, K., Mori, M., Yoshida, K., Onuki, Y., Sato, S., & Chiba, A. (2021). Surface evolution and corrosion behaviour of cu-doped carbide-reinforced martensitic steels in a sulfuric acid solution. *npj Materials Degradation*, *5*(1), 43.

Yang, L. (2020). *Techniques for corrosion monitoring.* Woodhead Publishing.

Yasakau, K., Zheludkevich, M., & Ferreira, M. (2018). Role of intermetallics in corrosion of aluminum alloys. smart corrosion protection. *Intermetallic matrix composites*, 425–462.

Yıldırım, Ç. (2022). *The effect of copper on the microstructure and aging characteristics of an 0.8% c bainitic steel* (Unpublished master's thesis). Middle East Technical University.

Yuan, Z., Xi, T., Yang, C., Zhao, H., & Yang, K. (2020). Enhancement of strength and ductility by cu-rich precipitation in cu-bearing 304l austenitic stainless steel. *Materials Letters*, *272*, 127815.

Zhang, C., Yamanaka, K., Bian, H., & Chiba, A. (2019). Corrosion-resistant carbide-reinforced martensitic steel by cu modification. *NPJ Materials Degradation*, *3*(1), 30.

A Appendix: Corrosion Test Results for Samples with Masking

This appendix gives the raw corrosion test results (E*ocp*, E*corr*, corrosion density and corrosion rate) for the samples with masking. 100Cr6 (TM-240) test no. 2 was unreliable as a crack was discovered on the steel surface after corrosion.

Table A1: E*ocp* values of the bearing steel with masking against Ag/AgCl reference electrode

Steel	1 (mV)	2 (mV)	3 (mV)
100Cr6 (TM-160)	-287.750	-339.925	
100Cr6Cu (TM-160)	-297.085	-302.124	
100Cr6 (TM-240)	-211.015	-363.802	-284.496
100Cr6Cu (TM-240)	-258.176	-257.410	-292.181
100Cr6 (B)	-310.323	-320.610	
100Cr6Cu (B)	-303.301	-271.892	

Table A2: E*corr* values of the bearing steel with masking against Ag/AgCl reference electrode

Steel	1 (mV)	2 (mV)	3 (mV)
100Cr6 (TM-160)	-299.104	-313.481	
100Cr6Cu (TM-160)	-284.654	-284.305	
100Cr6 (TM-240)	-196.190	-351.882	-210.695
100Cr6Cu (TM-240)	-203.544	-217.259	-244.680
100Cr6 (B)	-316.455	-323.481	
100Cr6Cu (B)	-265.216	-268.077	

Table A3: Corrosion density of the bearing steel with masking

Steel	1 (µA/cm2)	2 (µA/cm2)	3 (µA/cm2)
100Cr6 (TM-160)	2.427	2.674	
100Cr6Cu (TM-160)	2.032	2.157	
100Cr6 (TM-240)	0.750	2.598	0.752
100Cr6Cu (TM-240)	0.531	0.868	0.736
100Cr6 (B)	2.484	2.656	
100Cr6Cu (B)	2.453	2.247	

Table A4: Corrosion rate of the bearing steel with masking

Steel	1 (mmpy)	2 (mmpy)	3 (mmpy)
100Cr6 (TM-160)	0.028390	0.031280	
100Cr6Cu (TM-160)	0.023794	0.025232	
100Cr6 (TM-240)	0.008774	0.030391	0.008797
100Cr6Cu (TM-240)	0.006212	0.010154	0.008610
100Cr6 (B)	0.029058	0.031070	
100Cr6Cu (B)	0.028695	0.026285	

The corrosion rate calculated was an estimation as an assumption that all iron oxidised to Fe^{2+} was made.

B Appendix: Corrosion Test Results for Samples without Masking

Table B1 gives the average corrosion results of the bearing steel without masking. Likewise, the OCP value was derived from the OCP curve, Ecorr and Icorr values were extrapolated from the Tafel plot and the corrosion rate was calculated by assuming iron was oxidised to Fe^{2+}, using the density of 100Cr6 bearing steel, a surface area of 0.126 cm2, and only taking the results of consistent measurements.

Table B1: Corrosion results of the 100Cr6 bearing steel without masking

Steel	Eocp (mV)	Ecorr (mV)	icorr (µA/cm2)	Corrosion rate (mmpy)
100Cr6 (TM-160)	-372.1	-340.0	4.31	0.0504 ± 0.0030
100Cr6Cu (TM-160)	-359.9	-322.7	3.37	0.0371 ± 0.0047
100Cr6 (TM-240)	-387.3	-355.1	3.58	0.0420 ± 0.0011
100Cr6Cu (TM-240)	-430.4	-388.3	3.46	0.0404 ± 0.0010
100Cr6 (B)	-377.1	-336.9	3.95	0.0462 ± 0.0035
100Cr6Cu (B)	-398.9	-381.7	4.98	0.0582 ± 0.0018

The data clearly showed that introducing Cu to the TM-160 yields the best resistance against corrosion, and the effect of copper on the corrosion of TM-240 was negligible. This result was consistent with the findings from the corrosion test with masking. However, when masking was not applied, copper seemed to boost the corrosion rate of the bainite phase, as shown by the increase in corrosion rate from 0.0482 mmpy for B, no Cu, to 0.0582 mmpy for B, 0.5 wt% Cu. Also, the corrosion rate for TM-240 was much higher than when masking was used.

Masking significantly lowers the corrosion rate of TM-240, possibly because it protects the side of the surface, regions more susceptible to attack, from corrosion. The other possibility is that crevice corrosion occurred in the steel without masking. Although the steel was embedded with a non-conductive resin, there was a possibility that the electrolyte (100ppm NaCl) could enter the interface between the steel and the resin. This increases the surface area in contact with the electrolyte, which will overestimate the corrosion rate. Masking, on the other hand, sealed the interface between the resin and the steel from any contact, thus preventing crevice corrosion from happening.

Figure B1 compares the Tafel plot between steels without masking with 0.5 wt% Cu and without Cu for TM-160, TM-240 and B. It was observed that the reduction curve of the Tafel plot often shows a very steep slope. This was a signal for lack of oxygen. This lack of oxygen could result from corrosion, like crevice corrosion, in regions with limited oxygen. The oxidation curve for the B with 0.5 wt% Cu shows a very steep slope. This was the outcome of even more severe corrosion occurring on the surface of the steel. Nevertheless, no passivation of the surface was observed.

In addition, as judged from the Tafel plot, the repeatability of the results was weaker than when masking was used. Masking provided a mirror surface for the corrosion. Hence, factors affecting the corrosion behaviour were minimal, leading to good reproducibility of the outcome. However, without masking, it exposed weak spots on the side of the steel and created room for crevice corrosion. Therefore, there will be more variables that need to be taken into account, leading to a less controllable result. The total result for the corrosion test without masking can be found below.

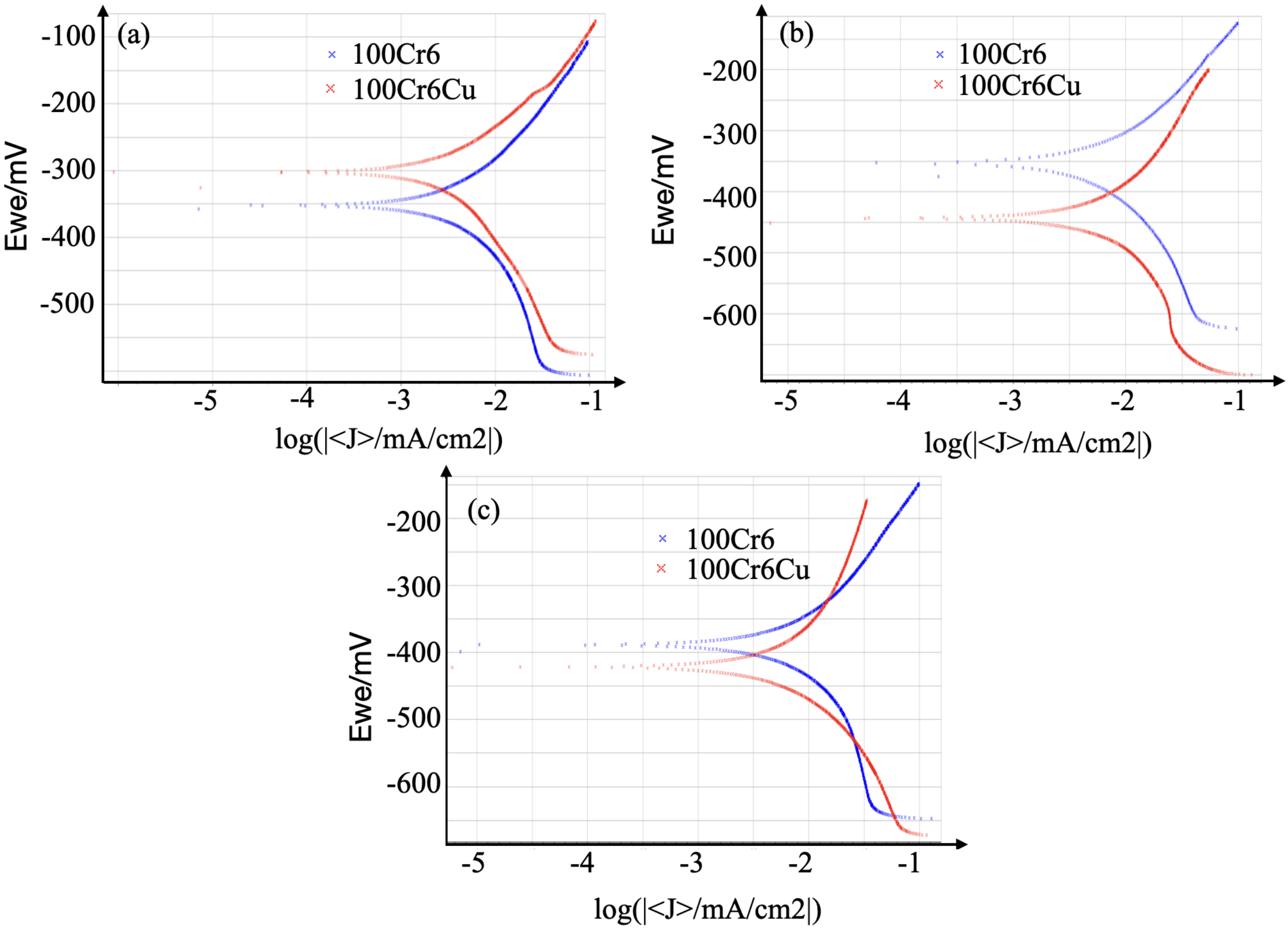

Figure B1: Tafel plot of the 100Cr6 steel without masking, (a) is for TM-160, (b) is for TM-240 and (c) is for B

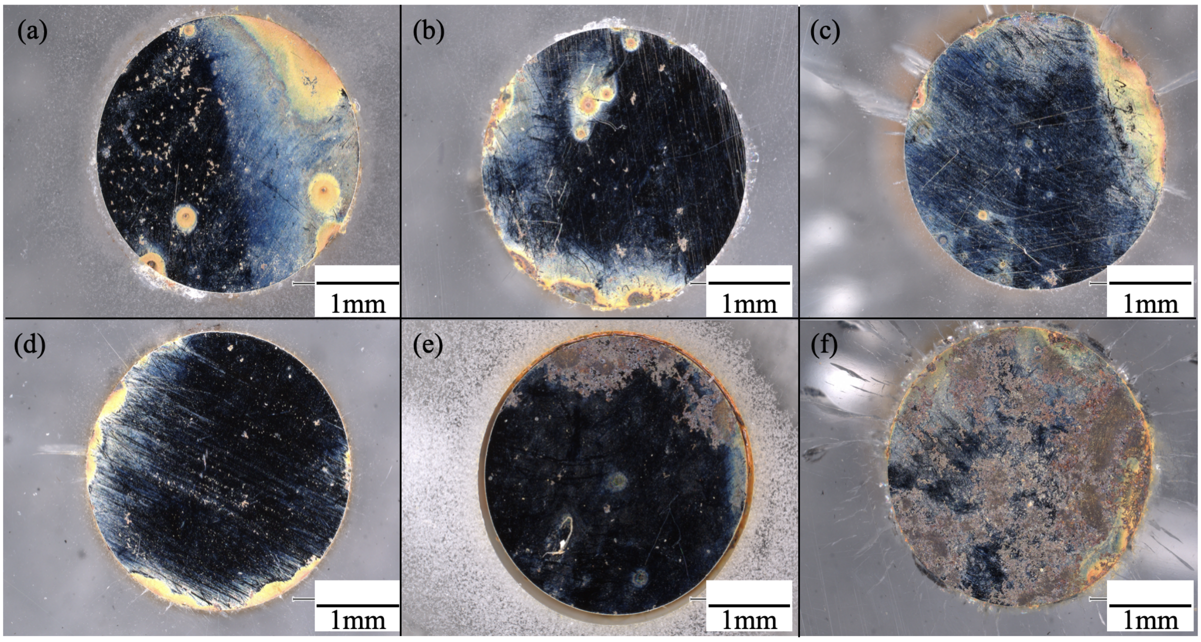

Figure B2: LOM images at X50 of the corroded steel without masking without and with 0.5wt% Cu respectively. TM-160 (a,d), TM-240 (b,e), B (c,f)

Figure B2 gives the LOM images of the general surface of the corroded steel without masking at X50 magnification. Pitting spots were observed in all samples without Cu, while uniform corrosion dominated the samples with 0.5wt% Cu. The level of corrosion on the surface of the steel correlates with the corrosion results obtained in Chapter 4.3, with the TM-160 steel with Cu showing only minor corrosion and the bainite steel with Cu giving the most apparent oxide layer on the surface. In addition, corrosion tends to be most serious on the side of the samples, with crevice corrosion visibly observed for most of the samples.

When the results were compared with those of the samples with masking, a very different corrosion mechanism was observed for the samples with copper. Judging from the images, masking changes the main form of corrosion on the surface from uniform corrosion to pitting corrosion. A reasonable explanation for this was that the side of the steel, as predicted, is highly susceptible to attacks, leading to corrosion concentrating only on the side of the steel. Hence, this resulted in a change in the corrosion mechanism.

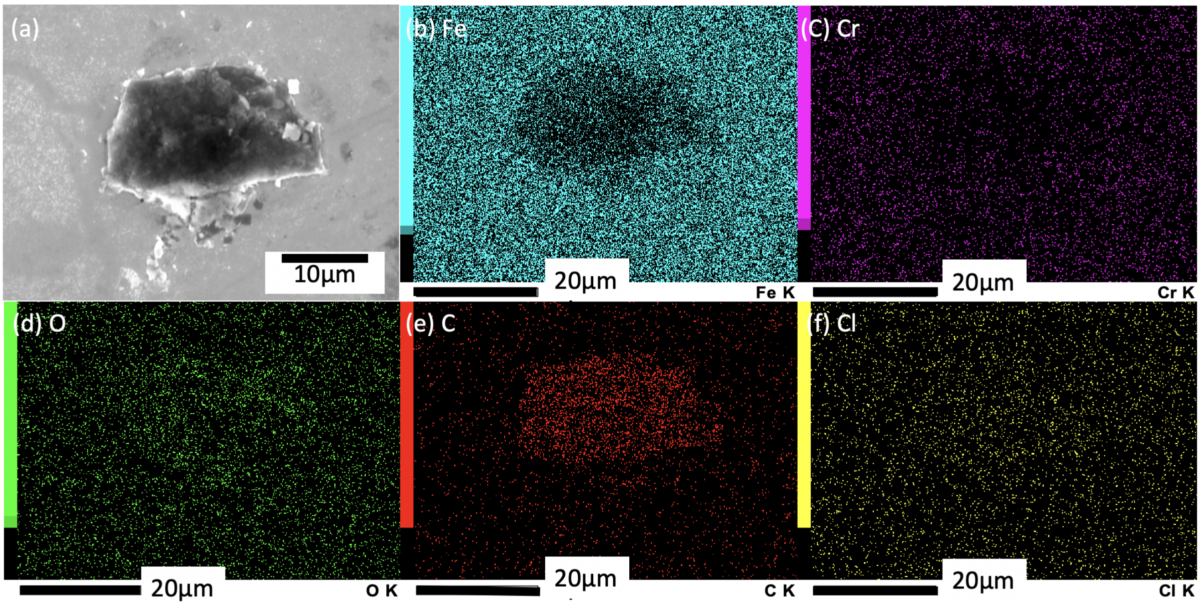

Figure B3: SEM image and EDS pattern at X2000 at the side of the TM-160 steel without masking with 0.5 wt% Cu

The pitting and uniform corrosion in the steel samples without masking share similar results with the steel with masking. It can be confirmed that a change in corrosion behaviour does not alter the overall outcome of the corrosion products. However, at the side of the steel where crevice corrosion was concentrated, black spots with a high intensity of carbon and low concentration of iron and chromium were found. It was unsure whether it was the cementite phase; what could be deduced was that these black spots could only be found near the side of the steel. The SEM image and EDS pattern of the black spots at X2000 magnification in the TM-160 steel without masking with 0.5 wt% Cu is seen in Figure B3. The intensity of other elements remains unchanged in the region of the black spot. From the EDS pattern, it seems that the black spots are cathodes that increase the corrosion of the surrounding steel surface, resulting in severe corrosion observed at the side of the steel without masking.

The black spots were also found in the B steel in regions near the side of the steel where crevice corrosion was less severe or did not occur. The EDS pattern shows a high intensity of carbon and a low intensity of iron, with oxygen missing from the EDS pattern. This proved that either the corrosion in this region was mild or did not occur at all. It was deduced that although these black spots might promote corrosion, they are not regions of weakness on the surface where corrosion might begin. The SEM image and EDS pattern at X500 magnification on the side of the bainite steel with 0.5 wt% at regions without corrosion is seen in Figure B4.

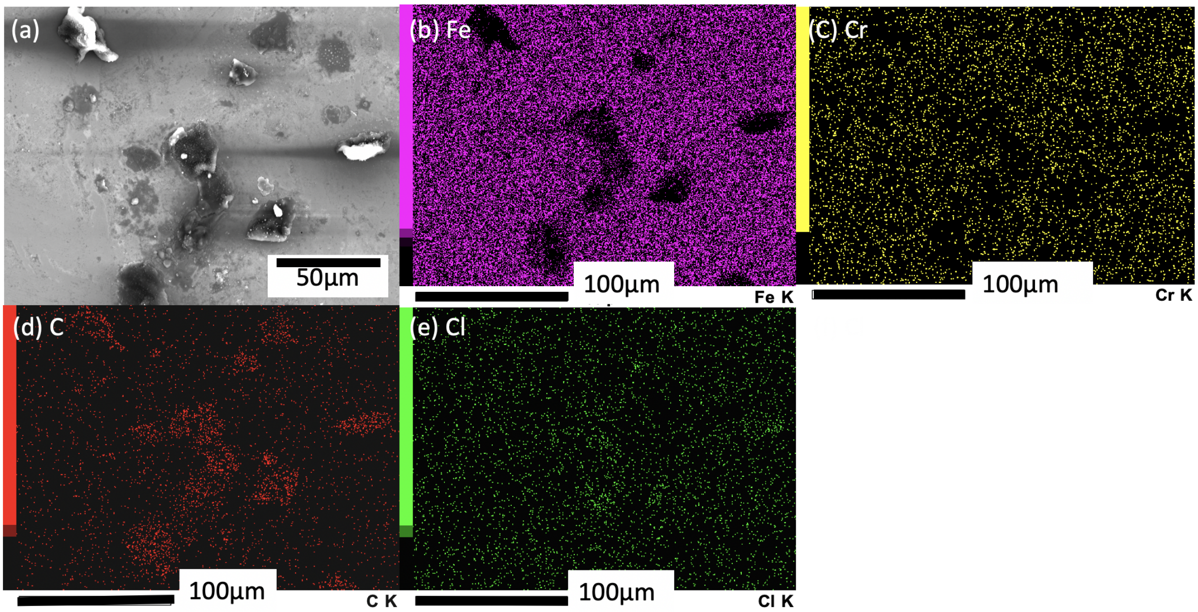

Figure B4: SEM image and EDS pattern at X500 on the side of the B steel at regions without corrosion and without masking with 0.5 wt% Cu

The corrosion results for B steel without masking pointed towards copper promoting corrosion. From the LOM images in Figure B2, the main form of corrosion on the B steel without copper is pitting corrosion, while the main form of corrosion on the B steel with 0.5 wt% Cu is uniform corrosion. Therefore, it was not similar to the finding in the literature review, which suggested that copper restricts uniform corrosion while promoting pitting corrosion. The steep slope of the cathodic curve of the Tafel plot shown in Figure B1 suggested a lack of oxygen. Combined with the corroded surface observed on the interface between the steel and the embedding resin, crevice corrosion occurred in the steel. The crevice corrosion was much more severe in the B steel with 0.5 wt% Cu. This observation was reinforced by Chapter 2.3.2, which states that copper promotes crevice corrosion in steel. Therefore, the increase in corrosion rate when copper was added to the steel could be due to the crevice corrosion in the steel. In addition, the occurrence of crevice corrosion suggested that the electrolyte had entered the interface between the steel and the resin. This increased the surface area exposed to the electrolyte, which needs to be included during the calculation of the corrosion rate. Therefore, the current corrosion results for the steel without masking is an overestimate of the actual corrosion rate, leading to the results for the steel without masking being less reliable.

A similar statement can also be concluded from the LOM images of the corroded steel surface without masking shown in Figure B2, where steels with copper showed only uniform corrosion on the surface. In contrast, steels without copper showed both pitting and uniform corrosion. Therefore, the effect of copper on pitting corrosion depends on the state of the surface. On certain surfaces, copper promotes pitting corrosion, but on other surfaces, it restricts pitting corrosion. To understand the phenomenon, more profound research will be needed to analyse how the surfaces affect the copper corrosion mechanism.

The difference in the steel's corrosion behaviour between with and without masking also suggested that any regions on the steel susceptible to attack could massively change its corrosion behaviour. The sides of the steel were the region most vulnerable to attack. Therefore, corrosion was most serious at the side of the steel without masking. In addition, black spots were detected on the side of the steel. From the EDS mapping shown in Figure B3 and Figure B4, these black spots contain a high concentration of carbon and low concentration of iron and chromium. It was most likely that the black spot was a source of contamination. These carbon-intensified black spots could act as cathodes during the corrosion, enhancing the galvanic effect on the side of the steel and leading to more severe corrosion.

From the Tafel plot of the steel without masking given in Figure B1, the cathodic curve depicted a very steep slope, inferring the lack of oxygen during corrosion. The LOM images in Figure B2 also suggested heavy corrosion on the interface between the steel and the resin. In addition, it was noticed that the steel with copper content has more severe corrosion of this type. This finding coincides with Chapter 2.3.2 of the literature review, which states that copper enhances the crevice corrosion of the steel.

The tables below provides the raw corrosion results from the samples without masking.

Table B2: Eocp values of the bearing steel without masking against Ag/AgCl reference electrode

Steel	1 (mV)	2 (mV)	3 (mV)	4 (mV)
100Cr6 (TM-160)	-428.457	-391.128	-357.592	-367.597
100Cr6Cu (TM-160)	-345.662	-446.822	-326.007	-404.907
100Cr6 (TM-240)	-415.125	-374.275	-398.596	-361.277
100Cr6Cu (TM-240)	-490.788	-410.014	-450.875	
100Cr6 (B)	-398.917	-401.593	-330.925	
100Cr6Cu (B)	-353.678	-420.362	-422.624	

Table B3: Ecorr values of the bearing steel without masking against Ag/AgCl reference electrode

Steel	1 (mV)	2 (mV)	3 (mV)	4 (mV)
100Cr6 (TM-160)	-416.611	-353.342	-348.919	-317.759
100Cr6Cu (TM-160)	-311.483	-411.831	-297.296	-358.397
100Cr6 (TM-240)	-376.538	-351.944	-369.928	-322.128
100Cr6Cu (TM-240)	-478.694	-339.694	-436.811	
100Cr6 (B)	-382.574	-374.078	-253.903	
100Cr6Cu (B)	-331.988	-408.944	-404.260	

Table B4: Corrosion density of the 100Cr6 bearing steel without masking

Steel	1 (µA/cm2)	2 (µA/cm2)	3 (µA/cm2)	4 (µA/cm2)
100Cr6 (TM-160)	8.881	4.631	4.112	4.186
100Cr6Cu (TM-160)	3.329	6.564	2.990	3.776
100Cr6 (TM-240)	4.603	3.911	2.640	3.183
100Cr6Cu (TM-240)	7.516	3.353	3.559	
100Cr6 (B)	4.342	3.749	3.753	
100Cr6Cu (B)	4.864	5.160	4.912	

Table B5: Corrosion rate of the 100Cr6 bearing steel without masking

Steel	1 (mmpy)	2 (mmpy)	3 (mmpy)	4 (mmpy)
100Cr6 (TM-160)	0.103889	0.054173	0.048102	0.048968
100Cr6Cu (TM-160)	0.038942	0.076785	0.034968	0.044171
100Cr6 (TM-240)	0.053846	0.045751	0.030882	0.037235
100Cr6Cu (TM-240)	0.087922	0.039223	0.041633	
100Cr6 (B)	0.050792	0.043856	0.043902	
100Cr6Cu (B)	0.056880	0.060361	0.057394	

The corrosion rate calculated was an estimation as an assumption that all iron oxidised to Fe^{2+} was made.